8217485

Womack, Kenneth Howard

TRADITIONAL AND SYNCHRONOUS CONVOLUTION METHODS FOR PROCESSING FRINGE PATTERN IMAGES

*The University of Arizona* PH.D. 1982

University Microfilms International 300 N. Zeeb Road, Ann Arbor, MI 48106

PLEASE NOTE:

In all cases this material has been filmed in the best possible way from the available copy. Problems encountered with this document have been identified here with a check mark _√_.

1. Glossy photographs or pages _____
2. Colored illustrations, paper or print _____
3. Photographs with dark background _√_
4. Illustrations are poor copy _____
5. Pages with black marks, not original copy _√_
6. Print shows through as there is text on both sides of page _____
7. Indistinct, broken or small print on several pages _√_
8. Print exceeds margin requirements _____
9. Tightly bound copy with print lost in spine _____
10. Computer printout pages with indistinct print _____
11. Page(s) __________ lacking when material received, and not available from school or author.
12. Page(s) __________ seem to be missing in numbering only as text follows.
13. Two pages numbered __________. Text follows.
14. Curling and wrinkled pages _____
15. Other________________________________________

# TRADITIONAL AND SYNCHRONOUS CONVOLUTION METHODS FOR PROCESSING FRINGE PATTERN IMAGES

by

Kenneth Howard Womack

A Dissertation Submitted to the Faculty of the

COMMITTEE ON OPTICAL SCIENCES (GRADUATE)

In Partial Fulfillment of the Requirements
For the Degree of

DOCTOR OF PHILOSOPHY

In the Graduate College

THE UNIVERSITY OF ARIZONA

1 9 8 2

THE UNIVERSITY OF ARIZONA
GRADUATE COLLEGE

As members of the Final Examination Committee, we certify that we have read the dissertation prepared by Kenneth Howard Womack

entitled Traditional and Synchronous Convolution Methods for Processing Fringe Pattern Images

and recommend that it be accepted as fulfilling the dissertation requirement for the Degree of Doctor of Philosophy.

| | |
|---|---|
| [signature] | 4/20/82 Date |
| James C. Wyant | 4/20/82 Date |
| Murray Sargent III | 4/20/82 Date |
| | Date |
| | Date |

Final approval and acceptance of this dissertation is contingent upon the candidate's submission of the final copy of the dissertation to the Graduate College.

I hereby certify that I have read this dissertation prepared under my direction and recommend that it be accepted as fulfilling the dissertation requirement.

James C. Wyant
Dissertation Director

4/20/82
Date

STATEMENT BY AUTHOR

This dissertation has been submitted in partial fulfillment of requirements for an advanced degree at The University of Arizona and is deposited in the University Library to be made available to borrowers under rules of the Library.

Brief quotations from this dissertation are allowable without special permission, provided that accurate acknowledgment of source is made. Requests for permission for extended quotation from or reproduction of this manuscript in whole or in part may be granted by the head of the major department or the Dean of the Graduate College when in his judgment the proposed use of the material is in the interests of scholarship. In all other instances, however, permission must be obtained from the author.

SIGNED: Kenneth H. Womack

## ACKNOWLEDGMENTS

I am greatly indebted to my advisor, Dr. J. Wyant, to C. R. Hayslett of the White Sands Missile Range, to the faculty and students of the Optical Sciences Center, and to my parents for the numerous opportunities they have provided me to grow and learn over the past five years.

TABLE OF CONTENTS

TABLE OF CONTENTS--Continued

LIST OF ILLUSTRATIONS

LIST OF ILLUSTRATIONS--Continued

## LIST OF TABLES

# ABSTRACT

The problem of recovering a wavefront or surface deviation from a fringe pattern image is investigated. The data sets generated in sampling a fringe pattern are considered in the frequency domain and errors that arise in analyzing the pattern are given an aliasing interpretation. Uniform sampling is shown to be superior to other sampling schemes. A variety of techniques for locating fringe centers are reviewed and three synchronous convolution methods are demonstrated that do not require the location of fringe centers. For the latter, direct phase measurements are obtained from fringe pattern photographs over a uniform grid with an accuracy comparable to temporal heterodyne interferometry. Two microprocessor-based video systems are described in which the traditional and synchronous convolution methods were implemented.

# CHAPTER 1

## INTRODUCTION

For years photographs have served as an intermediate step for obtaining phase measurements from interference and projected fringe patterns. The numerous systems and techniques which have been applied to their analysis usually have had the three steps listed below in common.

(1) The photograph is scanned to acquire the coordinates of fringe centers.

(2) Consecutive integers are assigned to data points along each fringe.

(3) The data triplets (x,y,order number) are analyzed to obtain numerical parameters and plots that characterize the surface.

A variety of phenomena associated with surface measurement can be understood when the data set generated in sampling a fringe pattern is considered in the frequency domain. This approach was used in this dissertation to investigate

(1) The relative merits of uniform, raster, and random sampling

(2) The advantage of a fringe pattern containing a tilt component (bias) over one with no tilt

(3) The design of interpolation schemes

(4) The effect of sampling sidelobes upon a Zernike fit.

In early systems a microdensitometer, an optical comparator, or a graphics tablet were often interfaced to a large mainframe computer. Recently self-contained systems have appeared in which an imaging detector such as a CCTV, image dissector, or diode array camera scans the fringe pattern while a dedicated mini- or microcomputer performs the analysis. Several of these systems are described in Chapter 2, including a video system developed at the Optical Sciences Center. For the latter, a CCTV camera was interfaced to a microcomputer and the coordinates of fringe centers were estimated from a thresholded image stored during a 480 x 512 x 1 bit frame capture. This bit map was superimposed upon the video image of the fringe pattern and lines at fringe minima were displayed. The operator visually checked the image for errors and, if necessary, edited the screen data by deleting points, adding line segments, or smoothing lines.

Undersampling and inaccurate fringe center estimates are the primary sources of error in systems based upon the traditional approach to fringe pattern reduction. A family of three convolution techniques are described in Chapter 3 that, to a considerable extent, overcome the disadvantages of the traditional methods. For these techniques direct phase measurements from photographs are made at any position within the fringe pattern and not just at fringe extrema. Measurements are readily obtained over a uniform grid with an accuracy comparable to that of temporal heterodyne interferometry. Results are presented that were obtained using a custom-designed video system capable of addressing 960 x 480 pixels at 6 bits depth.

## CHAPTER 2

## THE TRADITIONAL METHOD FOR ANALYZING FRINGE PATTERNS

### Background

The analysis of interferogram and projected fringe photographs involves selecting points at fringe centers and assigning to each an integer order number. The latter represents the distance between reference and test surfaces in units which depend upon exactly how the fringe pattern was produced. All points along a fringe are assigned the same number and the change in order number from one fringe to the next is one. The direction in which order numbers increase is determined by prior knowledge of which regions of the surface are high or low.

This procedure samples the surface height in a manner that is intrinsically aberration dependent. Sampling is also affected by the particular method used to scan fringes. If data are taken using a graphics tablet, points occur at random positions along each fringe. A raster-scan device, on the other hand, provides uniform sampling in one direction. Questions often arise concerning the impact of various sampling options on the analysis. These are phrased in many ways including:

How many fringes should be used?

How closely spaced should sample points be?

How many data points should be used?

Is uniform sampling better than nonuniform sampling?

The answers to these and other sampling questions are investigated in the next section.

With data selected and an order assignment complete, a global polynomial fit (Rimmer, 1972; Race, 1981; Loomis, 1976; Bezdidko, 1974; Wang and Silva, 1980; Crain and Bhattacharyya, 1967) or an interpolation (Hayslett and Swantner, 1978; Braile, 1978; Monro, 1980) or a combination of both are performed on the raw data. This serves two purposes:

(1) It enables removal of certain fit terms such as tilt and defocus before computing the numerical parameters and plots that describe the surface.

(2) It provides fractional order assignments over a uniform grid.

The latter is desirable if measurements are to be rotated or averaged. In addition, computer software for generating contour plots and other useful results is often designed to handle data over a uniform grid. If a fit is subtracted from the direct order assignment then accuracy in both the fit and the direct measurement must be regarded as equally important insofar as error in the end result is concerned. To go to great extremes in precisely locating the center of fringes and then to accompany this with a poor fit due to undersampling is not a good procedure.

Several workers have interfaced imaging detectors to small computers in efforts to automate fringe pattern reduction. Both active and passive approaches have been pursued. The former include heterodyne interferometry where a frequency or phase-shifting element is actively controlled during phase measurement (Massie, Nelson and Holly, 1979; Bruning et al., 1974; Balasubramanian and DeBell, 1980; Dandliker, 1977; Shagam, 1980; Koliopoulos, 1981). Commercial systems which take this approach include the Tropel System 70, the Spectra-Physics Diad, and the Zygo Mark III. These systems have the following advantages:

(1) The precision of phase measurements is dependent primarily upon the signal-to-noise ratio at which the fringe pattern is detected.

(2) Phase measurements are obtained over a uniform grid.

The major disadvantage is that live fringes are required. Measurements cannot be made on interferogram photographs and each interferometer must be equipped with a controllable element plus an imaging detector and associated electronics.

In the passive approach workers have concentrated upon analog and digital techniques for scanning fringes and locating their centers (Augustyn, Rosenfeld and Zanoni, 1978; Jones, 1977; Funnell, 1981; Freniere and Toler, 1981; Womack et al., 1979; Womack, Underwood and Forbes, 1980). These methods work with photographs and therefore are suited to a centralized interferogram analysis facility. This dissertation is primarily concerned with passive techniques for analyzing fringe patterns.

## Aliasing and Sampling Considerations

### The Sample Function

Let a two-dimensional fringe pattern be described by the equation,

$$I(x,y) = A+B\cdot\cos 2\pi W(x,y) = A+B\cdot\cos 2\pi[W'(x,y)-x/P] \ , \qquad (2.1)$$

where $W(x,y)$ is the surface deviation from a plane and $W'(x,y)$ is the surface with x-tilt of period P removed. By locating impulse sheets at fringe centers a sample function $S(x,y)$ is produced that can be written as a summation of exponentials as follows,

$$S(x,y) = \sum_{N=-\infty}^{\infty} \exp[i2\pi NW(x,y)]. \quad N=0,\pm1,\pm2, \ldots \qquad (2.2)$$

These impulse sheets are a two-dimensional generalization of the delta function (Gaskill, 1978; Huang, 1977) and are zero everywhere except along infinitely narrow lines. If $W'(x,y) = 0$, implying there is no aberration other than tilt, the impulse sheets are straight and parallel to the y-axis with spacing P. Examples of a fringe pattern and its sample function are presented in Figure 1. The form of Eq. (2.2) is recognized as similar to equations describing deformed gratings and interference-type binary computer-generated holograms (Yokozeki, Kusaka and Patorski, 1976).

The selection of points at fringe centers specifies a sample function. The assignment of order numbers can be regarded as multiplying the sample function times the surface $W(x,y)$ producing a data set $D(x,y)$ which is subsequently analyzed for peak-to-valley, rms, and other parameters. $D(x,y)$ can be written as follows,

$$D(x,y) = W(x,y) \cdot S(x,y) \ . \qquad (2.3)$$

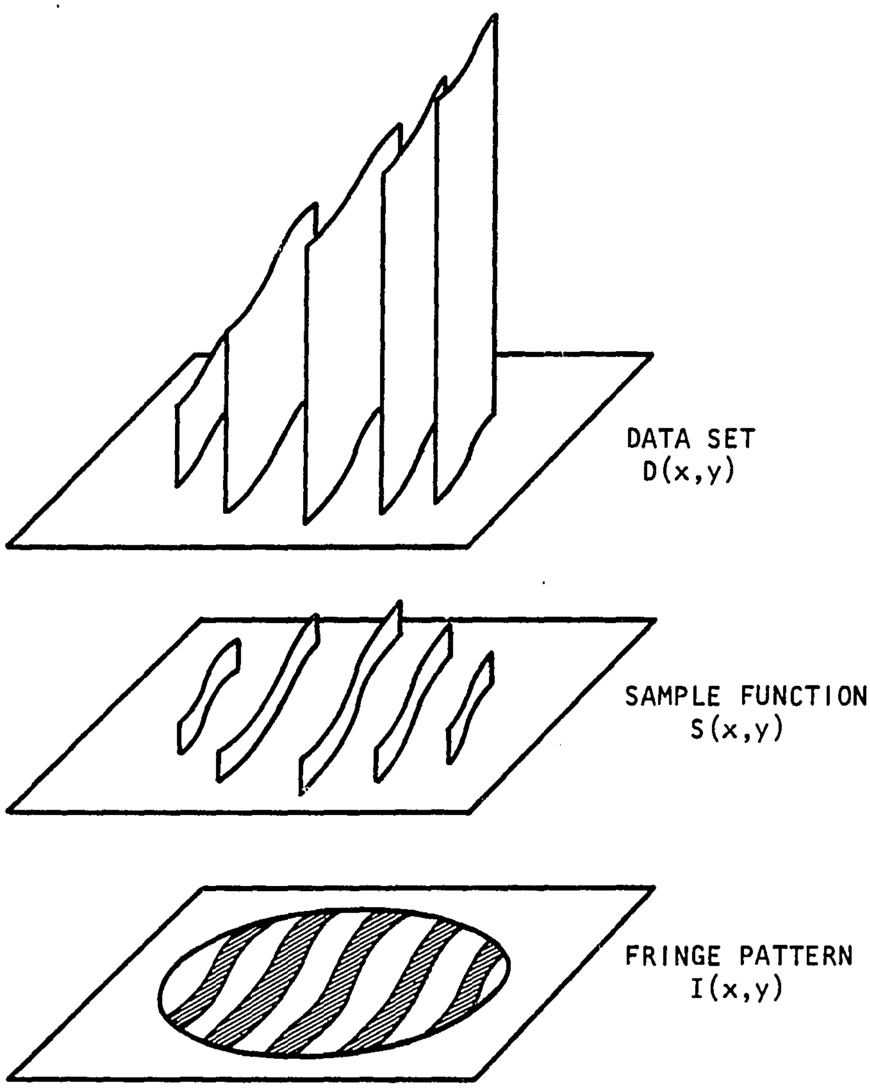


Figure 1. Data set and sample function associated with a fringe pattern.

The Fourier transform of D(x,y) is thus a convolution of the transforms of W(x,y) and S(x,y) given by

$$\overline{D}(F_x,F_y) = \overline{W}(F_x,F_y)*\overline{S}(F_x,F_y) \quad , \tag{2.4}$$

where an overhead bar is used to indicate the transform. If $W'(x,y) = 0$, the spectrum $\overline{D}(F_x,F_y)$ has a simple form with $\overline{W}(F_x,F_y)$ repeated in the frequency domain at regular intervals equal to the reciprocal of the fringe pattern spacing. For the moment sampling is regarded as infinitely dense along each fringe. This is never the real situation but it is instructive to consider this case before considering a finite number of sample points.

## Computer-Generated Holograms

The similarity between binary computer-generated holograms and the sampling function provides a valuable source of insight for understanding the form of the data spectrum $\overline{D}(F_x,F_y)$. A typical CGH and its diffraction pattern are shown in Figure 2 (Loomis, 1980). The latter was obtained at the transform plane of a lens positioned behind the CGH. The irradiance at the film plane was proportional to the modulus squared of the transform of the CGH transmittance. A bright narrow central peak was observed surrounded by higher diffraction orders whose widths were proportional to the diffraction order number. A cross-section of a typical CGH transform is illustrated in Figure 3. The CGH transmittance can be represented by a summation of exponentials as follows,

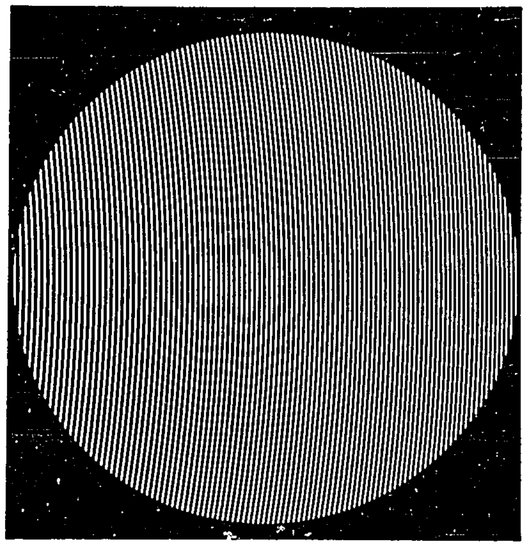

(a)

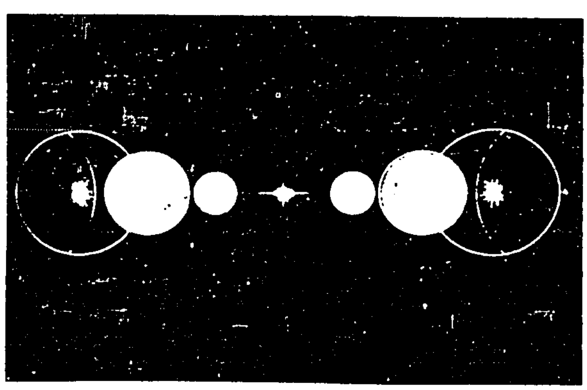

(b)

Figure 2. Interference-type computer-generated hologram.

(a) Binary fringe pattern.
(b) Diffraction pattern at the transform plane of a lens.

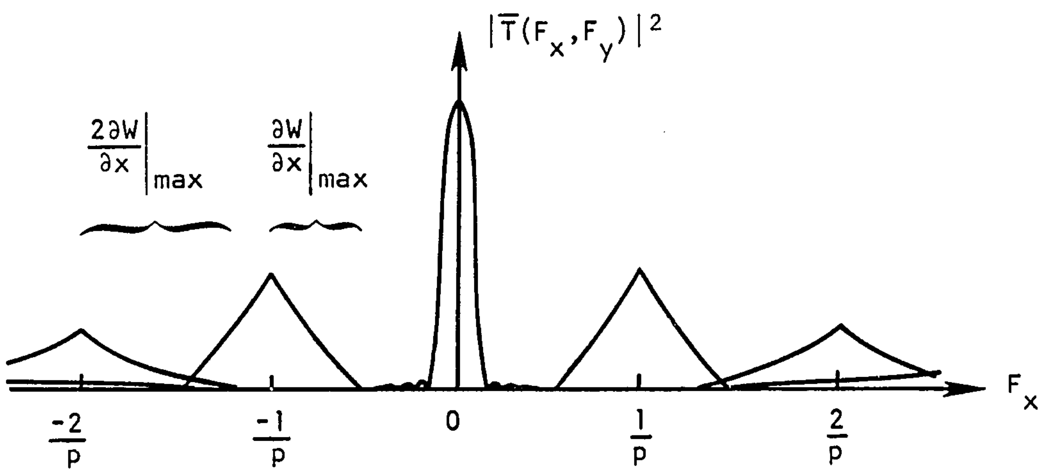


Figure 3. Cross-section of a CGH transform.

$$T(x,y) = P(x,y) \cdot \sum_{N=-\infty}^{\infty} C_N \exp[i2\pi N W(x,y)] \qquad N = 0, \pm 1, \pm 2, \ldots, \tag{2.5}$$

where P(x,y) is an aperture function equal to one inside the aperture and zero outside. By considering a plane wave decomposition of the N=1 term, the width of the first order diffraction lobe is estimated to be equal to the range of slopes of the surface W(x,y) plus a contribution due to the width of the transform of P(x,y). The latter also contributes to the width of the central peak of the diffraction pattern.

From Parseval's theorem, which is essentially a statement of conservation of energy, we have

$$\int_{-\infty}^{\infty}\int |\overline{T}(F_x,F_y)|^2 dF_x dF_y = \int_{-\infty}^{\infty}\int |P(x,y)|^2 dxdy \cdot \sum_{N=-\infty}^{\infty} C_N{}^2 \tag{2.6}$$

and so the energy or volume contained in each lobe is given by the square of the Fourier coefficient and is independent of the lobe width. In conclusion, the wider the diffraction lobe, the lower the peak. In Figure 3 the width of $\overline{P}(F_x,F_y)$ is assumed to be much less than the range of slopes for W(x,y). The higher order lobes are therefore shown with relatively sharp cut-off frequencies. To modify the CGH spectrum so that it equals the data spectrum $\overline{D}(F_x,F_y)$, the Fourier coefficients in Eq. (2.5) are set to one and $\overline{P}(F_x,F_y)$ is replaced by $\overline{W}(F_x,F_y)$. The sample spectrum $\overline{S}(F_x,F_y)$ produced by impulse sheets at fringe centers differs from a CGH spectrum primarily in its harmonic content which is expected since the sample function consists of infinitely narrow impulse sheets and the CGH transmittance consists of broad fringes.

The zero order peak of the data spectrum is a close approximation to $\overline{W}(F_x,F_y)$ provided a tilt component is present in the fringe pattern such that the various spectral orders are well-separated. The data spectrum $\overline{D}(F_x,F_y)$ can be written

$$\overline{D}(F_x,F_y) = \overline{W}(F_x,F_y) + \overline{A}(F_x,F_y) \quad , \tag{2.7}$$

where $\overline{W}(F_x,F_y)$ corresponds to the zero order peak and $\overline{A}(F_x,F_y)$ is the alias error due to all the sampling sidelobes. This same aliasing interpretation has been discussed by Huck, Halyo and Park (1980) with regard to uniformly sampled images. In general, recovery of W(x,y) from the data spectrum requires keeping the alias contribution small in the vicinity of the zero order. Common techniques for estimating W(x,y) from a data set D(x,y) include a global polynomial fit and local interpolation. Their connections with the frequency domain description of a data set are considered next.

Global Least Squares Fit

In this procedure the coefficients of a series expansion are determined so as to minimize the mean square error of the approximation. An error function can be written as

$$E = \int\int_{-\infty}^{\infty} S(x,y) \cdot \left[ W(x,y) - \sum_{n=\phi}^{N} C_n \phi_n \right]^2 dxdy \quad . \tag{2.8}$$

$S(x,y)$ is included in Eq. (2.8) to indicate that the integral is evaluated over the sample points which make up the data set $D(x,y)$. By setting the derivative with respect to $C_n$ equal to zero for all n, we obtain a set of normal equations. In matrix notation, these have the form,

$$\begin{bmatrix} \iint_{-\infty}^{\infty} \phi_1^2\, S(x,y)dxdy & \iint_{-\infty}^{\infty} \phi_1\phi_2 S(x,y)dxdy & \cdots \\ \iint_{-\infty}^{\infty} \phi_2\phi_1 S(x,y)dxdy & \iint_{-\infty}^{\infty} \phi_2^2 S(x,y)dxdy & \cdots \\ \vdots & \ddots & \\ & & \iint_{-\infty}^{\infty} \phi_N^2\, S(x,y)dxdy \end{bmatrix} \begin{bmatrix} C_1 \\ C_2 \\ \vdots \\ C_N \end{bmatrix} = \begin{bmatrix} \iint_{-\infty}^{\infty} D(x,y)\phi_1(x,y)dxdy \\ \iint_{-\infty}^{\infty} D(x,y)\phi_2(x,y)dxdy \\ \vdots \\ \iint_{-\infty}^{\infty} D(x,y)\phi_N(x,y)dxdy \end{bmatrix} \tag{2.9}$$

Solution of this set of simultaneous equations yields the coefficients $C_n$. Assuming the $\phi_n$ are orthogonal and sampling is infinitely dense, the off-diagonal terms of the normal equations reduce to zero and the fit coefficients are given directly by evaluating continuous integrals of the form,

$$C_n = \frac{\iint_{-\infty}^{\infty} D(x,y)\phi_n(x,y)dxdy}{\iint_{-\infty}^{\infty} \phi_n^2\, dxdy} \quad . \tag{2.10}$$

The integrals which appear in the normal equations are related to the data and sample spectra through the generalized form of Parseval's theorem, given by

$$\iint_{-\infty}^{\infty} F(x,y)\cdot G(x,y)dxdy = \iint_{-\infty}^{\infty} \overline{F}(F_x,F_y)\cdot\overline{G}(F_x,F_y)dF_x dF_y \ . \qquad (2.11)$$

Applying this theorem to the integrals on the right side of Eq. (2.9), we obtain values that can be interpreted as measures of the output of two-dimensional frequency domain filters. The Fourier transforms of the basis functions used for the surface approximation act as transfer functions that filter out a portion of the data spectrum. Similar interpretations can be given for the integrals on the left side of Eq. (2.9). For an appropriate choice of basis functions, such as Zernike polynomials, most of contribution to the integrals comes from a region near to and centered on the origin of the frequency plane. If the coefficients resulting from a least squares fit are to yield an approximation to the continuous surface $W(x,y)$, the filter outputs in the normal equations must pass the central peak and attenuate the sidelobes which extend over the entire frequency plane. Ideally sampling is dense enough that the data set $D(x,y)$ provides an alias-free duplicate of $\overline{W}(F_x,F_y)$ at the origin. To keep the aliasing error small, the distance between peaks of the data spectrum should be large compared to the width of $\overline{W}(F_x,F_y)$

It can be shown that if a least squares fit is performed in the spatial domain, a fit is simultaneously performed in the frequency domain. Following Papoulis (1962), let a function $V(x,y)$ approximate $W(x,y)$ where

$\overline{V}(F_x,F_y)$ is bandlimited to a region Q in the frequency domain. The least squares error function is given by

$$E = \iint_{-\infty}^{\infty} [W(x,y)-V(x,y)]^2 dxdy \ . \tag{2.12}$$

Expanding this expression and applying Parseval's theorem,

$$E = \iint_{-\infty}^{\infty} W^2 dxdy + \iint_{-\infty}^{\infty} V^2 dxdy - 2\iint_{-\infty}^{\infty} WV\ dxdy$$

$$= \iint_{-\infty}^{\infty} |\overline{W}|^2 dF_x dF_y + \iint_Q |\overline{V}|^2 dF_x dF_y - \iint_Q \overline{W}^* \overline{V} dF_x dF_y - \iint_Q \overline{W}\overline{V}^* dF_x dF_y . \tag{2.13}$$

Combining terms,

$$E = \iint_{\substack{\text{OUTSIDE}\\ Q}} |\overline{W}|^2 dF_x dF_y + \iint_Q [\overline{W}-\overline{V}]\cdot[\overline{W}^*-\overline{V}^*] dF_x dF_y$$

$$= \iint_{\substack{\text{OUTSIDE}\\ Q}} |W|^2 dF_x dF_y + \iint_Q |\overline{W}-\overline{V}|^2 dF_x dF_y \ . \tag{2.14}$$

The first term is independent of the approximation V(x,y). The error E is minimum provided the second term is minimized. By subtracting the first term from both sides, a frequency domain version of the error function can be written as follows,

$$E' = \iint_Q |\overline{W}-\overline{V}|^2 dF_x dF_y \ . \tag{2.15}$$

Therefore minimization of the error function in the spatial domain implies minimization of $E'$ in the frequency domain. Coefficients for a series expansion approximation in both spatial and frequency domains are identical. The approximation $V(x,y)$ is an accurate reconstruction of $W(x,y)$ provided aliasing is negligible.

From Figure 3 a condition can be stated which must be satisfied in order to have adequate separation between the first and zero order lobes. This aliasing criterion can be written

$$A_x + B_x < K/P \ , \tag{2.16}$$

where $A_x$ and $B_x$ are the characteristic widths of the zero and first order lobes, respectively, in the $F_x$-direction and K is a coefficient whose exact value depends upon the amount of aliasing to be tolerated. The characteristic widths can be regarded as containing a specified percentage of the total lobe energy.

## Special Cases

The discussion above has assumed sampling with infinite density along the center of each fringe. Three cases are considered below which correspond to a finite number of sample points.

Raster-Scan Sampling. Suppose discrete sample points are selected with a constant spacing L in the y-direction as shown in Figure 4. This new sample function $S'(x,y)$ is obtained from $S(x,y)$ by multiplying $S(x,y)$ times a straight, uniformly spaced impulse sheet function where the sheets are parallel to the x-axis. Thus $S'(x,y)$ can be written

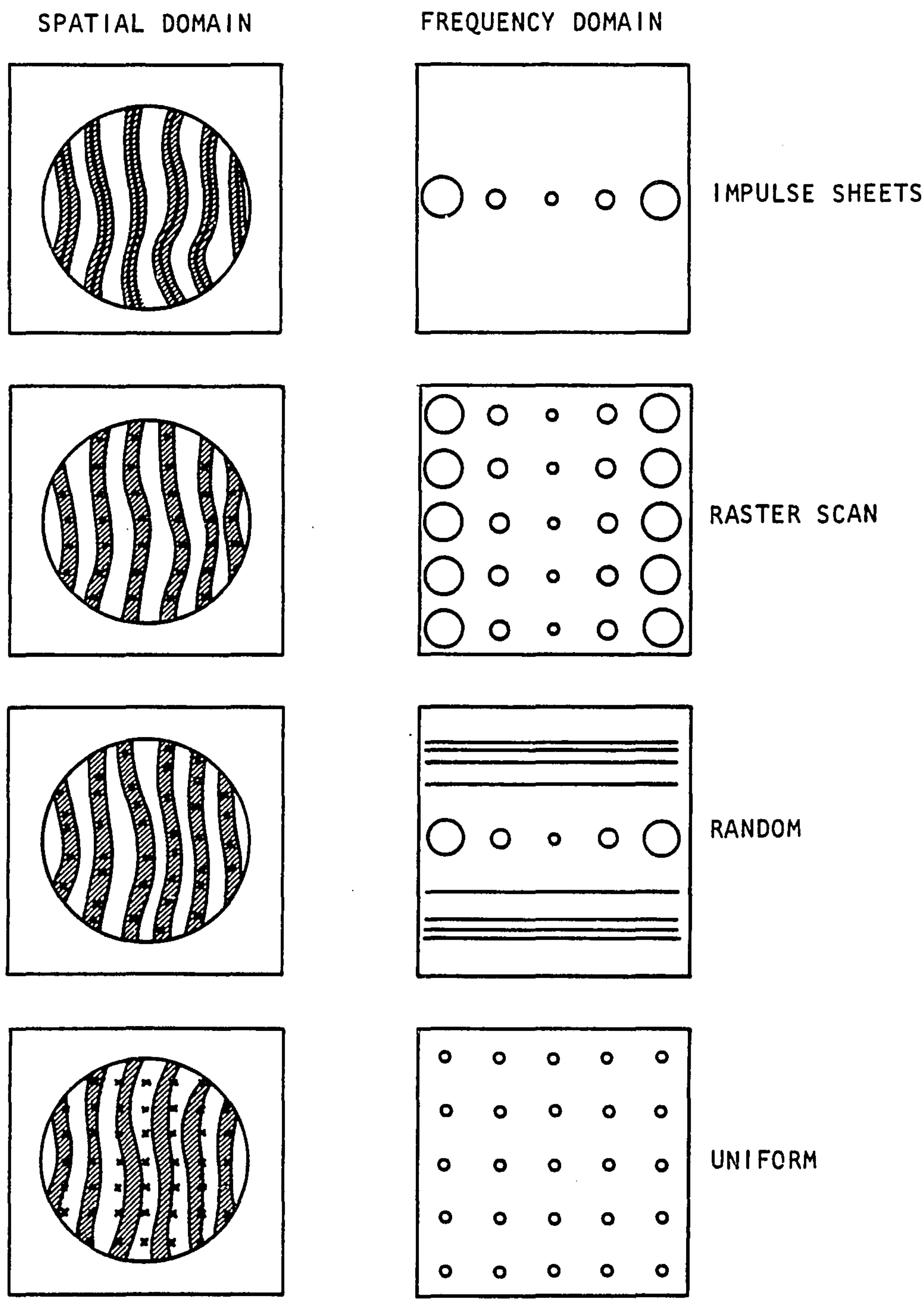


Figure 4. Data sets and spectra for several sampling schemes.

For convenience, frequency domain lobes are shown as circularly symmetric.

$$S'(x,y) = S(x,y) \cdot \sum_{N=-\infty}^{\infty} \exp[i2\pi Ny/L] \quad . \tag{2.17}$$

The transform of $S'(x,y)$ is just the familiar transform $\overline{S}(F_x,F_y)$ repeated at a regular interval in the $F_y$-direction. Uniform sampling in the y-direction thus leads to two aliasing criteria that can be stated as follows,

$$A_x + B_x < K/P \qquad F_x\text{-direction}$$

$$2A_y < K/L \qquad F_y\text{-direction} \quad . \tag{2.18}$$

<u>Random Sampling</u>. Let discrete sample points be chosen at random positions along each fringe. The new sample function $S'(x,y)$ is obtained by multiplying the original $S(x,y)$ discussed above by impulse sheets which intersect $S(x,y)$ at the discrete data points. $S'(x,y)$ can be written

$$S'(x,y) = S(x,y) \cdot \sum_{N=-\infty}^{\infty} \exp\Big[i2\pi N[K(x,y)-y/G]\Big] \quad . \tag{2.19}$$

By introducing an artificial surface function $K(x,y)$ the impulse sheets overlapping $S(x,y)$ are given the proper curvature to intersect $S(x,y)$ at the desired positions. G is the nominal spacing of the new impulse sheets which can be regarded as sheets of a perturbed raster scan. If the fringe pattern is sampled using a graphics tablet the perturbation may be treated as a random variable having a uniform probability over an interval of width G. Depending on how the tablet is used a probability density function whose width is a fraction of the nominal spacing may be appropriate. In any case the statistical description of a jittered sample array presented in a later section is applicable. The major result is that a continuous component is superimposed upon the usual raster scan spectrum. If we assume the biased fringe pattern is oriented roughly parallel to the y-axis, this spectral contribution is zero at the origin and increases with increasing distance from the $F_x$-axis. For a uniform probability density over the nominal sample interval the continuous component has the form

$$E\{|\overline{S}'(F_x,F_y)|^2\} \propto 1 - |\mathrm{SINC}(G\cdot F_y)|^2 \quad . \tag{2.20}$$

In effect, the usual raster spectrum is washed out by the random perturbation except for a zone surrounding the $F_x$-axis. This picture is in agreement with a physical experiment performed by Aime and Martin (1980) in which masks containing a jittered array of apertures were illuminated by a coherent beam while observing the diffraction pattern in the Fourier transform plane of a lens.

Uniform Sampling. Suppose a phase measurement scheme could be devised that would free us from the necessity of locating sample points at fringe centers. Let the raw data be taken over a uniform grid with spacing P. $\overline{S}'(F_x,F_y)$ then has the form of delta functions repeated over a uniform grid in the frequency domain resulting in a spectrum for $\overline{D}'(F_x,F_y)$ such as that shown in Figure 4. The aliasing criteria for uniform sampling become the following,

$$2A_x < K/P \qquad F_x\text{-direction}$$

$$2A_y < K/P \qquad F_y\text{-direction} \quad . \tag{2.21}$$

In conclusion, all the sampling schemes described perform adequately provided sampling is dense enough to provide an undisturbed version of $\overline{W}(F_x,F_y)$ at the origin. It is possible, nevertheless, to rank the schemes in terms of the severity of their aliasing criteria and their frequency domain pictures. Uniform sampling is best. Fewer sample points are required if W(x,y) is uniformly sampled than if it is sampled by any other method. Raster-scan sampling is second and random sampling is last. It is noted that as the aberration goes to zero, the fringe pattern becomes straight and raster-scan scampling becomes equivalent to uniform sampling. Statistical considerations suggest that in using a graphics tablet to sample a fringe pattern it is constructive to place a ruled transparent mylar sheet over the photograph to serve as a guide for a raster scan.

Closed Fringes

If the fringe pattern contains closed fringes, the higher order lobes of $\overline{D}(F_x,F_y)$ overlap the zero order as illustrated in Figure 5. The situation is analogous to the overlapping diffraction orders of a Gabor hologram. An approach to reducing the effects of aliasing, assuming closed fringes cannot be avoided, is to introduce deliberately an aberration such as defocus so that the widths of the higher order lobes spread and their peaks drop relative to the peak of the zero order. The added aberration can be subtracted following a least squares fit to the data set.

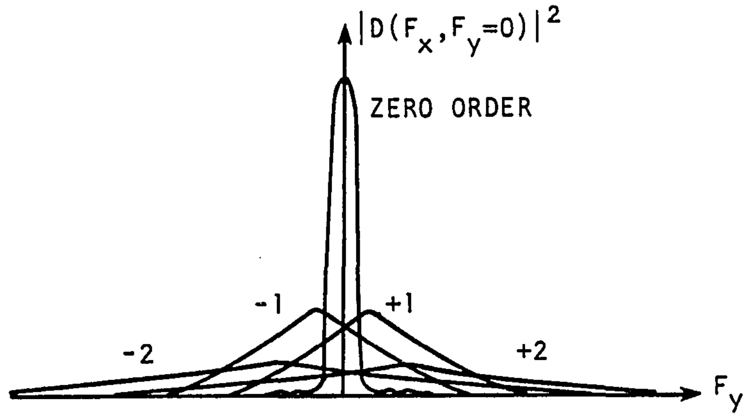


Figure 5. Example of data spectrum for closed fringes showing overlapping orders.

Of course, a better solution to the problem of overlapping spectral orders is to introduce enough tilt to separate the lobes, i.e., eliminate closed fringes from the pattern. Again there is a close analogy with holography where Leith and Upatnieks (1962) suggested use of a high spatial frequency carrier as an improvement to the Gabor technique.

Interpolation

Two-dimensional interpolation (Hayslett and Swantner, 1978; Braile, 1978; Monro, 1980) has served as an alternative to a global fit for obtaining phase measurements over a uniform grid. Interpolation can be modeled as a convolution of the raw data $D(x,y)$ with a continuous weighting function $H(x,y)$ followed by sampling over a uniform grid. With proper choice of $H(x,y)$ the new data set $D'(x,y)$ approximates $W(x,y)$ over the grid. $D'(x,y)$ can be written

$$D'(x,y) = [D(x,y) * H(x,y)] \cdot S'(x,y) \,, \tag{2.22}$$

where $S'(x,y)$ is a uniform sampling function. The convolution of $D(x,y)$ with a weighting function is equivalent to applying a low-pass filter to the transform of $D(x,y)$. Again aliasing due to sampling sidelobes is a source of error.

Each element of $D'(x,y)$ can be computed by positioning $H(x,y)$ at the intersection of a uniform grid, multiplying the order values of sample points in the neighborhood by the value of $H(x,y)$ at each point, and summing over the products. If $H(x,y)$ is circularly symmetric then the distance of a sample point from the grid intersection determines the weight to be applied at that point. For a biased fringe pattern where the data spectrum consists of a central peak and well-separated sidelobes, an interpolation function of the form $H(x) \cdot \delta(y)$ is acceptable provided data is taken using a raster scan. This type of convolution filters out the peaks along the $F_y$-axis of the raster spectrum shown in Figure 4, where each of these peaks is equal to the Fourier transform of $W(x,y)$. What remains after filtering is just the spectrum produced by sampling $W(x,y)$ with a raster of impulse sheets. This is attractive since the data reduction is one-dimensional with each line treated independently of all others. Such a procedure could be implemented on a computer much more rapidly than convolution using a circularly symmetric interpolation function.

A rect function is not a good choice for $H(x)$ due to the relatively large sidelobes of its sinc transfer function. The attenuation at the peak of the first sidelobe is only -13db. A better choice is a Hamming function or any of the popular filter functions used in digital signal processing (Stanley, 1975; Nuttall, 1981). A Hamming window provides better than -40db attenuation (factor of 100) outside its passband.

In some ways interpolation is a more attractive procedure than performing a global least squares fit. Whereas a fit tends to require a large number of terms to reconstruct a local hill or valley of $W(x,y)$, interpolation successfully recovers it provided

(1) The width of the hill or valley is significantly greater than the characteristic width of the interpolation function.

(2) The fringe density is large enough that several sample points occur across the local feature.

Zernike Polynomials

The relationship of a Zernike polynomial expansion to the spectrum $\overline{D}(F_x,F_y)$ is important since a summation of Zernike terms is often used to describe wavefronts in optical testing. The Zernike terms have the form

$$Z_N^M(r,\theta) = R_N^M(r)\cdot\exp[iM\theta] \qquad \begin{array}{l} M \,\&\, N \text{ are integers;} \\ N > 0,\ M < N; \\ (M+N) \text{ always even} \end{array} \tag{2.23}$$

where the $R_N^M(r)$ are Zernike polynomials. These terms form a complete, orthogonal set over a unit circle. From Kintner and Sillitto (1976) the Fourier transform of Eq. (2.23) can be written

$$\overline{Z_N^M}(\rho,\phi) = (-i)^N\cdot A_N(\rho)\cdot\exp iM\phi\ , \tag{2.24}$$

where

$$A_N(\rho) = \frac{J_{N+1}(2\pi\rho)}{\rho}\ .$$

The variables $\rho$ and $\phi$ are frequency coordinates in polar form and $J_N(2\pi\rho)$ is the Nth order Bessel function. The Zernike transforms also form a complete, orthogonal set. $\overline{Z_N^M}(\rho,\phi)$ consists of circular rings with an angular modulation dependent on the integer M and an amplitude factor $A_N(\rho)$ that decreases as $\rho$ increases. Using a well-known property of Bessel functions (Hildebrand, 1962), the asymptotic behavior of the amplitude factor for large $\rho$ is given by

$$\lim_{\rho\to\infty} A_N(\rho) = \left(\frac{1}{\pi\rho^{3/2}}\right) \cos\left(2\pi\rho - \frac{N\pi}{2} + \frac{\pi}{4}\right) \quad . \tag{2.25}$$

In this limit $A_N(\rho)$ is independent of N except for a phase term. Figure 6 presents a plot of $A_N(\rho)$ for several values of N. To relate the scale of this plot to a pupil of diameter d, multiply the dimensionless frequency coordinate $\rho$ by $\frac{2}{d}$ .

Let's estimate the fraction of the energy of each Zernike transform that lies outside a circle of radius $\rho_o$ centered at the origin of the frequency plane. Since the Zernike amplitude is always less than $\frac{1}{\pi\rho^{3/2}}$ , the following inequality must be true,

$$\int_0^{2\pi} \int_{\rho_o}^{\infty} |\overline{Z_N^M}(\rho,\phi)|^2 \, \rho d\rho d\phi < \int_{\rho_o}^{\infty} \left(\frac{1}{\pi\rho^{3/2}}\right)^2 \cdot 2\pi\rho d\rho$$

$$= \frac{2}{\pi} \int_{\rho_o}^{\infty} \frac{1}{\rho^2} \, d\rho = \frac{2}{\pi\rho_o} \quad . \tag{2.26}$$

Therefore the energy lost by truncation at $\rho_o$ is always less than $\frac{2}{\pi\rho_o}$ independent of the Zernike order number N. From Kintner and Sillitto the total energy for each term is given by

$$\int_0^{2\pi} \int_0^{\infty} |\overline{Z_N^M}(\rho,\phi)|^2 \, \rho d\rho d\phi = \frac{\pi}{N+1} \quad . \tag{2.27}$$

Dividing Eq. (2.26) by Eq. (2.27) the fraction of the total energy outside $\rho_o$ is given by

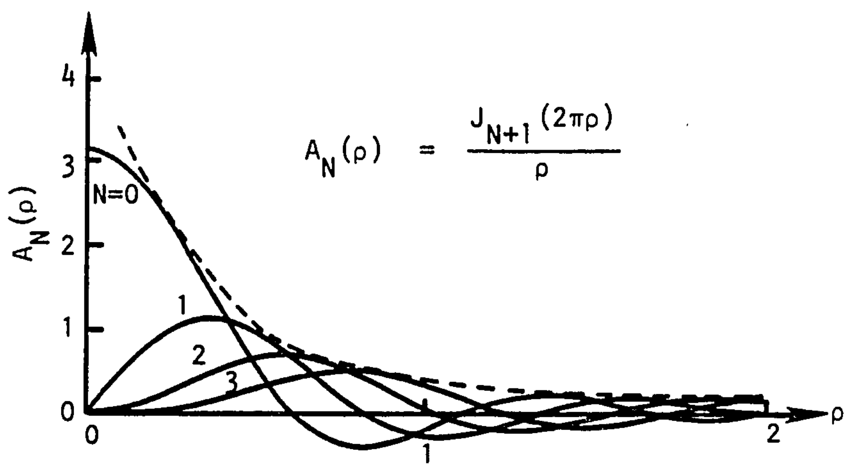


Figure 6. Radial amplitude for Zernike transforms vs. frequency. Dotted line shows the envelope $(1/\pi\rho^{3/2})$.

$$\frac{E_{\rho>\rho_0}}{E_{total}} < \frac{2(N+1)}{\pi^2 \rho_0} \quad . \tag{2.28}$$

Therefore higher order Zernike terms have more energy at a large distance from the origin than do smaller order number terms. For this reason higher order fit coefficients are more strongly affected by sampling sidelobes than lower order terms.

The alias error $\overline{A}(F_x,F_y)$ in the vicinity of the central peak of the $\overline{D}(F_x,F_y)$ can be regarded as noise which degrades a least squares fit or interpolation in the spatial domain. Let a surface W(x,y) be uniformly sampled such that $\overline{D}(F_x,F_y)$ is composed of duplicates of $\overline{W}(F_x,F_y)$ spaced at regular intervals 1/P. The envelope amplitude of $\overline{D}(F_x,F_y)$ midway between lobes can be taken as a measure of the alias error. For $\rho_o = 10$ at the midpoint implying a sample spacing of d/40 the amplitudes of the Zernike terms are down by a factor of 100. The energy for each term which lies beyond the midpoint can be estimated from Figure 7. The alias error within the zone of radius is a summation of cosine-like terms similar to Eq. (2.25), each having an amplitude less than 1% of the corresponding Zernike coefficient. The period of oscillation is the same for all these terms and is independent of the sidelobe from which the aliasing contribution originated. The alias error is therefore much like an undesired grating in the frequency domain which arises due to the presence of sampling sidelobes. Due to the period of this grating, aliasing shows up in the spatial domain primarily as broad peaks located on opposite edges of the pupil. Alias error at the edges may be expected

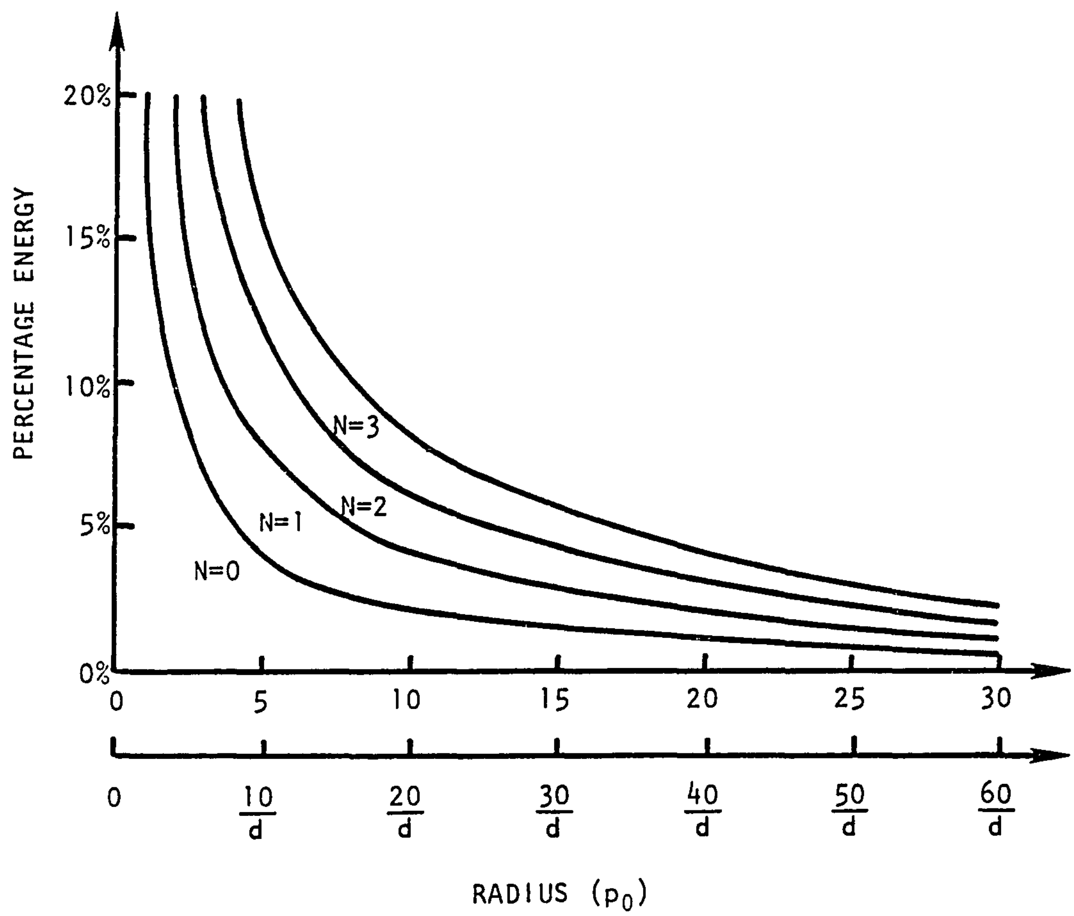


Figure 7. Upperbound to percentage energy lying outside a circle of radius $\rho_0$ in the frequency domain.

Pupil diameter = D. Zernike order number = N.

to have a symmetry dependent upon the sampling scheme. The difficulty of obtaining a good fit at the edge of the pupil is a common observation.

B-Spline Fit

Spline curves are of interest in fringe pattern analysis for interpolating fringe order assignments to a uniform grid. Renes and Beintema (1981) have described the use of B-spline fits for image data compression and have discussed a frequency domain interpretation of the B-spline approximation. Briefly, a spline fit is a procedure in which a polynomial of order K is fit to successive sample intervals in such a manner that the K-2th and lower derivatives of the spline are continuous at interval end points. The polynomial arc for an interval is defined recursively by repeated convolution of the first order spline such that

$$
\begin{aligned}
B_1(x) &= 1 && |x| < 1/2 \\
B_2(x) &= B_1 * B_1 \\
&= 1 - |x| && |x| < 1 \\
B_3(x) &= B_2 * B_1 \\
&= \begin{cases} 3/4 - x & |x| < 1/2 \\ 1/2[3/2 - |x|]^2 & 1/2 < |x| < 3/2 \end{cases} \\
B_K(x) &= B_{K-1} * B_1 && (2.29)
\end{aligned}
$$

where the width of the sample interval is taken to be unity. A one-dimensional spline curve can be written as a summation of successive basis functions as follows

$$L(x) = \sum_n C_n B_K(x-n) \ , \tag{2.30}$$

where the $C_n$ are coefficients associated with the spline intervals. Spline basis functions through 4th order (3rd degree polynomial) are plotted in Figure 8 (Gordon and Bhattacharyya, 1974). If a spline curve is fit to samples obtained across a raster-scan of $W(x,y)$ then a least squares error condition can be defined as follows,

$$E = \int_{-\infty}^{\infty} S(x)\cdot[W(x,y=y_o) - L(x)]^2 dx \ , \tag{2.31}$$

where $S(x)$ is a sample function used to indicate that E is evaluated over discrete data points. A set of normal equations is derived which have the form

$$\begin{bmatrix} \int_{-\infty}^{\infty} S(x)\cdot[B_K(x-\nu_1)]^2 dx & \int_{-\infty}^{\infty} S(x)\cdot B_K(x-\nu_1)B_K(x-\nu_2)dx \ \ldots \\ \int_{-\infty}^{\infty} S(x)\cdot B_K(x-\nu_2)\cdot B_K(x-\nu_1)dx & \int_{-\infty}^{\infty} S(x)\cdot[B_K(x-\nu_2)]^2 dx \\ \vdots & \ddots \\ & \int_{-\infty}^{\infty} S(x)\cdot[B_K(x-\nu_N)]^2 dx \end{bmatrix} \begin{bmatrix} C_1 \\ C_2 \\ \vdots \\ C_N \end{bmatrix}$$

(continued)

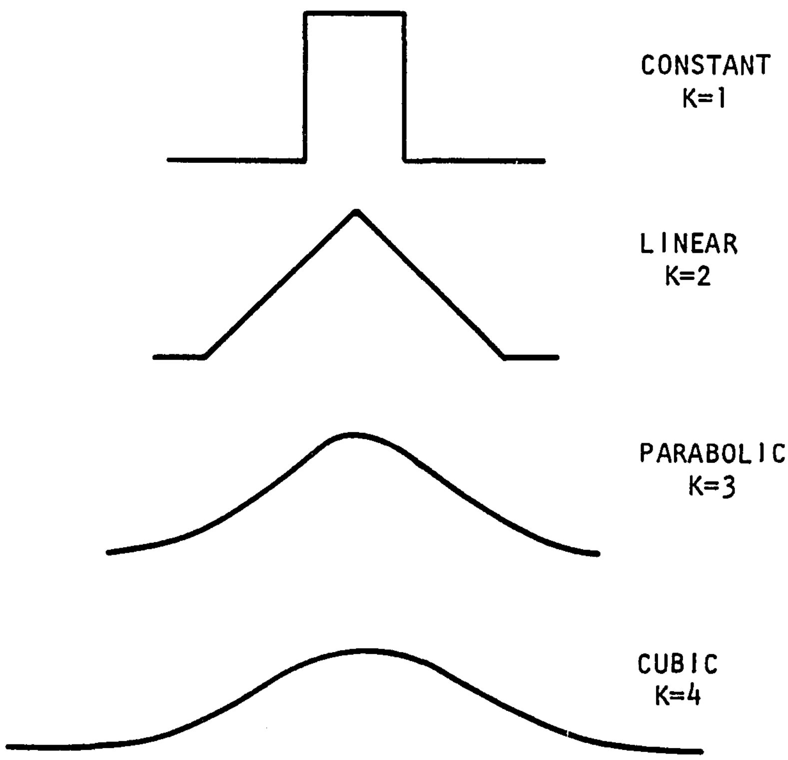


Figure 8. Spline basis functions.

$$= \begin{bmatrix} \int_{-\infty}^{\infty} D(x) B_K(x-\nu_1) dx \\ \int_{-\infty}^{\infty} D(x) B_K(x-\nu_2) dx \\ \vdots \\ \int_{-\infty}^{\infty} D(x) B_K(x-\nu_N) dx \end{bmatrix} \quad . \tag{2.32}$$

D(x) represents the data set for a scan line. The integrals on the left side are mostly zero except for a few terms near the diagonal.

Renes and Beintema (1981) point out that the Fourier transform of $B_K(x)$ is simply $\text{sinc}^K(F_x)$ for a spline interval of unit width. From Parseval's theorem the integrals on the right above are therefore given by frequency domain expressions of the form

$$\int_{-\infty}^{\infty} D(x) \cdot B_K(x-\nu_j) dx = \int_{-\infty}^{\infty} \exp(i2\pi F_x \nu_j) \cdot \text{sinc}^k(A \cdot F_x) \cdot \overline{D}(F_x) dF_x \quad , \tag{2.33}$$

where a spline interval of width A is assumed. The spline fit thus has the attractive property of filtering the data spectrum with a function that falls off as $F_x^{-K}$. Linear interpolation between sample points corresponds to a second order spline (K=2) and thus the peak of the first sidelobe is down by approximately -26db (factor of $4 \times 10^{-2}$). For a fourth order spline (cubic arc) the peak of the first sidelobe is down by approximately -52db (factor of $2 \times 10^{-3}$). If the fringe pattern is strongly biased, the width of the spline transfer function is automatically a fraction of the distance between central peak and the first sidelobe. Since a spline fit is constrained to pass through each data point, local interpolation errors occur if a sample obtained in estimating the location of a fringe center is incorrectly positioned.

## A Jittered Data Set

In locating sample points at fringe centers, random jitter is often introduced due to various sources of measurement error (Aime and Martin, 1980; Lawson and Uhlenbeck, 1950; Pole, Spiekerman and Hansch, 1980; Huang, 1977). These include electrical instability in the image scanner and errors in operator judgment for manual scanning. An example of a jittered data set is presented in Figure 9.

To model this random process consider a set of N sample points whose x and y coordinates are $x_k + \underset{\sim}{\varepsilon_k}$ and $y_k + \underset{\sim}{\alpha_k}$ for the kth point where $x_k$ and $y_k$ are the ideal coordinates for the fringe center and $\underset{\sim}{\varepsilon_k}$ and $\underset{\sim}{\alpha_k}$ are independent random variables describing displacements in the x and y directions. The perturbed sample function $S'(x,y)$ can be written

$$S'(x,y) = \sum_{k=\phi}^{N-1} \delta(x - x_k - \underset{\sim}{\varepsilon_k},\ y - y_k - \underset{\sim}{\alpha_k}) \quad . \tag{2.34}$$

To determine the average effect of the random process upon the sample spectra, let's compute the expected value of the modulus squared of the Fourier transform of $S'(x,y)$. Taking the transform of $S'(x,y)$,

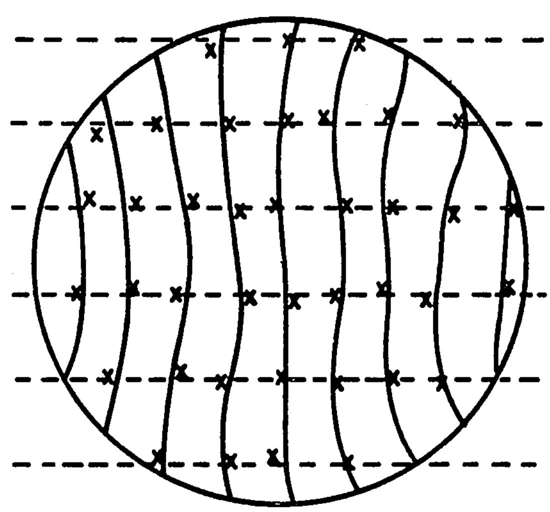

Figure 9. Sample points with jitter about intersections of a raster scan and lines at fringe centers.

$$\overline{S'}(F_x,F_y) = \sum_{k=\phi}^{N-1} e^{i2\pi F_x(x_k+\underset{\sim}{\epsilon_k})} \cdot e^{j2\pi F_y(y_k+\underset{\sim}{\alpha_k})} \quad . \tag{2.35}$$

The modulus squared is given by

$$|\overline{S'}(F_x,F_y)|^2 = N + \sum_{\substack{k=\phi \\ k\neq\ell}}^{N-1} \sum_{\ell=\phi}^{N-1} e^{i2\pi F_x[(x_k-x_\ell)+(\underset{\sim}{\epsilon_k}-\underset{\sim}{\epsilon_\ell})]}$$

$$\cdot\; e^{i2\pi F_y[(y_k-y_\ell)\; +\; (\underset{\sim}{\alpha_k}-\underset{\sim}{\alpha_\ell})]} \quad . \tag{2.36}$$

Taking the ensemble average of $|\overline{S'}(F_x,F_y)|^2$,

$$E\{|\overline{S'}(F_x,F_y)|^2\} = N + |\Phi_\epsilon(F_x)|^2 \cdot |\Phi_\alpha(F_y)|^2$$

$$\cdot \sum_{\substack{k=0 \\ k\neq\ell}}^{N-1} \sum_{\ell=0}^{N-1} e^{i2\pi F_x(x_k-x_\ell)} \cdot e^{i2\pi F_y(y_k-y_\ell)} \quad . \tag{2.37}$$

Subtracting and adding the term $N\cdot|\Phi_\epsilon(F_x)|^2 \cdot |\Phi_\alpha(F_y)|^2$ restores the $k=0$, $\ell=0$ terms of the summation as follows

$$E\{|\overline{S'}(F_x,F_y)|^2\} = N - N\cdot|\Phi_\epsilon(F_x)|^2 \cdot |\Phi_\alpha(F_y)|^2$$

$$+ \; |\Phi_\epsilon(F_x)|^2 \cdot |\Phi_\alpha(F_y)|^2 \cdot \sum_{k=0}^{N-1} \sum_{\ell=0}^{N-1} e^{i2\pi F_x(x_k-x_\ell)}$$

$$\cdot\; e^{i2\pi F_y(y_k-y_\ell)} \quad . \tag{2.38}$$

With this change the summation is recognized as equal to the modulus squared of the transform of the ideal sample function $S(x,y)$. This expression can be written,

$$E\{|S'(F_x,F_y)|^2\} = N - N\cdot|\Phi_\varepsilon(F_x)|^2\cdot|\Phi_\alpha(F_y)|^2$$

$$+ |\Phi_\varepsilon(F_x)|^2\cdot|\Phi_\alpha(F_y)|^2\cdot|\overline{S}(F_x,F_y)|^2 \quad . \tag{2.39}$$

From this result the effects of jitter upon the sample spectra are the following:

(1) The lobes of the ideal spectra are attenuated by an amount dependent upon the characteristic functions $\Phi_\varepsilon(F_x)$ and $\Phi_\alpha(F_y)$.

(2) A continuous component is added to the ensemble average due to the first two terms of Eq. (2.39).

In the limiting case in which the jitter goes to zero the characteristic functions become unity and the expected value is the modulus squared of the ideal sample spectra. If the jitter is sufficiently large that the widths of the characteristic functions are much less than the width of the zero order lobe of the ideal sample spectrum, the ensemble average is dominated by the continuous component, i.e., the ideal sample spectrum is washed out.

This analysis is easily extended to the perturbed data set $D'(x,y)$ by writing

$$D'(x,y) = \sum_{k=0}^{N-1} W_k \delta(x - x_k - \underset{\sim}{\varepsilon_k},\ y - y_k - \underset{\sim}{\alpha_k}) \quad , \tag{2.40}$$

where $W_k$ is the order assignment at the sample point. The modulus squared of $\overline{D'}(F_x,F_y)$ is given by

$$|D'(F_x,F_y)|^2 = N \sum_{k=0}^{N-1} W_k{}^2 + \sum_{k=0}^{N-1} \sum_{\ell=0}^{N-1} W_k W_\ell e^{i2\pi F_x[(x_k-x_\ell)+(\underset{\sim}{\varepsilon_k}-\underset{\sim}{\varepsilon_\ell})]}$$

$$\cdot\ e^{i2\pi F_y[(y_k-y_\ell)+(\underset{\sim}{\varepsilon_k}-\underset{\sim}{\varepsilon_\ell})]} \quad . \tag{2.41}$$

The first summation is related in a simple manner to the standard deviation and mean over the data set. Consider the following,

$$\sigma_D{}^2 = \frac{1}{N} \sum_{k=0}^{N-1} (W_k - \mu_D)^2 \quad , \tag{2.42}$$

where $\mu_D$ is the mean for the data set. Expanding this expression,

$$N\sigma_D{}^2 = \left(\sum_{k=0}^{N-1} W_k{}^2\right) - 2\mu_D\left(\sum_{k=0}^{N-1} W_k\right) + N\mu_D{}^2$$

$$= \left(\sum_{k=0}^{N-1} W_k{}^2\right) - N\mu_D{}^2$$

$$\therefore \sum_{k=0}^{N-1} W_k{}^2 = N\cdot(\sigma_D{}^2 + \mu_D{}^2) \quad . \tag{2.43}$$

Making this substitution in Eq. (2.41) and continuing with the derivation of the ensemble average,

$$E\{|\overline{D'}(F_x,F_y)|^2\} = N\cdot(\sigma_D{}^2+\mu_D{}^2)\cdot[1-|\Phi_\varepsilon(F_x)|^2\cdot|\Phi_\alpha(F_y)|^2]$$

$$+ |\Phi_\varepsilon(F_x)|^2\cdot|\Phi_\alpha(F_y)|^2\cdot|\overline{D}(F_x,F_y)|^2 \ . \tag{2.44}$$

The major new feature is the additional factor $\sigma_D{}^2+\mu_D{}^2$ in the continuous component of the ensemble average. From the discussion of Zernike polynomials the effect of the continuous component tends to show up in higher order coefficients of a Zernike fit. An example of jittered data spectrum for uniform sampling is presented in Figure 10.

## Spatial Quantization

To this point the discussion has assumed infinite resolution for specifying the location of a sample point. In practice resolution is limited and the photograph image is partitioned into a finite number of resolution cells. A position on the photograph cannot be measured to a precision exceeding the width of a single cell. Figure 11 illustrates the resulting measurement error. This effect can be modeled as jitter with a uniform probability distribution over a range equal to the dimensions of one cell. The description in the previous section is then directly applicable.

The peak-to-valley wavefront error associated with spatial quantization is given by the expression,

$$PV = \left. \frac{\partial W(x,y)}{\partial x} \right|_{max} \cdot \Delta \ell \quad , \tag{2.45}$$

where $\Delta \ell$ is a resolution cell dimension. This error is often estimated visually directly from a photograph by counting the number of resolution cells across one fringe period. The contour interval is generally known from the experimental set-up used in producing and recording the fringe pattern. The peak-to-valley error is then given by the ratio of the interval to the number of resolution cells.

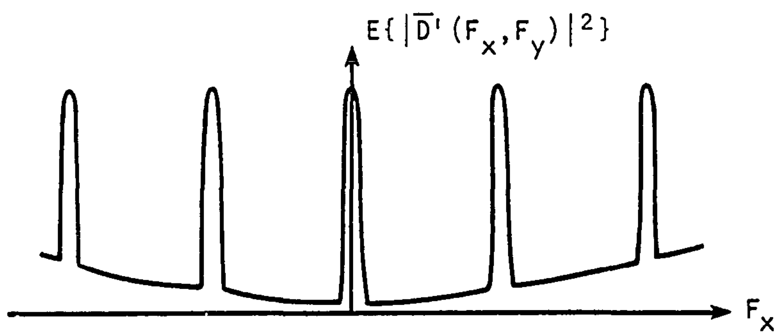


Figure 10. Cross-section of the ensemble average of the jittered data spectrum showing discrete and continuous components.

Ideal sample array is assumed to be uniform.

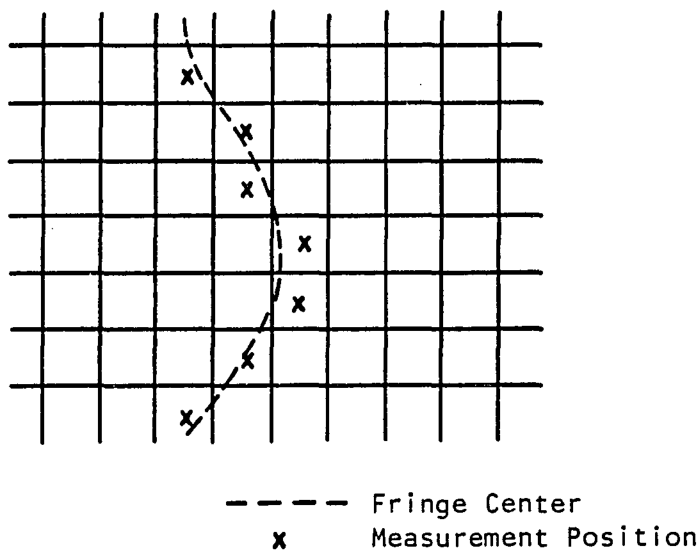


Figure 11. Error due to spatial quantization.

Nonuniform Envelope

A nonuniform fringe pattern envelope causes a small shift in the location of fringe extrema which affects sample positions. To estimate the magnitude of this shift consider a fringe pattern described by the expression,

$$I(x) = I_o(1 + \alpha x) \cdot (1 + K \cdot \cos 2\pi F_x x) \qquad K \leqslant 1 \quad , \qquad (2.46)$$

where $\alpha$ is the slope of the envelope and K allows for fringe visibilities less than one. Let's compute the shift in fringe extrema by taking the first and second derivatives of Eq. (2.46),

$$\frac{dI}{dx} = I_o\{\alpha + K\alpha \cdot \cos 2\pi F_x x - 2\pi F_x K \sin 2\pi F_x x \cdot [1+\alpha x]\} \qquad (2.47)$$

$$\frac{d^2I}{dx^2} = I_o\{-K\alpha 2\pi F_x \sin 2\pi F_x x - (2\pi F_x)^2 K \cos 2\pi F_x x \cdot [1+\alpha x] - 2\pi F_x K\alpha \sin 2\pi F_x x\} \quad . \qquad (2.48)$$

At the ideal positions for fringe extrema corresponding to the argument of the cosine equal to $\pm\pi(2N)$ and $\pm\pi(2N+1)$ for peaks and minima, respectively, these expressions reduce to the following,

$$\left.\frac{dI}{dx}\right|_{\text{extrema}} = \begin{cases} \alpha(1+K)I_o & \text{PEAK} \\ \alpha(1-K)I_o & \text{MINIMA} \end{cases} \qquad (2.49)$$

$$\left.\frac{d^2I}{dx^2}\right|_{\text{extrema}} = \begin{cases} -(2\pi F_x)^2 K[1+\alpha x]I_o & \text{PEAK} \\ +(2\pi F_x)^2 K[1+\alpha x]I_o & \text{MINIMA} \end{cases} \qquad (2.50)$$

From the illustration in Figure 12 the shift in extrema is approximately equal to the ratio of the first and second derivatives at the ideal peak location. The shift due to a nonuniform envelope is therefore given by

$$\Delta x = \begin{cases} \dfrac{-\alpha}{(2\pi F_x)^2} \cdot \dfrac{(1+K)}{K} \cdot \dfrac{1}{1+\alpha x} & \text{PEAK} \\[2ex] \dfrac{\alpha}{(2\pi F_x)^2} \cdot \dfrac{(1-K)}{K} \cdot \dfrac{1}{1+\alpha x} & \text{MINIMA} \end{cases} \tag{2.51}$$

Note that due to the factor $(1 \pm K)/K$ the affect of the nonuniform slope upon a low visibility fringe pattern is greater than the affect on a high visibility pattern. For the relatively severe envelope slope of $1/P$ and letting $K=1$ and $F_x = 1/P$, the shift $\Delta x \approx \frac{P}{36}$ for peaks and $\Delta x = 0$ for minima.

Rather than directly detect peaks or minima, the locations of fringe centers can be estimated from the transitions of a binarized fringe pattern produced by thresholding the irradiance distribution. The simplest estimate is to take the midpoint between transitions as the fringe center. The effect of a nonuniform envelope upon sample points chosen in this way can be estimated in the manner shown in Figure 13. Let the envelope again be linear as in Eq. (2.46). Point B in the illustration is raised vertically from the it's position for a uniform envelope by an amount $\alpha(x_B - x_A)$. If the transition is near the local mean level for the fringe pattern, then the slope at point C is approximately $2\pi F_x$. The error $\Delta x$ in the fringe center estimate is given by

(a)

(b)

(c)

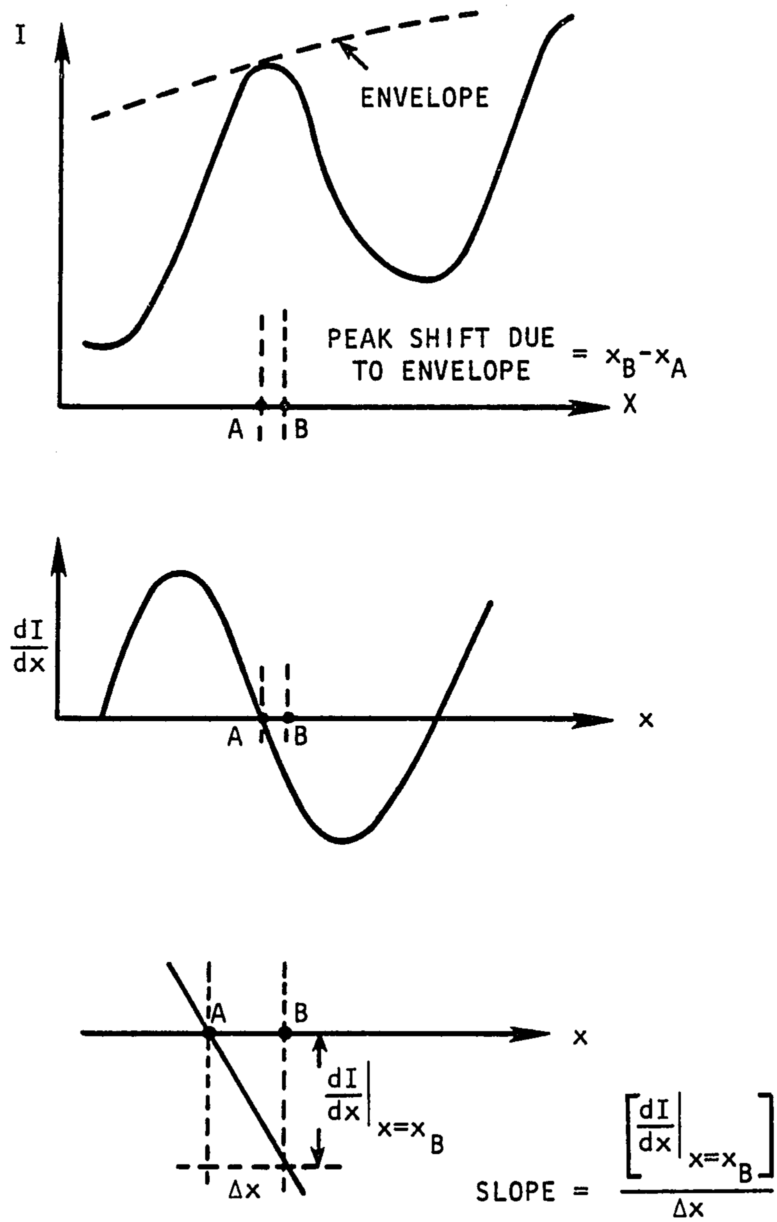


Figure 12. Peak shift due to nonuniform envelope.

(a) Fringe profile.
(b) 1st derivative of profile.
(c) Derivation of error expression.

(a)

(b)

(c)

(d)

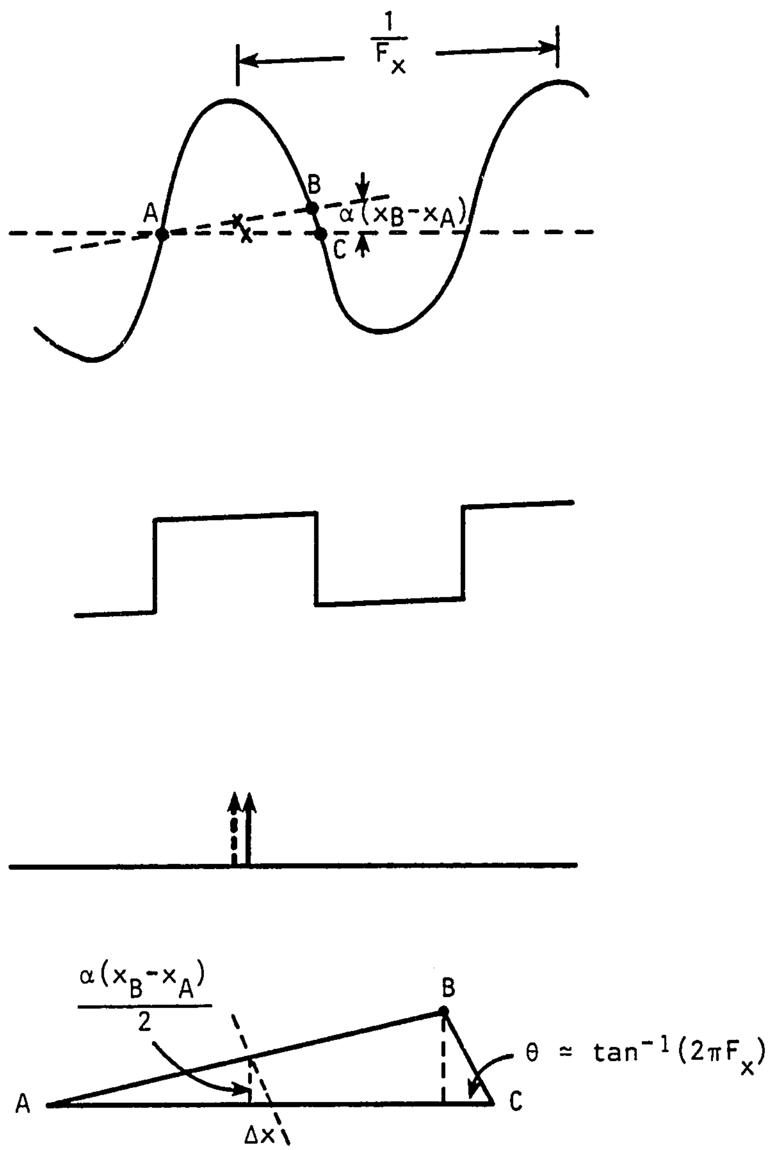


Figure 13. Effect of nonuniform envelope on fringe center acquisition by thresholding.

(a) Fringe profile.
(b) Binarized profile after thresholding.
(c) Fringe center estimate error.
(d) Derivation of error expression.

$$\Delta x = \frac{\alpha(x_B - x_A)}{4\pi F_x K} \quad . \tag{2.52}$$

Notice that the error increases as the fringe visibility decreases. For $\alpha = \frac{P}{10}$, $F_x = 1/P$, $K = 1$, and $x_B - x_A = P/2$, the error $\Delta x \cong P/250$.

Geometric Distortion

Distortion which occurs in imaging a fringe pattern photograph onto a detector surface and in scanning the image contributes to the sample position error. Typically, distortion associated with the imaging lens design and electron optics in the scanner has the form of a radial displacement proportional to the cube of the field height or the square of field height if distortion is expressed as a percentage. Distortion causes a square in the object plane to assume a pin-cushion or barrel shape in the image. Commercial electron beam scanners such as vidicon and image dissector cameras typically have 1 to 2% distortion. With special deflection electronics this scan error can be reduced by an order of magnitude. Commercial copy lenses designed for specific magnification and conjugate distances are available which have distortions of less than 0.1%.

An additional geometric distortion may occur in imaging a fringe pattern photograph onto a detector plane due to tilt of the photograph and detector planes with respect to the paraxial object and image planes. A tolerance for these tilt angles can be estimated through consideration of the illustration in Figure 14. By similar triangles the fractional error in image height due to the tilt is given by

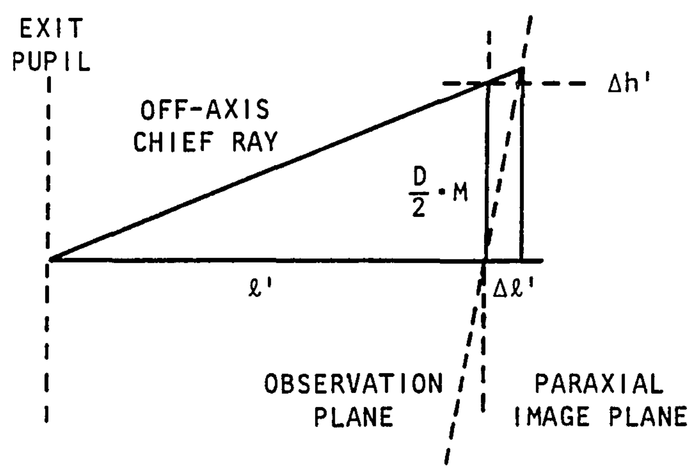


Figure 14. Geometry in image space illustrating source of geometric distortion due to tilted observation plane.

$$E = \frac{\Delta h'}{\frac{D}{2} \cdot M} = \frac{\Delta \ell'}{\ell'} \quad . \tag{2.53}$$

Using the fact that the image distance is one plus the magnification times the focal length, the tilt angle is given by

$$\theta_i \cong \frac{\Delta \ell'}{\frac{D}{2} \cdot M} = \frac{\ell' \cdot E}{\frac{D}{2} \cdot M} = \frac{[(1+M)f] \cdot E}{\frac{D}{2} \cdot M}$$

$$= \frac{2[1 + \frac{1}{M}]f \cdot E}{D} \quad . \tag{2.54}$$

Similarly for a tilt of the photograph,

$$\theta_o \cong \frac{\Delta \ell}{\frac{D}{2}} = \frac{\ell \cdot E}{D/2} = \frac{2[1 + \frac{1}{M}]f \cdot E}{D} \quad . \tag{2.55}$$

The tilt expressions are therefore identical. For 0.1% distortion or $E = .001$, $f = 100$ mm, $M = 0.25$, and $D = 10$ cm, the tilt angle should be less than 10 mrad.

Interference Fringes

Most interferometers incorporate as part of their design a lens for imaging the exit pupil of the optics under test onto an output film plane. Errors occur due to this lens which affect fringe positions and hence the location of sample points for the following reasons,

(1) The interference of two spherical wavefronts yields fringes which lie along hyperboloid surfaces (Hecht and Zajac, 1974; Slomba and Figoski, 1978).

(2) Due to the angle between reference and test beams the two wavefronts acquire different aberrations from the imaging optics (Slomba and Figoski, 1978).

The hyperboloid surfaces for bright fringes satisfy the following interference condition,

$$m\lambda = \sqrt{(y-c)^2+x^2+z^2} - \sqrt{(y+c)^2+x^2+z^2} \quad , \tag{2.56}$$

where the parameters are defined in Figure 15. If observation is restricted to a region near the intersection of the observation plane with the perpendicular bisector of a line drawn between the two sources, the fringes are relatively straight with period given by

$$\frac{1}{F_o} = \frac{\lambda x}{2c} \quad . \tag{2.57}$$

The hyperbolic error in a fringe pattern containing M fringes across a circular pupil can be estimated by substituting the y-value for the edge of the pupil ($y = M/2F_o$) into Eq. (2.56). Figure 16 presents the hyperbolic error in units of fringe periods as a function of the number of fringes across a circular pupil. The figure indicates there is a rapid increase in error as the fringe density increases. The hyperbolic error can be eliminated by locating a lens between the point sources and film plane such that the two interfering wavefronts are collimated and the virtual point sources are essentially an infinite distance away. Slomba and Figoski (1978) have described the design of a telecentric relay which yields fringe patterns free of hyperbolic error and that

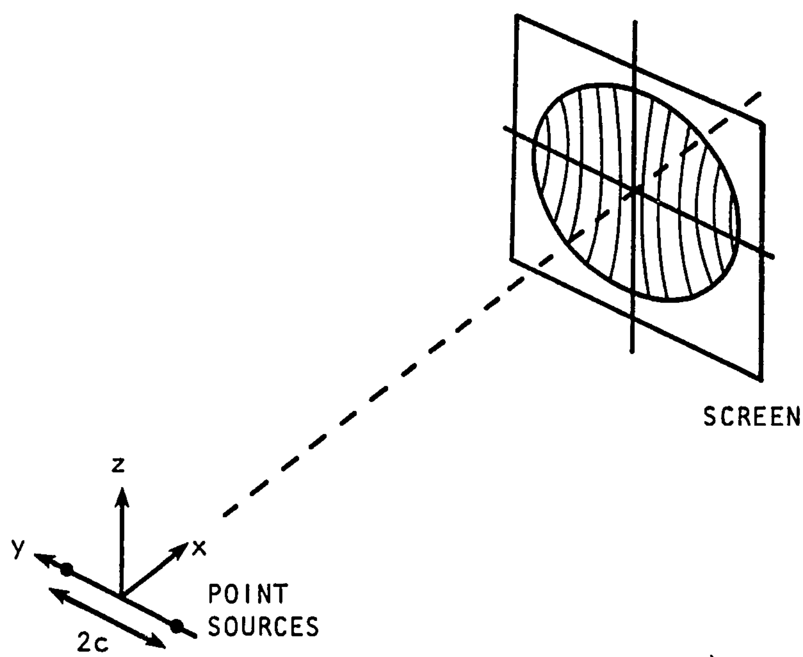


Figure 15. Hyperbolic fringe pattern due to illumination by two point sources.

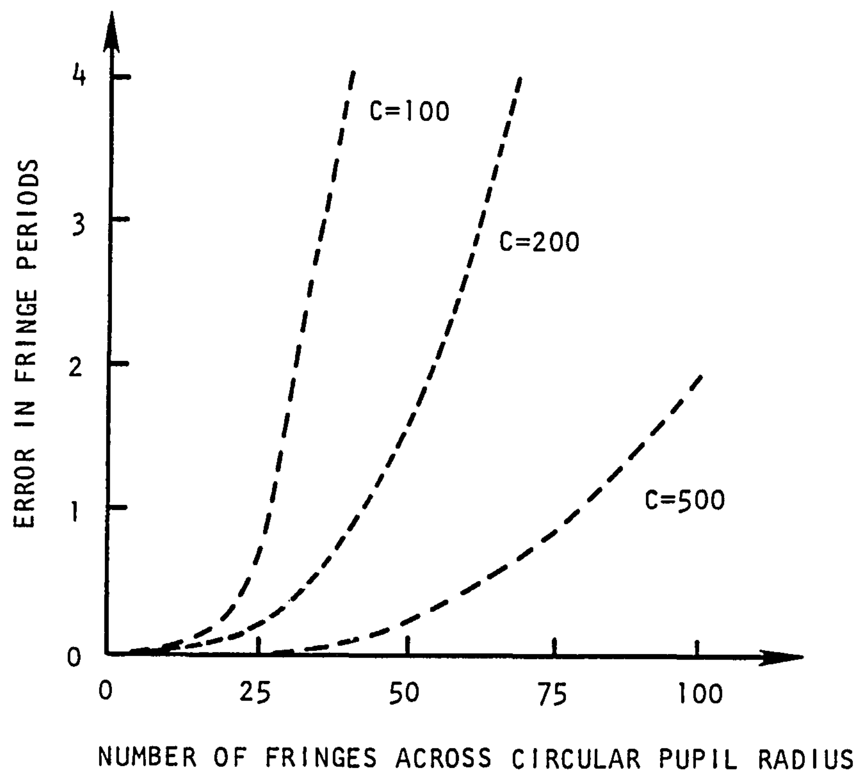


Figure 16. Hyperbolic error due to interference between two spherical wavefronts for a distance of 10 cm between sources and the observation screen.

Parameter C is in units of wavelength.

also introduces negligible aberration due to the different propagation paths of reference and test beams through the relay.

## Fringe Scanning Devices

### Graphics Tablet

Interferogram analysis systems that use a graphics tablet for selecting points at fringe centers are currently in use at Oak Ridge, Los Alamos, Honeywell, Lockheed, TRW, the University of Arizona, and other facilities. The tablet provides x-y coordinates to an external computer marking the position of a cursor cross-hair or stylus on a platen surface. The platen contains wires which are parallel to the x and y axes and uniformly spaced. These interact with the cursor usually by magnetostrictive, capacitive, or inductive mechanisms. The operator places the fringe pattern photograph on the tablet surface, tapes it flat, and marks four fiducial points at the top, bottom, right, and left of the fringe pattern indicating the borders of the pupil. Data is taken at random positions along the full length of a fringe after which a command to the external computer increments the order number. The procedure is repeated for the next fringe and continues until the entire fringe pattern has been sampled.

In magnetostrictive tablets the x and y sets of wires are magnetic and the cursor contains a multiple turn coil centered on the cross-hair (Whetstone, 1980). A strain pulse is launched simultaneously along each of the wires in either set depending upon whether the x-coordinate or the y-coordinate is being measured. Due to magnetostriction the field surrounding the wires is disturbed as the strain pulse propagates and the flux change is detected by the cursor coil. A pulse velocity of approximately five thousand meters/second and a pulse length of 50 nano-seconds yield a pulse width of approximately 0.25 mm which determines the resolution of the tablet.

Tablets based upon capacitive coupling between the x and y sets of wires and a stylus tip are also common (Stavely, 1981; Cardwell, 1981). In this scheme wires are located several millimeters apart typically on a double-sided PC board imbedded in plastic. Each wire is connected to an output pin of a daisy chain of serial-to-parallel shift registers. A periodic digitial signal propagating through one of the two sets of shift registers produces by capacitive coupling a signal of the same frequency at the stylus tip but shifted in phase by an amount dependent upon the stylus position. If the period of the digital wave-form is less than the tablet width, more than one frequency may be used in order to resolve the modulo-pi phase ambiguity. A resolution of 0.25 mm is achievable by this method.

Inductive tablets have a primary coil winding located in the cursor that is driven by a sinusoidal source. A voltage is induced in secondary loops imbedded in the platen surface. The latter are formed by connecting the x and y sets of wires in common along two edges of the tablet. Each individual wire is electrically scanned at the opposite end. The induced voltage is measured and the cursor position is esti-mated by interpolation.

Advantages of the graphics tablet for fringe scanning include the following:

(1) Easy to interface and use--suitable for an unskilled operator.

(2) Inexpensive--less than $1 K for an 11 inch square tablet.

(3) High resolution--generally 1 to 2 hundred points per inch.

Disadvantages include:

(1) Sample points occur at random positions along each fringe.

(2) Operator must visually estimate fringe center location.

(3) Tedious and time-consuming if a large number of data points are taken.

Electron Beam Scanners

Vidicons have been the most popular type of electron beam imager for scanning fringe patterns largely due to the success of the Zapp fringe pattern analyzer of the Zygo Corporation. The operation of vidicons (Talmi, 1975) is based upon a capacitive storage target which is illuminated by an optical image on the faceplate surface while the rear surface is scanned by an electron beam. Two types of target designs are available. One is photoconductive with the most common materials being antimony trisulfide and lead oxide. The former is associated with high sensitivity and nonlinear response. The latter is known for its exceptionally good lag characteristic. The other type of target consists of a dense array of P-N junctions on a silicon wafer with reverse bias maintained by the scanning electron beam. Silicon vidicons are known for their linear response and a spectral sensitivity that extends into the near infrared. In both types of targets hole-electron pairs generated by the incident illumination discharge the target. The next pass of the electron beam restores the charge drained away by carrier generation. The recharge current flows through a load resistance producing a voltage that represents the information signal. Variations upon this fundamental design include the following:

(1) An electron imaging stage is located between the target and a photosensitive surface at the faceplate. The target is thus bombarded by high-energy electrons which are far more efficient producers of hole-electron pairs than optical illumination. Target gains of several thousand are realized. Silicon intensifier tubes (SIT) are an example of this type of tube.

(2) Instead of deriving the video signal from the charge absorbed at the target, the portion of the electron beam reflected or scattered from the target is intercepted and amplified to obtain a video signal. Image isocons and silicon return beam vidicons use this type of readout.

Table 1 presents a performance/price description of some commercially available vidicon cameras. The primary method of achieving higher resolution in vidicon tubes is to increase target diameter. The most common diameters are 2/3" and 1". Vidicon tubes are readily available with all the required electronics in the form of inexpensive CCTV cameras.

Image dissector tubes are distinguished from other electron beam imagers in that there is no integrating target. The tube consists of a

Table 1. Characteristics of commercial electronic scanners.

| | S/N | CENTER RESOLUTION (LINE PAIRS) | DIAMETER | SHADING | DISTORTION | PRICE |
|---|---|---|---|---|---|---|
| VIDICON CAMERAS | 40 db | 300 | 16 mm | <10% | ±1% | 0.4K |
| | 40 db | 500 | 16 mm | <10% | ±1% | 5.0K |
| | 40 db | 750 | 25 mm | <10% | ±1% | 9.0K |

| | S/N | ADDRESSABLE POINTS | DIAMETER | NONUNIFORMITY OF RESPONSE | DISTORTION | PRICE |
|---|---|---|---|---|---|---|
| IMAGE DISSECTOR | PROPORTIONAL TO SQUARE ROOT EXPOSURE & TIME | 2048×2048 | 43 mm | ±15% | ±3% | 16.0K |

| | GEOMETRY | NO. OF ELEMENTS | DYNAMIC RANGE | SPACING | NONUNIFORM RESPONSE | MAXIMUM FREQUENCY | PRICE |
|---|---|---|---|---|---|---|---|
| PHOTODIODE ARRAYS | LINEAR | 128 | >100:1 | 25μ | 4% | 2 MHz | 0.1K |
| | LINEAR | 1024 | >100:1 | 25μ | 7% | 2 MHz | 0.6K |
| | LINEAR | 1728 | >200:1 | 15μ | 10% | 3 MHz | 3.0K |
| | LINEAR | 100×100 | >200:1 | 60μ | 5% | 10 MHz | 1.5-3.0K |

| | GEOMETRY | NO. OF ELEMENTS | DYNAMIC RANGE | SPACING | NONUNIFORM RESPONSE | MAXIMUM FREQUENCY | PRICE |
|---|---|---|---|---|---|---|---|
| CCD ARRAYS | LINEAR | 256 | 2500:1 | 13μ | 10-20% | 10 MHz | 0.1K |
| | LINEAR | 2048 | 2500:1 | 13μ | 10-20% | 20 MHz | 1.1K |
| | AREA | 400×380 | 1000:1 | 30μ hori. 18μ vert. | 1% | 20 MHz | 5.0K |

| | GEOMETRY | NO. OF ELEMENTS | DYNAMIC RANGE | MAXIMUM FREQUENCY | PRICE |
|---|---|---|---|---|---|
| CID ARRAYS | AREA | 42×342 | 256:1 | 3.5 MHz | 2.0K |
| | AREA | 128×128 | 256:1 | 7.0 MHz | 1.0K |
| | AREA | 244×248 | - | 4.5 MHz | 3.5K |

photoemissive surface that upon illumination produces photoelectrons. These are imaged onto a mask containing a small aperture. The electron image is positioned with respect to the aperture by x-y deflection fields. Electrons passing through the aperture are multiplied by several stages of amplification in the same manner as a photomultiplier tube. The size of the mask aperture determines the resolution. Commercial dissectors have resolutions as large as 2048 x 2048 points at a cost of $15 to $20 K. Special options are available to reduce distortion to approximately 0.2%.

Solid State Scanners

Three types of solid state arrays--silicon photodiode, charge-coupled detector (CCD), and charge-injection devices (CID)--are of interest for fringe scanning. Compared with vidicons these devices have the advantages of small size, low voltage, high scan rate, linear response, and freedom from geometric distortion.

Silicon photodiode arrays consist of discrete P-N diodes each with an associated parallel capacitance which is charged so as to reverse bias the junction (Reticon, 1981). Incident illumination creates hole-electron pairs which discharge the capacitance. A digital shift register scans the array recharging the diode capacitance through analog switches connected to each photodiode. The recharge current is the information signal.

CCD arrays do not use P-N junctions as the photosensitive element. Instead an array of electrodes is deposited on the surface of P-type silicon. Voltages applied to the electrodes create depletion zones that store charge produced by illumination until readout. Applying voltages to the neighboring electrodes in a certain time sequence shifts charge from one potential well to the next. Array readout thus occurs in the manner of an analog shift register (Fairchild, 1981).

CID arrays resemble CCD arrays in structure with the major difference being that neighboring pairs of electrodes constitute a single x-y address. Readout occurs by removing voltage from one electrode which causes charge to be transferred to the second potential well of the x-y electrode pair. Then removing voltage from the second electrode injects charge into the substrate. The injection current is the information signal. CID's are potentially capable of random access addressing (Talmi, 1975).

For years the major difficulty in applying two-dimensional arrays to fringe scanning has been their low resolution. However, CCD arrays are now available off-the-shelf with resolutions as high as 488 x 380 and there are reports in the literature of arrays as large as 800 x 800. CID and silicon photodiode arrays are currently available in formats as large as 244 x 248 and 100 x 100, respectively.

A linear array in combination with a mechanical scan perpendicular to the array is an attractive alternative to the use of two-dimensional arrays for digitizing fringe patterns (Eikonix, 1981). In this way two-dimensional scans with resolutions of 2048 x 2048 points are achieved with negligible distortion and scan times as fast as 35 seconds. Table 1 presents specifications for several commercial solid-state arrays.

## Fringe Center Acquisition

### Introduction

Numerous analog and digital techniques are available for acquiring the coordinates of fringe centers from a scanner signal. These include

(1) Detection of zero crossings of a differentiated video signal.

(2) Switching a voltage comparator on the direct video signal or the filtered video, storing the comparator output in video memory, and using software to estimate the fringe center coordinates.

(3) Fitting a polynomial to digitized samples obtained from the vicinity of a fringe peak or minima.

(4) Tracing along fringe maxima or minima using a correlation window applied to the digitized image.

### Differentiation

Differentiator circuits usually rely upon the derivative relationship which exists between the current and voltage across a capacitor. This current is given by

$$I = \frac{dQ}{dt} = C \cdot \frac{dV_c}{dt} \quad . \tag{2.58}$$

If the current flow is sinusoidal then the voltage across the capacitor is shifted in phase by 90 degrees. By adding a load resistor in series with the capacitor a high pass filter is created with the load voltage intrinsically 90 degrees shifted with respect to the voltage across the capacitor. If the reactance of the capacitor ($1/\omega c$) is much greater than the load resistance, then most of the input voltage (see Figure 17a) is dropped across the capacitor and the input-output equation becomes

$$V_{out} = I \cdot R = RC \cdot \frac{dV_c}{dt} \cong RC \cdot \frac{dV_{in}}{dt} \quad . \tag{2.59}$$

Due to the dependence of this approximation upon the relative impedances of the capacitor and the load, differentiation by an RC filter is associated with strong attenuation of the input sinusoidal signal and with a phase shift which is exactly 90 degrees only in the limit in which the frequency goes to zero. At $\omega = \frac{1}{2\pi RC}$ (the 3-db point of the filter) the impedances are equal and the phase shift is 45 degrees with an attenuation of 71 per cent. For a fringe pattern this corresponds to 1/8 of the fringe period. Assuming that fringe scanning occurs from left to right, zero crossings of the filter output, which ideally give the location of fringe extrema, are shifted to the right due to the non-ideal phase delay. If the spatial period of the fringe pattern is constant then error due to the phase delay is also constant across the pattern and will have no effect upon the subsequent analysis. Another problem with RC-type differentiators is that frequency components higher than the 3-db frequency are passed with small attenuation compared with that applied to the signal. The op-amp differentiator shown in Figure 17b partially overcomes these faults. Because the op-amp maintains virtual ground at its negative terminal, it represents a nearly ideal load impedance for the capacitor. In addition the capacitor across the feedback resistor limits the high frequency response reducing the effect of noise.

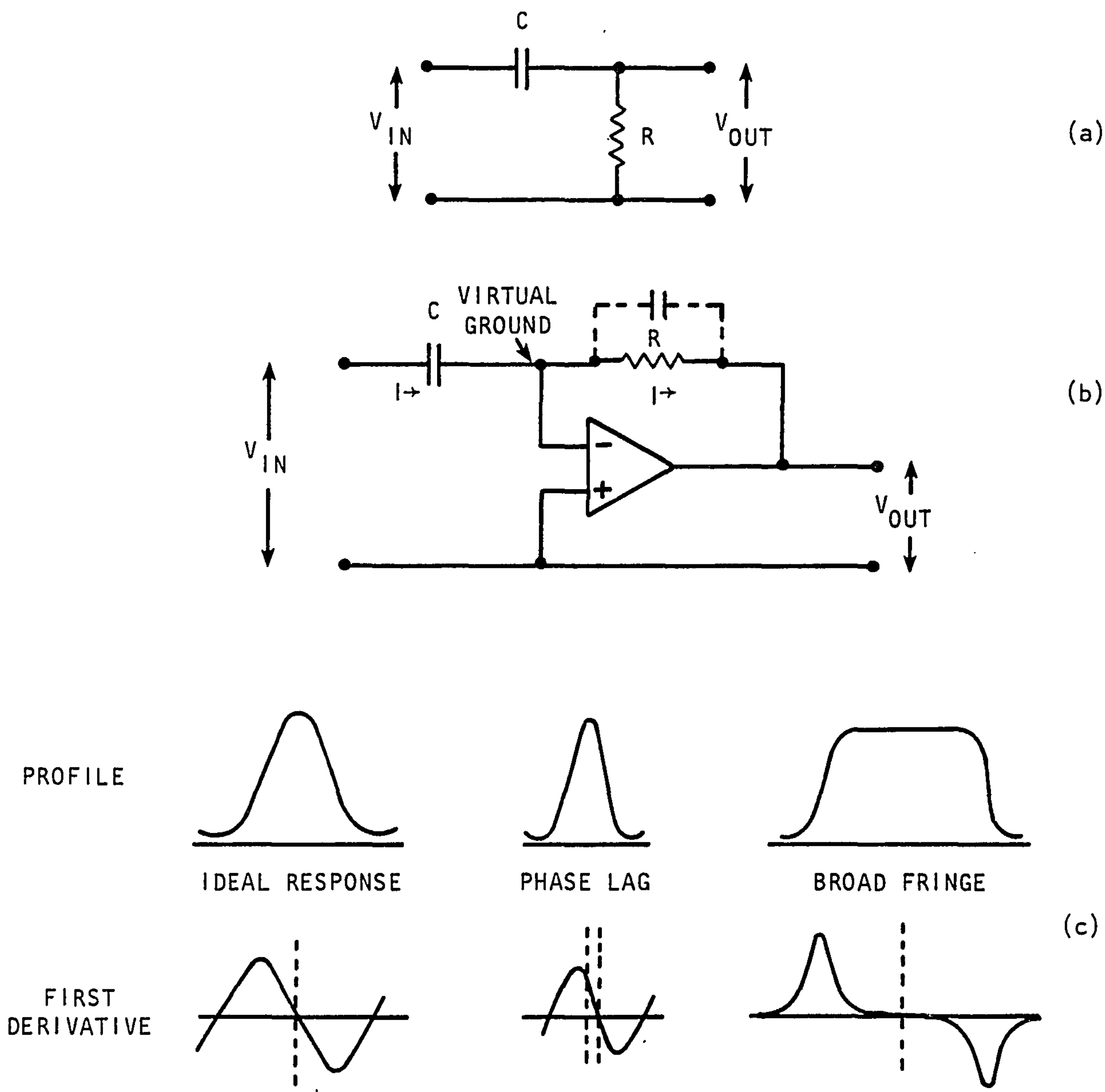


Figure 17. Detecting fringe extremes by differentiation.

(a) RC differentiation.
(b) op-amp differentiation.
(c) Fringe profiles and their first derivatives.

A variation upon the basic differentiation circuit involves limiting zero-crossing detection to a window determined by thresholding the derivative of the signal (Zanoni, 1979). This helps discriminate against spurious zero crossings due to noise. Zygo Corporation has marketed a fringe pattern analyzer based upon this approach (Augustyn et al., 1978). Using a vidicon camera for scanning, their system operates with up to 25 fringes and locates fringe centers on 25 video lines. A reference clock provides 1000 resolution elements per line.

Binarization

Thresholding is a technique for locating fringe centers in which a binarized representation of the fringe pattern is produced by point operations defined by the following transformation

$$B(I,J) = \begin{cases} 1 & P(I,J)>T \\ 0 & P(I,J)<T \end{cases} , \qquad (2.60)$$

where P(I,J) is the pixel value at the ith row and jth column and T is the threshold value (Jones, 1977). If the fringe pattern has a non-uniform envelope, it may be necessary to vary T as function of position in order to sample the entire fringe pattern. The midpoint error that occurs due to a nonuniform envelope was described in an earlier section.

Womack et al. (1979) took an approach in which a video signal was thresholded in real time by a voltage comparator. The comparator output was passed through a 4-out-of-6 majority circuit before storing the binary output in a microcomputer's memory. This helped eliminate spurious pulses due to the comparator switching on video noise. The binary fringe pattern was scanned horizontally to locate transition points from which fringe centers were estimated by calculating the mean for successive pairs of transitions. Resolution of the frame store was 480 x 512 x 1. A data subset from the lines at fringe centers was chosen for analysis with the number and location of points determined by the operator. Visual editing and fringe order assignment were implemented in software with interactive control. A detailed description of this system is included later in this chapter.

Jones (1977) has applied a midpoint thinning algorithm originated by Stefanelli and Rosenfeld (1971) to estimate fringe centers from a binary fringe pattern. Arcelli, Cordella and Levialdi (1979) have described an improved version of the thinning algorithm. In this scheme the pattern is scanned repeatedly with edge points eliminated until only the midline remains. This technique is capable of handling closed binary fringe patterns.

## Least Squares Fit

A method for reducing the effect of high frequency noise on fringe center acquisition is to perform local least squares polynomial fits. Bernal and Loomis (1977) have described a video system in which polynomials of the form

$$I(X) = A + B \cdot X + C \cdot X^2 \tag{2.61}$$

were fit to the vicinity of fringe maxima and minima. The extrema of the parabolic fit were taken as fringe center locations.

Glassman and Orr (1979) performed straight line fits in the regions of maximum slope for scans across a fringe pattern. They took the intersection of the straight lines as the fringe center and the distance between midpoints for successive line segments as the fringe period. The latter was useful for handling closed fringes since the periods for vertical and horizontal scans could be compared and a best choice made for which scan to use for the fringe center estimate.

Correlation

By convolving a fringe pattern with a symmetric window, high frequency noise is attenuated and fringe centers can be located with a simple algorithm for extracting local extrema. Snyder (1980) has analyzed the effect of a nonuniform envelope on a one-dimensional sinusoidal signal convolved with a symmetric window. To obtain high precision phase measurements he chooses the filter width such that error due to the nonuniform envelope at peaks is opposite the error at minima. A least squares fit of a straight line to extrema of the filtered signal is then used to interpolate phase values across the fringe pattern.

Funnell (1981) applied the correlation window concept to two-dimensional closed fringe patterns. Rather than perform the filter operation on the entire fringe pattern before proceeding with location of extrema, he reports scanning the window in the vicinity of extrema so as to trace out a complete fringe before moving on to an adjacent fringe.

# A Microprocessor-Based Video Interferogram Analysis System

## General Description

In 1979 a video interferogram analysis system was developed at the Optical Sciences Center that used the traditional approach to measure peak-to-valley and rms wavefront deviation, aberration coefficients and other optical parameters (Womack et al., 1979; Womack, 1980). It consisted of a portable rack containing a video processor, a PDP 11/03 with dual 8-inch disk drives, and a photomodule as shown in Figure 18. The photomodule provided polaroid photographs of the monitor screen and also contained a television camera and a built-in photo-easel for working with interferogram photographs. Hardware also included a printer, an x-y plotter, and a CRT terminal modified for displaying graphics.

The system was designed to work with interferogram photographs or with the direct interferometer output. A TV camera was interfaced to a Z-80 microcomputer in such a way that a single video image of an interferogram was captured at a resolution of 480 x 512 x 1. In seconds, continuous white lines were obtained at the centers of dark fringes. The operator proceeded through steps that included editing the interferogram, selecting a reduced data set for analysis, and assigning order numbers to fringes. Data was passed to a PDP 11/03 microcomputer, which performed a 36-term Zernike polynomial fit. Various parameters were computed and graphics output was generated.

Figure 18. Video interferogram analysis system.

## Video Processor

A block diagram of the video processor is presented in Figure 19. Signal processing options included the direct comparator with a choice of two high-pass filters, an adjustable comparator threshold, and 4-out-of-6 majority logic. Controls were located on the front panel of the video processor. The comparator output was fed to an 8-bit shift register that drove a prom pattern recognizer. If any 4 of 6 consecutive pixels were "on," the prom output a logic one. This contributed to noise immunity. Depending on the condition of control lines, this modified comparator output was either loaded into the lower 32 kbytes of Z-80 memory or passed directly to the video combiner so that a digitized interferogram was viewed in real time. When not viewing in real time, the lower 32 kbytes of memory were fed serially to the video combiner, allowing the operator to observe the stored comparator output or the output after software processing. Locating the video memory in the address space of the Z-80 contributed to the speed of certain algorithms and was also convenient for system development since the Z-80's monitor program could directly manipulate video memory for setting up test patterns and examining processed patterns.

## Operation

The chief objective of interferogram digitization is to acquire the coordinates of fringe centers and to properly assign consecutive integers to the points along each fringe. Figure 20d illustrates the end result with integers appearing at the tops of lines drawn at the

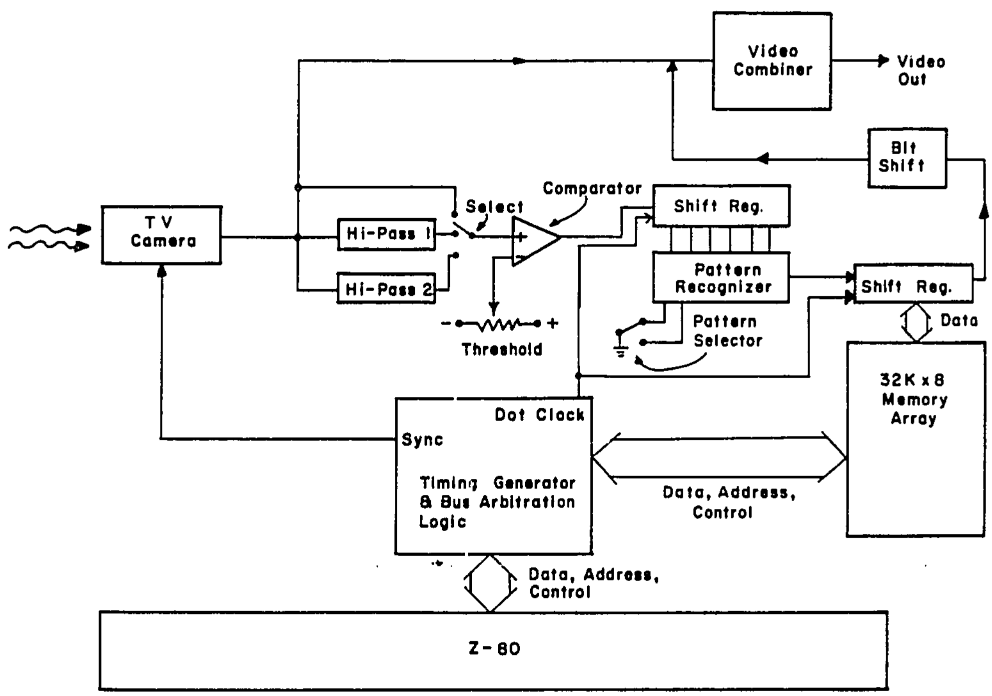


Figure 19. Block diagram of video processor.

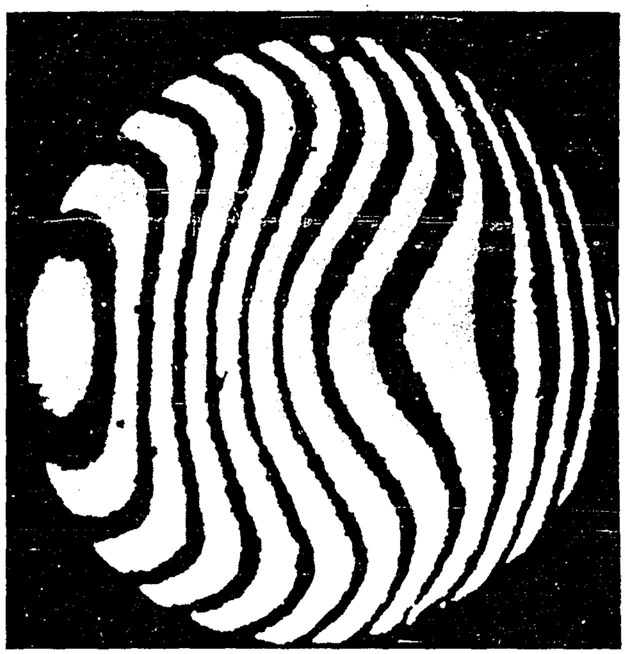

(a)

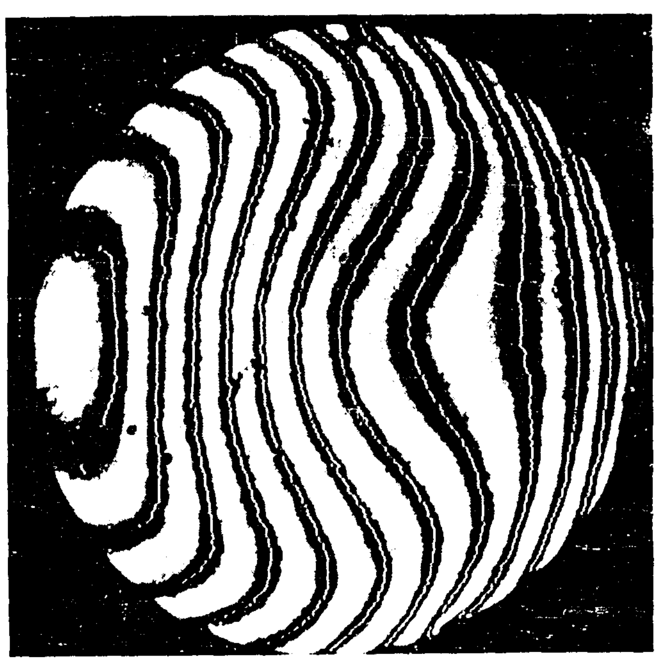

(b)

Figure 20. Video output.

(a) Digitized interferogram.
(b) Lines at fringe center.

(c) 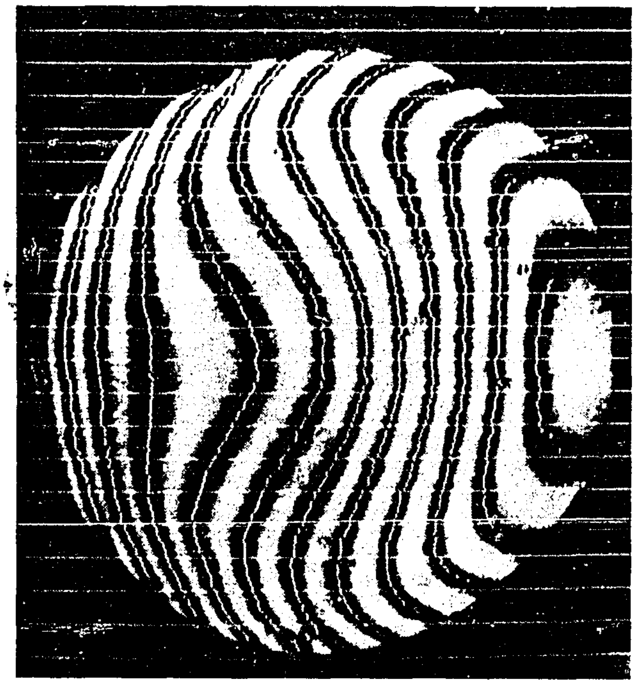

(d) 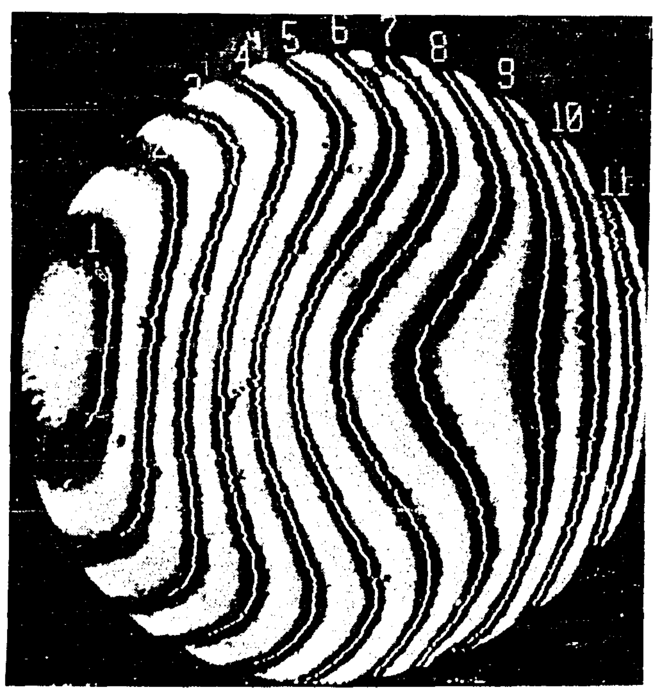


Figure 20.--<u>Continued</u>

(c) Data selection.
(d) Order assignment.

centers of dark fringes. The video system was used in three ways for producing lines at fringe centers:

(1) Manual Data Entry - Successive line segments were manually drawn at fringe centers with the aid of a cursor superimposed upon the video image.

(2) Single Digitization - The interferogram was sampled once with the video comparator and the center-finding routine was run to have the computer draw lines at fringe centers in a matter of seconds. This method was used for high visibility interferograms.

(3) Multiple Digitization - The interferogram was sampled several times at comparator threshold levels selected by the user. The center-finding routine was run at each step and lines obtained from each sampling were combined into an overall result. This method was used for low visibility interferograms and interferograms for which the fringe pattern had a nonuniform envelope.

The seven steps listed below were required to process an interferogram using the automatic features for locating fringe centers.

(1) Define the pupil.

(2) Digitize.

(3) Edit, if necessary.

(4) Select data.

(5) Assign order numbers.

(6) Set up the analysis program.

(7) Transfer data and run the program.

The major system functions were controlled by user-definable keys of the terminal keyboard. At turn-on, a message was displayed indicating these special keys were enabled. The operator pressed DIGITIZE and observed the digitized version of the interferogram in real time as signal processing controls were adjusted. Inspecting the digital image, the operator again pressed DIGITIZE, capturing a single video frame of the comparator output, as shown in Figure 20a. An algorithm was then executed that drew continuous lines at the centers of dark fringes in less than 12 seconds. An example of the resulting display is illustrated in Figure 20b.

When EDIT was pressed, a double-arrow cursor appeared that was used for adding points, removing points, and drawing line segments as desired. To facilitate edit operations, the double-arrow cursor automatically followed fringes or was directed to jump from one fringe to the next. Joystick control and x-y cursor movement were also provided with fine and coarse motion available at a tap of the space bar. Special routines provided for 11 and 25 point smoothing of the entire interferogram or the particular fringe closest to the cursor.

The DATA SELECT function determined the data set that was used for detailed analysis. Horizontal sample lines, such as those shown in Figure 20c, appeared on the screen. Their intersection with the lines at fringe centers formed the data set. Spacing and offset were adjustable by entering appropriate commands which made the sample line spacing smaller or larger or shifted the array of lines up or down. The number of intersection points was displayed at the upper left of the screen. As the data list was built up in memory, a byte was left blank adjacent to each set of coordinates for later insertion of the order number.

Returning to the EDIT mode, the user positioned the cursor for the order assignment. The command OR assigned consecutive integers to all fringes to the right of the cursor. OL accomplished the corresponding operation to the left of the cursor. Order number sequences such as "1,2,3..." to the right and "1,2,3..." to the left were easily accomplished. A number at the upper left of the screen indicated the next order number to be assigned. It was incremented or decremented by pressing SHIFT # with "+" or "-" determining the direction. Order numbers could also be assigned manually by pointing to a fringe line and pressing ON. To make it clear which points on the screen were interpreted by the computer as a single connected fringe, the fringe was erased and redrawn as the automatic order assignment proceeded from one fringe to the next. Immediately before resetting each pixel along the fringe, a search routine scanned the data list created by DATA SELECT and inserted the order number when a match was found. Order numbers assigned to each fringe were displayed at the top of the fringe, as shown in Figure 20d.

The FRINGE program (Loomis, 1976; Womack, 1980) was the primary analytical tool of the system. It fit a 36-term Zernike polynomial to the data and used this polynomial to generate contour maps, section plots, MTF curves, point spread function plots, and spot diagrams.

Options provided for subtraction of aberrations, averaging, handling obscurations, expressing results in terms of surface or wavefront deviations, printing Zernike coefficients, and much more. Examples of the FRINGE program printout and graphics are presented in Figures 21 and 22. Execution time for the polynomial fit was typically 3 minutes.

Calibration

Geometric distortion was observed to be approximately 1% corresponding to 5 pixels deviation near the edge of a circular pupil having a diameter equal to 80% of the screen height. To correct for this, a calibration procedure was performed after a 15 minute warm-up of the CCTV camera. A calibration photograph consisting of a 5 x 5 array of precisely located circular dots was selected from the available set of calibration targets. The photograph was placed on the photo-easel and a rectangular pupil was defined using appropriate EDIT commands enclosing the array. A binary pattern corresponding to this array of circular dots was captured and reduced by the computer to single pixels displayed at the center of the actual dot video images. The coordinates of these pixels were compared to the coordinates of an ideal grid and numbers corresponding to the x and y errors at each circular dot were displayed immediately above each dot. At the same time a correction map was built up in memory that was applied to the coordinates of data points selected in future analyses. The only visible change in performance was a pause of a few seconds at the end of the DATA SELECT routine followed by a display of the corrected points. The correction map remained intact until power to the video processor was turned off.

50 INCH SPHERE

WVFRONT DEVIATION IN UNITS OF WAVES
TILT AND DEFOCUS MEASURED FROM DIFFRACTION FOCUS
WAVELENGTH 0.633 MICRONS

QUALITY OF FIT FOR DIFFERENT POLYNOMIAL ORDERS

| | N | RMS | MAX |
|---|---|---|---|
| PLANE | 2 | 0.139 | 0.410 |
| SPHERE | 3 | 0.121 | 0.296 |
| 4TH ORDER | 8 | 0.043 | 0.119 |
| 6TH ORDER | 15 | 0.035 | 0.088 |
| 8TH ORDER | 24 | 0.028 | 0.077 |
| COMPLETE | 36 | 0.023 | 0.071 |

STREHL RATIO 0.562 AT BEST FOCUS
TILT 5.506 -2.5 DEG.
FOCUS 0.281

FOURTH ORDER ABERRATIONS

| MAGNITUDE WAVES | ANGLE DEG | DESIGNATION |
|---|---|---|
| 5.506 | -1.4 | TILT |
| -0.011 | | FOCUS |
| 0.548 | -71.0 | ASTIGMATISM |
| 0.165 | -101.4 | COMA |
| 0.003 | | SPHERICAL ABERRATION |

FOLLOWING TERMS WERE SUBTRACTED FROM DATA-

TILT FOCUS

RESIDUAL WVFRONT VARIATIONS EVALUATED AT DATA POINTS

| PTS | RMS | MAX | MIN | SPAN | STREHL |
|---|---|---|---|---|---|
| 143 | 0.121 | 0.296 | -0.246 | 0.542 | 0.561 |

RESIDUAL WVFRONT VARIATIONS OVER UNIFORM MESH

| PTS | RMS | MAX | MIN | SPAN | STREHL |
|---|---|---|---|---|---|
| 592 | 0.120 | 0.336 | -0.242 | 0.578 | 0.566 |

50 INCH SPHERE

| CONTOUR STEP | WIDTH | PAGE SIZE | -M- | -N- | -P- | -Q- |
|---|---|---|---|---|---|---|
| 0.100 | 0.200 | 2.000 | -0.150 | -0.050 | 0.050 | 0.150 |

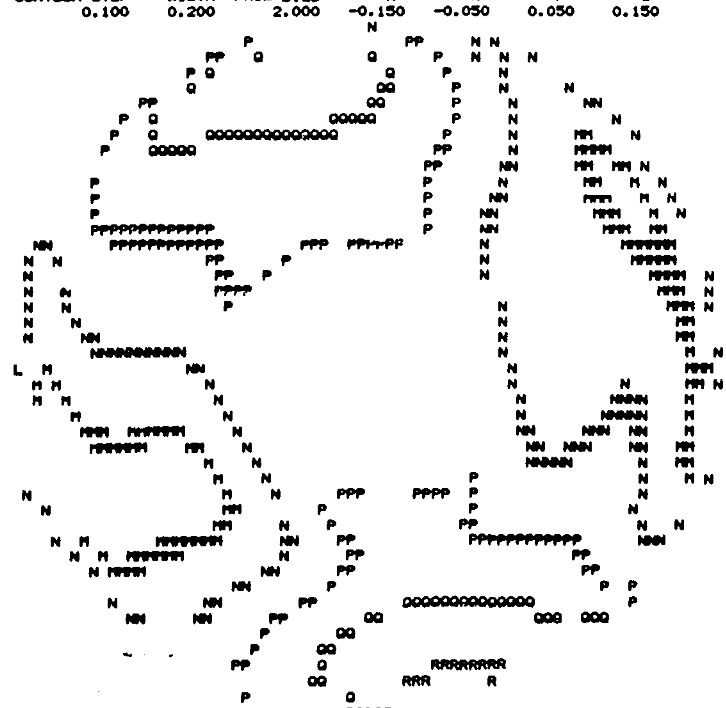

Figure 21. FRINGE program printout.

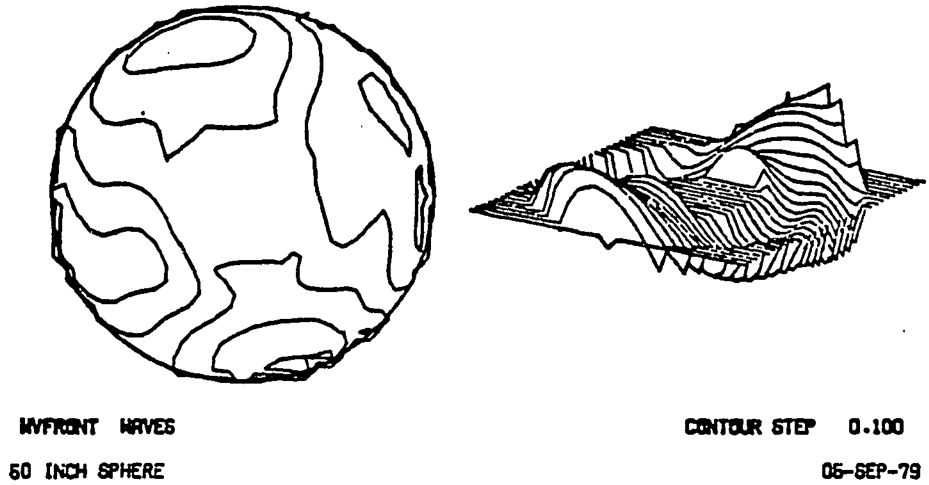


(a)

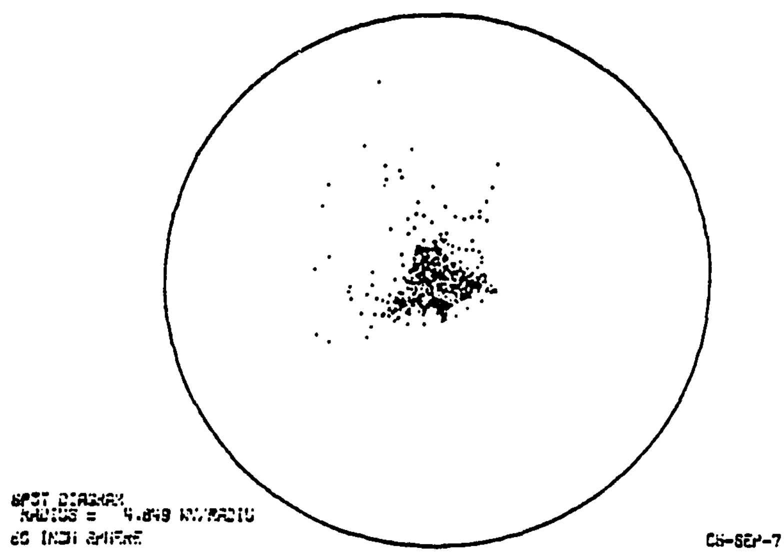

(b)

Figure 22. FRINGE program graphics.

(a) Contour and 3-D.
(b) Spot diagram.

## Summary and Conclusions

The frequency domain spectra for a data set was investigated using binary computer-generated holograms as a conceptual aid. Various sampling schemes were considered and it was concluded that uniform sampling is best. Biased fringe patterns were shown to be preferable to closed patterns. Interpolation in the spatial domain was described as low-pass filtering in the frequency domain. The transfer function associated with spline interpolation was derived. A global least squares fit was presented as a method for recovering the zero order peak of the data spectrum. From consideration of the Fourier transform of Zernike polynomials it was concluded that higher order fit coefficients are more strongly affected by sampling sidelobes than lower order coefficients. Random jitter on a data set gave rise to a continuous component superimposed upon the usual data spectrum. The effect of a non-uniform envelope on a fringe pattern was to shift peaks down-slope and minima up-slope by a small amount. Geometric distortion due to imaging optics, the scanner, and the alignment of the photograph and detector planes with respect to the optical axis all contributed sampling errors. If the fringe pattern originated by interference of two wavefronts, errors arose due to the hyperboloid nature of such fringes and the different propagation paths for the reference and test beams through the imaging optics. Automated systems for traditional analyses have used differentiation, binarization, parabolic fitting, and correlation techniques for locating fringe centers. An example of the binarization approach is a microprocessor-based video system developed at the Optical

Sciences Center that used a single bit frame capture to estimate center locations. To date this system has been used for over 5000 interferogram analyses.

## CHAPTER 3

## SYNCHRONOUS CONVOLUTION METHODS OF FRINGE PATTERN PHASE MEASUREMENT

### Quadrature Multiplicative Moiré (QMM)

#### Concept

Let a fringe pattern be given by

$$I(x,y) = A + B \cdot \cos 2\pi W(x,y) \quad , \tag{3.1}$$

and a reference pattern by

$$R(x,y) = \cos 2\pi W_R(x,y) \quad , \tag{3.2}$$

where $W(x,y)$ and $W_R(x,y)$ represent unknown and known surface deviations, respectively. $I(x,y)$ can be regarded as an image illuminating a detector that is interfaced to a computer. $R(x,y)$ is a mathematical function used by the computer in executing the QMM algorithm. Taking the product of the two fringe patterns, sum and difference terms are generated given by

$$P_1(x,y) = A \cdot \cos 2\pi W_R(x,y) + B \cdot \cos 2\pi [W(x,y) + W_R(x,y)]$$
$$+ B \cdot \cos 2\pi [W(x,y) - W_R(x,y)] \quad . \tag{3.3}$$

If the difference between surfaces is small then the 3rd term represents a low spatial frequency component that can be separated at least partially, if not completely, from the remaining terms by low pass filtering. In the spatial domain this filtering operation corresponds to convolving the product $I(x,y) \cdot R(x,y)$ with a window function. Assuming the filter isolates the difference term perfectly, the resulting low spatial frequency moiré can be written

$$\begin{aligned} M_1(x,y) &= P_1(x,y) * H(x,y) \\ &= B \cdot \cos 2\pi [W(x,y) - W_R(x,y)] \quad . \end{aligned} \tag{3.4}$$

Similarly from the product of the fringe pattern and a reference shifted in phase by 90 degrees with respect to the first, a second low spatial frequency moiré is obtained given by

$$\begin{aligned} M_2(x,y) &= P_2(x,y) * H(x,y) \\ &= B \cdot \sin 2\pi [W(x,y) - W_R(x,y)] \quad . \end{aligned} \tag{3.5}$$

$W(x,y)$ is then computed from the ratio of the two moiré functions as follows,

$$W(x,y) = W_R(x,y) + (1/2\pi) \cdot \arctan[M_2(x,y)/M_1(x,y)] \quad . \tag{3.6}$$

Since the convolution window must be several fringe periods wide, a high fringe density is needed in order for each phase measurement to be localized to a region much smaller than the overall width of the pupil. This also keeps the loss of phase information where the convolution window overlaps the edge of the pupil small.

Closed Fringe Patterns

The Fourier transform of the product I(x,y)·R(x,y) consists of lobes whose widths are approximately equal to the range of slopes associated with the sum, difference, and reference terms. For closed fringe patterns these spectral lobes overlap one another and the difference component of the spectrum cannot be perfectly isolated. Portions of the sum and reference lobes which lie near-dc are passed along with the difference component by a low-pass filter as illustrated in Figure 23. This does not however degrade phase measurement across the entire pupil. In fact, the only degradation occurs in the spatial zone of the pupil which contributes near-dc frequency components to the sum and reference lobes of the Fourier transform of Eq. (3.3). For closed fringe patterns this zone corresponds approximately to the region surrounded by the central fringe. For other spatial zones of the pupil, the sum and reference spectral contributions are well-displaced from the difference component and as a result the separation of terms by low-pass filtering is excellent for those areas of the fringe pattern.

The moiré between two sheared zone plates as shown in Figure 24 provides a good visual demonstration. One zone plate can be regarded as a test pattern and the other a reference. Since this reference corresponds to an irradiance distribution a dc component is present which is of no consequence here. Over most of the pupil it is observed that the surface deviation is coded on a high spatial frequdncy carrier such that multiplication by a well-matched reference followed by low pass filtering

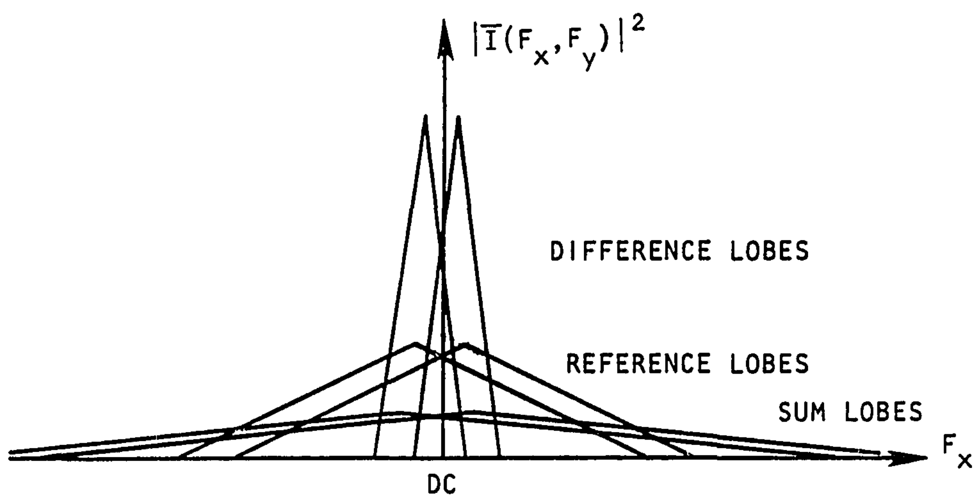


Figure 23. Fourier spectra for product of test and reference patterns containing closed fringes.

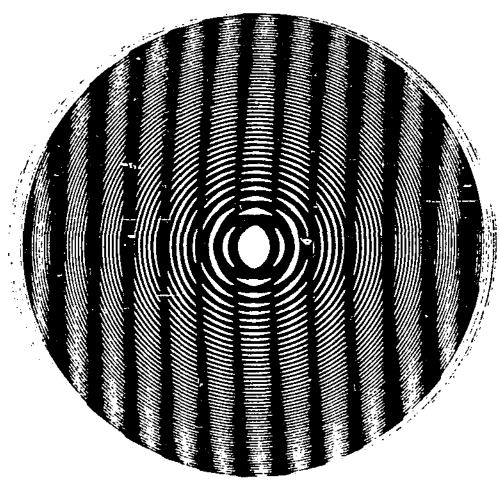

Figure 24. Moiré between two sheared zone plates.

produces a high visibility moiré. Only in the vicinity of the central fringe is there any disturbance to the moiré.

In conclusion, phase measurements on closed fringe patterns using QMM can be made over a large portion of the pupil with no error due to overlapping spectral lobes assuming a high fringe density and a well-matched reference pattern. Under these circumstances error due to overlapping spectra is restricted to the low spatial frequency zone of the unknown fringe pattern.

## Biased Fringe Patterns

The overlap of spectral lobes associated with the sum, difference, and reference components of the product of test and reference patterns can be eliminated if a high spatial frequency carrier is added to each surface. In this case the function $W(x,y)$ in Eq. (3.1) can be written

$$W(x,y) = F_o x + W'(x,y) \quad , \tag{3.7}$$

where the carrier is assumed to be a planar surface tilted in the x-direction. If harmonics are present then the condition

$$F_o > 3 \left. \frac{\partial W'(x,y)}{\partial x} \right|_{max} \tag{3.8}$$

must be met in order to separate 1st and 2nd order lobes as illustrated in Figure 25a since the width of the 2nd order lobe is twice that of the 1st order. Likewise the biased reference of Eq. (3.2) can be written

$$W_R(x,y) = F_R x + W_R'(x,y) \quad , \tag{3.9}$$

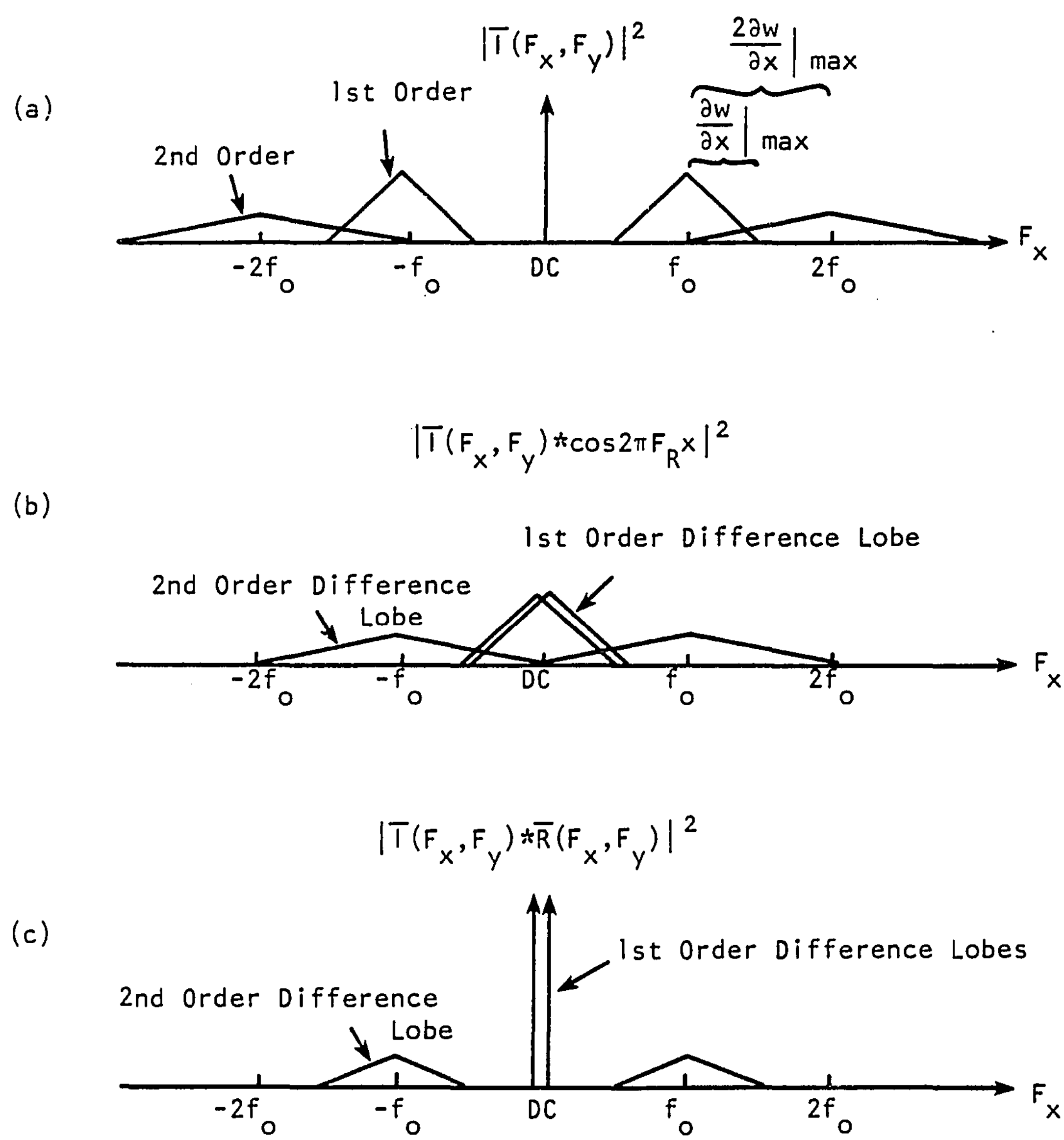


Figure 25. Fourier spectra.

(a) Biased test pattern with 1st and 2nd order sidelobes shown.
(b) Difference lobes for product of test and one-dimensional sinusoidal reference.
(c) Difference lobes for product of test and well-matched reference.

where again the carrier $F_R$ is taken to be a plane tilted in the x-direction.

The difference terms associated with the first and second harmonics have arguments given by

$$W(x,y) - W_R(x,y) = (F_o - F_R)\cdot x + W'(x,y) - W_R'(x,y) \tag{3.10}$$

and

$$2W(x,y) - W_R(x,y) = (2F_o - F_R)\cdot x + 2W'(x,y) - W_R'(x,y) \ . \tag{3.11}$$

If $F_o \approx F_R$ and $W_R'(x,y) = 0$, i.e., the reference is pure tilt, the 1st and 2nd order lobes are shifted down by $F_R$ in spatial frequency with their shapes unchanged as shown in Figure 25b. The condition stated in Eq. (3.8) then must be met in order that low-pass filtering can isolate the low spatial frequency moiré due to the 1st order difference term.

On the other hand, if $F_o \approx F_R$ and $W_R'(x,y)$ is not planar, then not only are the first order side lobes shifted down in frequency due to the difference term but their energy is redistributed. For example, if $W'(x,y)$ and $W_R'(x,y)$ are perfectly matched the difference term associated with the first order lobes condenses to a single delta function located at DC. For the zone plate example of Figure 24 the first order difference lobes condensed to two delta functions near DC due to shear between the patterns.

For the case of well-matched reference and test patterns the 2nd order difference lobe reduces to the original width of the 1st order as illustrated in Figure 25c. The condition for isolation of the low spatial frequency component is then given approximately by

$$F_o > \left.\frac{\partial W'(x,y)}{\partial x}\right|_{max} , \qquad (3.12)$$

which is much less severe than the earlier condition where the reference was regarded as planar.

In conclusion, biased fringe patterns permit phase measurements with near perfect isolation of the low spatial frequency quadrature moiré functions provided certain conditions are met for the relative sizes of the carrier frequency and the maximum surface slope. Figure 26 illustrates quadrature moiré functions obtained from a biased fringe pattern by shifting the reference approximately one-quarter period. It is observed that the moiré changes in the same manner as would be expected for a live fringe pattern if the PZT on the reference arm of an interferometer were incremented by one-eighth a wavelength.

## Convolution Window

The moiré value at a point $x_o,y_o$ within the pupil is given by the integral

$$M(x_o,y_o) = \int_{-\infty}^{\infty} I(x,y)\cdot R(x,y)\ h(x_o-x,y_o-y)dxdy . \qquad (3.13)$$

Assume the fringe density is high and that the major contributions to the integral come from the immediate vicinity of $x_o,y_o$. $W(x,y)$ and $W_R(x,y)$ can be represented by a Taylor series expansion about the point $x_o,y_o$ as follows,

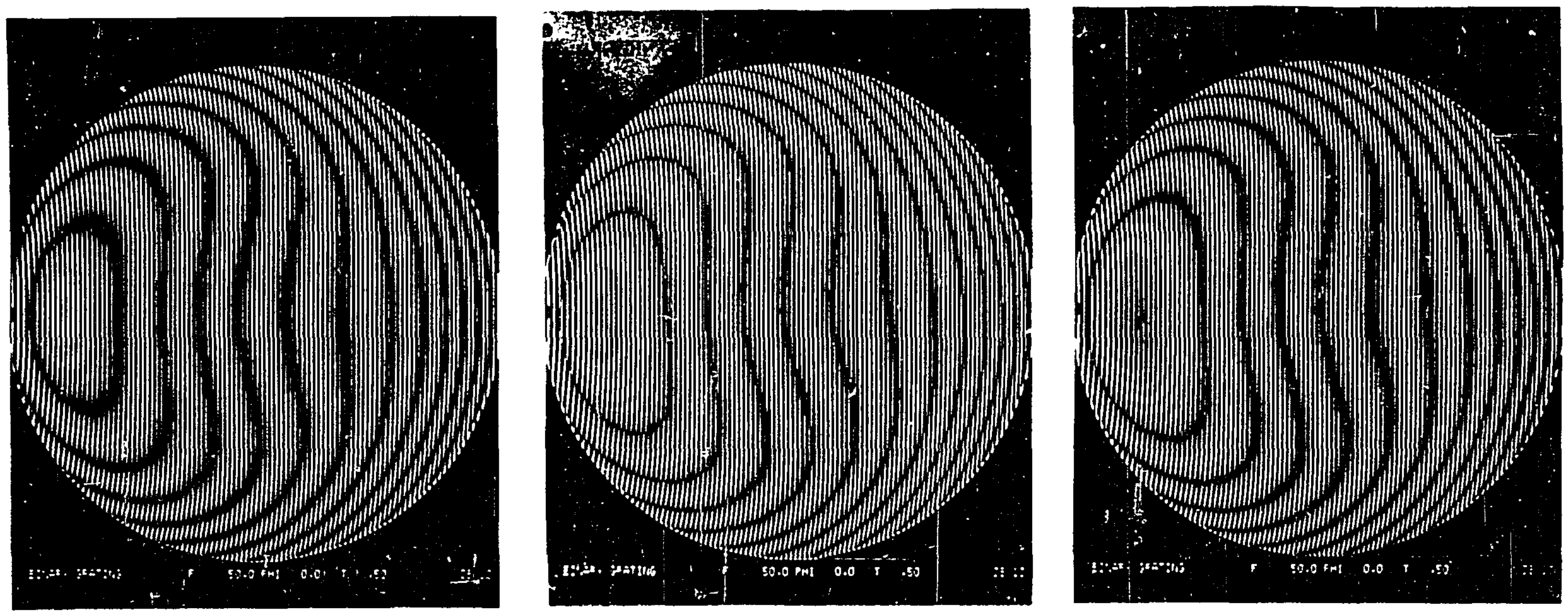

Figure 26. Moiré produced by successive shifts of a one-dimensional reference pattern.

$$W(x,y) = W(x_o,y_o) + \left.\frac{\partial W(x,y)}{\partial x}\right|_{x_o,y_o} \cdot (x-x_o)$$

$$+ \left.\frac{\partial W(x,y)}{\partial y}\right|_{x_o,y_o} \cdot (y-y_o)$$

$$W_R(x,y) = W_R(x_o,y_o) + \left.\frac{\partial W_R(x,y)}{\partial x}\right|_{x_o,y_o} \cdot (x-x_o)$$

$$+ \left.\frac{\partial W_R(x,y)}{\partial y}\right|_{x_o,y_o} \cdot (y-y_o) \quad , \tag{3.14}$$

where terms beyond the first order are neglected. The slopes in these equations represent the local spatial frequencies of the two fringe patterns while the dc terms set the local relative phase shifts of the patterns. Therefore $I(x,y) \cdot R(x,y)$ may be represented approximately by the product of two straight fringe patterns in the neighborhood of $x_o,y_o$. In this point-of-view the spectral lobes associated with the sum, difference, and reference terms are regarded as composed of contributions from local neighborhoods across the entire fringe pattern. The spectral contributions from a particular neighborhood are located at $\pm(\underset{\sim}{F_o}-\underset{\sim}{F_R})$, $\pm(\underset{\sim}{F_o}+\underset{\sim}{F_R})$, and $\pm\underset{\sim}{F_R}$ where $\underset{\sim}{F_o}$ and $\underset{\sim}{F_R}$ are vectors described by

$$\underset{\sim}{F_o} = \left( \left.\frac{\partial W(x,y)}{\partial x}\right|_{x_o,y_o} , \left.\frac{\partial W(x,y)}{\partial y}\right|_{x_o,y_o} \right) \cdot$$

$$\underset{\sim}{F_R} = \left( \left.\frac{\partial W_R(x,y)}{\partial x}\right|_{x_o,y_o} , \left.\frac{\partial W_R(x,y)}{\partial y}\right|_{x_o,y_o} \right) \cdot \tag{3.15}$$

Ideally the transfer function associated with the convolution window passes the difference frequency component unattenuated and completely eliminates the higher frequency components. In practice, the transfer function is not perfect and the higher frequency components can be regarded as noise sources which, in combination with other possible sources of noise, degrade the moiré measurement.

The one-dimensional windows and transfer functions presented in Figure 27 show the relative performances of a Hamming and simple rect windows. The latter provides an attenuation of only -13 db at the peak of the first sidelobe. The Hamming window or, for that matter, any of several other windows used in digital signal processing provides an attenuation of -40 db (factor of 100) at the peak of the first sidelobe. Visualization of components at $\pm(F_o - F_R)$, $\pm(F_o + F_R)$, and $\pm F_R$ superimposed upon the transfer function provides valuable insight into the performance of quadrature moiré phase measurement. The moiré amplitude and therefore the signal-to-noise ratio are maximum when $F_o = F_R$ and falls off as $F_o$ deviates from $F_R$. In terms of visual moiré the low spatial frequency fringes suffer a loss in contrast as the periods of the unknown and reference patterns deviate from one another.

## One-Dimensional Reference

For practical implementation of QMM phase measurement a one-dimensional reference pattern is attractive. Ichioka and Inuiya (1972) took this approach in an analog system in which quadrature signals derived from a reference oscillator were multiplied times a video signal

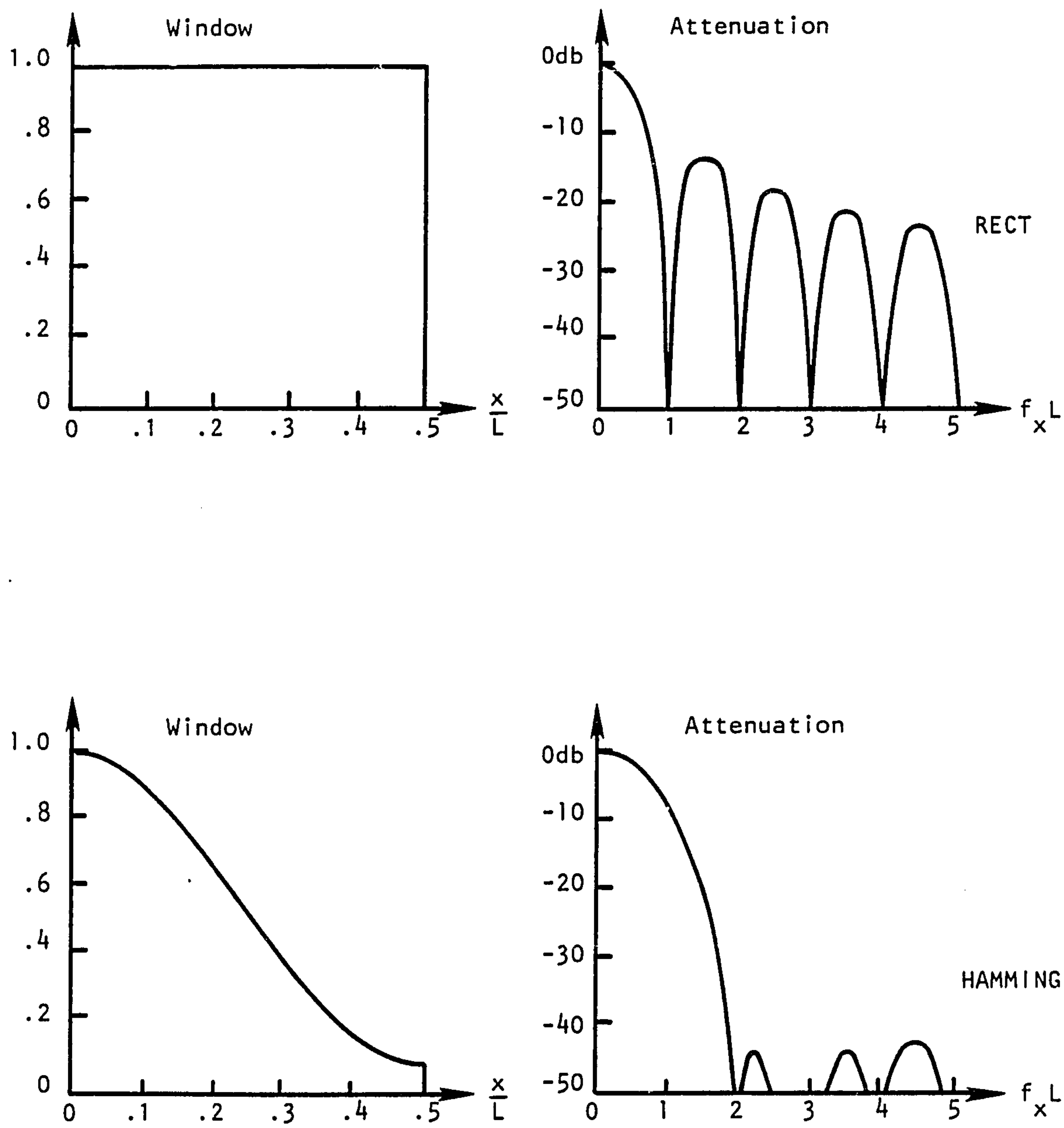


Figure 27. Window and transfer functions.

in real-time. The temporal product was low-pass filtered and the phase output of an analog arctangent circuit was displayed on a monitor.

A digital approach using microcomputer technology provides greater flexibility than the analog scheme and is better-suited to obtaining quantitative phase measurements. In applying a microcomputer to QMM phase measurement the advantage of a one-dimensional reference is that the quadrature signals need only be calculated once and stored in memory for later multiplication times each digitized line of the fringe pattern. The less efficient alternatives are to re-calculate the reference as needed or to make use of quadrature reference images stored on disk. With a computer the reference period and window function can be manipulated under software control.

The use of digital techniques implies that the fringe pattern signal will no longer treated as continuous. The two moiré functions described earlier can be rewritten in discretized form as follows,

$$M_1(x_o,y_o) = \sum_{i=-M}^{+M} I(x_i,y_i)\cos 2\pi F_R x_i \; h(x_o-x_i,y_o-y_i)$$

M is even

$$M_2(x_o,y_o) = \sum_{i=-M}^{+M} I(x_i,y_i)\sin 2\pi F_R x_i \; h(x_o-x_i,y_o-y_i) \tag{3.16}$$

These equations are recognized as the spatial equivalent of digital synchronous detection. From this point-of-view phase measurement by QMM is much the same as having an array of spatial lock-in amplifiers distributed across the fringe pattern image. A by-product of discretizing the moiré integrals is that the spectrum associated with the product of fringe patterns and the window is repeated in the frequency domain at an interval equal to the reciprocal of the sample spacing. It is desirable to have enough samples per fringe period to eliminate aliasing due to harmonics of the fringe pattern.

Bruning et al. (1974) have discussed the effect of additive Gaussian noise upon the phase error associated with temporal synchronous detection. They show that in the limit of zero signal-to-noise all phase values are equally likely. For large signal-to-noise ($S/N \gg 1$) the phase error is given approximately by the expression,

$$\Delta\phi = 1/(\sqrt{M} \cdot S/N), \tag{3.17}$$

where M is the number of discrete steps. This result is directly applicable to QMM measurement. Eqs. (3.16) are also recognized as equivalent to the real and imaginary parts of one coefficient of a windowed DFT. Jain (1978) and Walkup and Goodman (1973) have discussed phase measurement on a one-dimensional, single frequency sinusoidal signal by computing a single DFT coefficient. The latter shows by a joint-maximum-likelihood argument that a DFT phase estimator is near-optimal.

Simulation

To study the characteristics of QMM phase measurement a simulation was performed in which an interferogram was represented by the expression below

$$I(x,y) = [1+\cos 2\pi\left(W_o(x^2+y^2)+f_o x\right)] \cdot e^{-\frac{x^2+y^2}{\sigma^2}} + n(x,y) \ , \tag{3.18}$$

where I(x,y) was quantized to N bits, $W_o$ was the amount of defocus, $\sigma$ was the width parameter for the Gaussian envelope, and n(x,y) was additive Gaussian noise. Defocus was selected for performance tests because its wavefront slope is linear in the x and y directions making it easy to observe the effect of slope on results. For all runs I(x,y) was computed over a 128 x 128 array of pixels with $F_o$ and $W_o$ fixed at 20 waves/radius and 10 waves, respectively. The amount of aberration was deliberately chosen large compared to the tilt in order that the degradation in phase measurements which occurs when the difference component is strongly attenuated by the transfer function would be clearly observed. A one-dimensional reference was used with $F_o = F_R$. The pupil radius was set at 60 pixels. The size of the integration window was 3 x 9 pixels with weighting by a Hamming function.

Figure 28 illustrates the result of a typical run. A zone of precise phase measurements (less than 0.02 waves error) was observed oriented vertically across the center of the pupil. Within this zone the fringe and reference periods in the x-direction are sufficiently well-matched that the difference frequency spectral components for each local neighborhood lie within the central lobe of the filter transfer function. Outside this zone the difference frequency components are strongly attenuated yielding poor signal-to-noise and inaccurate phase measurements. In terms of visual moiré this degradation in signal-to-noise corresponds to the low spatial frequency moiré period decreasing such that convolution with a window of fixed width yields a reduced visibility.

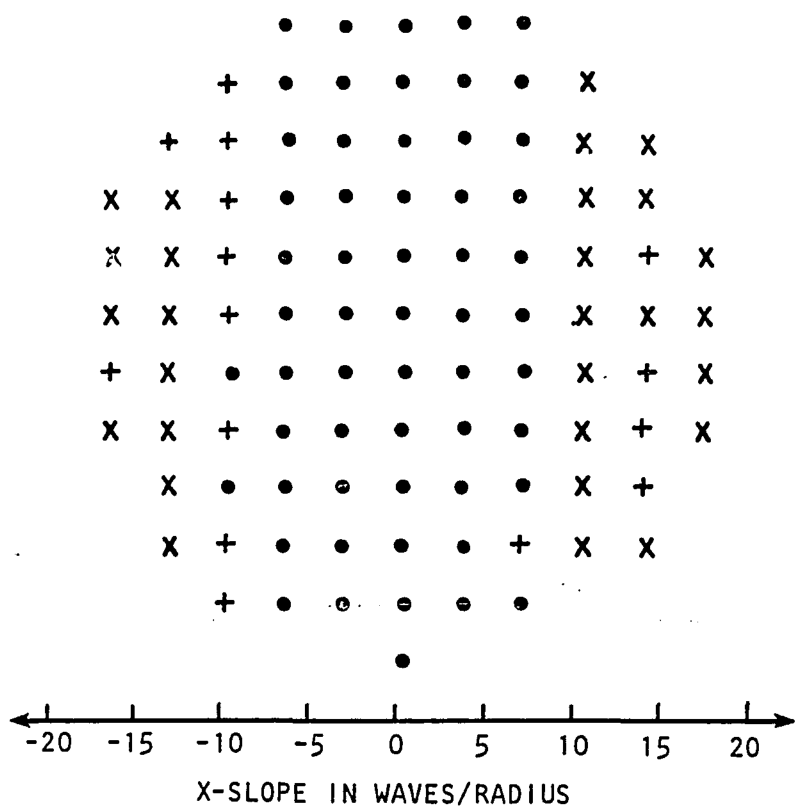


Figure 28. Difference between actual and measured phase for interferogram containing 40 fringes across the pupil with 10 waves of defocus.

Sample array was 128x128x6 bits with a 3x9 pixel integration window.

● < .02 waves

+ .02 to .10 waves

X > .10 waves

Table 2 summarizes performance as a function of Gaussian noise, the number of quantization levels, and the envelope width parameter. All rms values refer to the central measurement zone described above. The results indicate that good performance can be achieved for a variety of system configurations and conditions. Since the phase error is proportional to the reciprocal of the square root of the number of samples, the error will improve if sampling resolution or window dimensions are increased assuming all other parameters are held constant. Increased resolution also permits operation at greater tilt angles thereby extending the range of wavefront slope over which accurate phase measurements are obtained.

## A QMM Video System

### System Description

An image processing system was assembled to demonstrate QMM phase measurement on fringe pattern photographs. The system consisted of a 4 MHz Z-80 microcomputer with 64K RAM, dual 8-inch disk drives, a 4 MHz 9511 arithmetic unit, and a custom-designed video interface. The latter was a column digitizer based upon the TRW 6 bit A-to-D and a control circuit for addressing 960 x 480 pixels. To process photographs an RCA TC 2000 CCTV camera with 6:1 zoom lens was mounted vertically on an adjustable-height stand.

FORTH was found to be well-suited for implementing a special purpose image processing system. The language is highly interactive and

Table 2. Results of computer simulation at 128x128xN bits with 40 fringes across the pupil and 10 waves of defocus.

Quantization Noise. No Gaussian Noise added to image.

| Number of Bits | RMS Error in Waves |
|---|---|
| 6 | .010 |
| 4 | .013 |

Gaussian Noise. Quantized to 6 bits.

| RMS Signal-to-Noise Ratio | RMS Error in Waves |
|---|---|
| 28 | .013 |
| 14 | .020 |
| 7 | .059 |
| 3.5 | .083 |

Nonuniform Envelope. Quantized to 6 bits and no Gaussian Noise.

| Center-to-Edge Attenuation Ratio | RMS Error in Waves |
|---|---|
| 2.7 | .016 |
| 7.7 | .05 |

encourages modular programming. With FORTH the programmer literally designs an instruction set appropriate to each piece of hardware. In addition the programmer can work at the level of assembly language where speed is critical and with higher-level commands where convenience is more important than speed. For example, in this application the evaluation of the two quadrature moiré expressions was performed in assembly language using the internal stack and commands of the 9511 arithmetic processor. Other functions such as generating graphics output and computing P-V and rms were accomplished through a pyramid-like structure of higher level commands.

### Video Interface

The circuit schematic for the video column digitizer is presented in Figure 29. An 8224 clock driver and crystal were used to generate an 18.432 MHz dot clock. The 8224 also provided a 2.048 MHz clock to a 5321 TV sync generator. Vertical and horizontal sync outputs from the 5321 were buffered and inverted to meet the external sync requirements of the RCA CCTV camera. The 18.432 MHz clock was input to a set of 74161 synchronous binary counters whose outputs were connected to one of the two sets of inputs of an 8130 10 bit comparator. A second 10 bit word was input to the comparator from an 8255 PPI. In this way a 55 nsec pulse was obtained from the 8130 whose position in time corresponded to the horizontal pixel location addressed by the 8255. An additional pair of 74161 counters are clocked by the composite blanking output of the 5321 sync generator. The 8255 PPI and this second set of counters serve as inputs

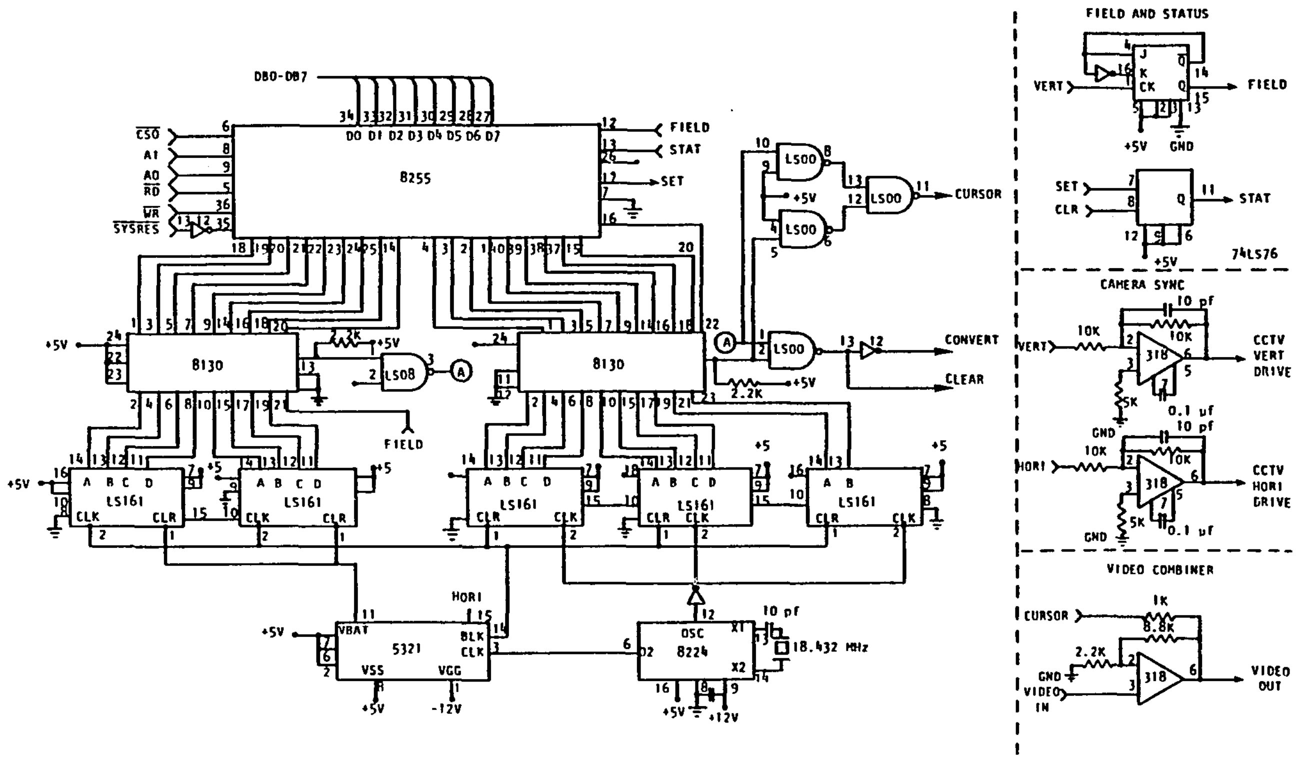


Figure 29. Video column digitizer.

to a second 8130 10 bit comparator. This comparator's output goes low for the duration of the video line addressed by the 8255. The two comparator outputs are combined by an AND gate to obtain a convert pulse for the TRW 6 bit A-to-D and are logically OR'ed to obtain the signal needed to produce a visual cross-hair superimposed on the camera video. The 6 bit data from the TRW A-to-D is transferred to the Z-80 via a 74LS244 tri-state buffer. Not shown in the schematic of Figure 29 are bus buffers, a chip select decoder, and the support circuit for the A-to-D.

Operation

The first step in reducing a fringe pattern by QMM is to digitize an image. A photograph is placed on the photo-easel, zoom is adjusted, and the image is centered with respect to a square area displayed on the screen. This area contains 256 x 384 pixels. By restricting measurements to the central portion of the vidicon raster distortion error in sample positions is reduced. The system asks for the number of scans to be summed. Digitization then proceeds column by column from left to right across the image with a single scan requiring approximately 10 seconds. The signal-to-noise improvement due to summing successive scans is proportional to the square root of the number of scans. This is important in this application since high fringe densities result in a video signal that is strongly attenuated by the combined MTF's of the camera and lens. Typically with 50 high visibility fringes across the image 4 to 12 scans are needed to boost the signal-to-noise to the range of 10 to 20.

Next a selected video line is examined using graphics displayed on the CRT terminal screen and the approximate fringe period is noted. The operator then responds to a system query asking for a reference period and window width. The direct phase measurement including modulo-pi transitions due to the arctangent in Eq. (3.6) is immediately displayed on the CRT. The direct phase measurement is clearly noisy for a poor choice of reference and window. The operator, at this point, has the option of making new choices for the reference and window parameters. The specification of reference and window can be completely automatic but for maximum flexibility the choices were left to the operator in this system. Options are selected giving the size of the measurement array and specifying the terms of a least squares fit which should be subtracted from the phase values. The analysis and print-out then proceed with no further operator intervention yielding results such as those shown in Figures 30 to 32. The first of these analyses presents phase measurements obtained over a 64 x 128 array for a straight line fringe pattern projected onto a human back. Time required for this analysis excluding the print-out was approximately 20 minutes. A phase profile obtained in testing an optical fiber preform is shown in Figure 32. A plot proportional to the moiré amplitude given by the square root of the sum of the squares of the two quadrature moiré values was provided in this analysis. The amplitude of moiré fringes is useful to the operator since it indicates the approximate signal-to-noise for the phase measurements. Profiles such as those shown in Figures 31 and 32 require less than 5 minutes to complete including the digitization.

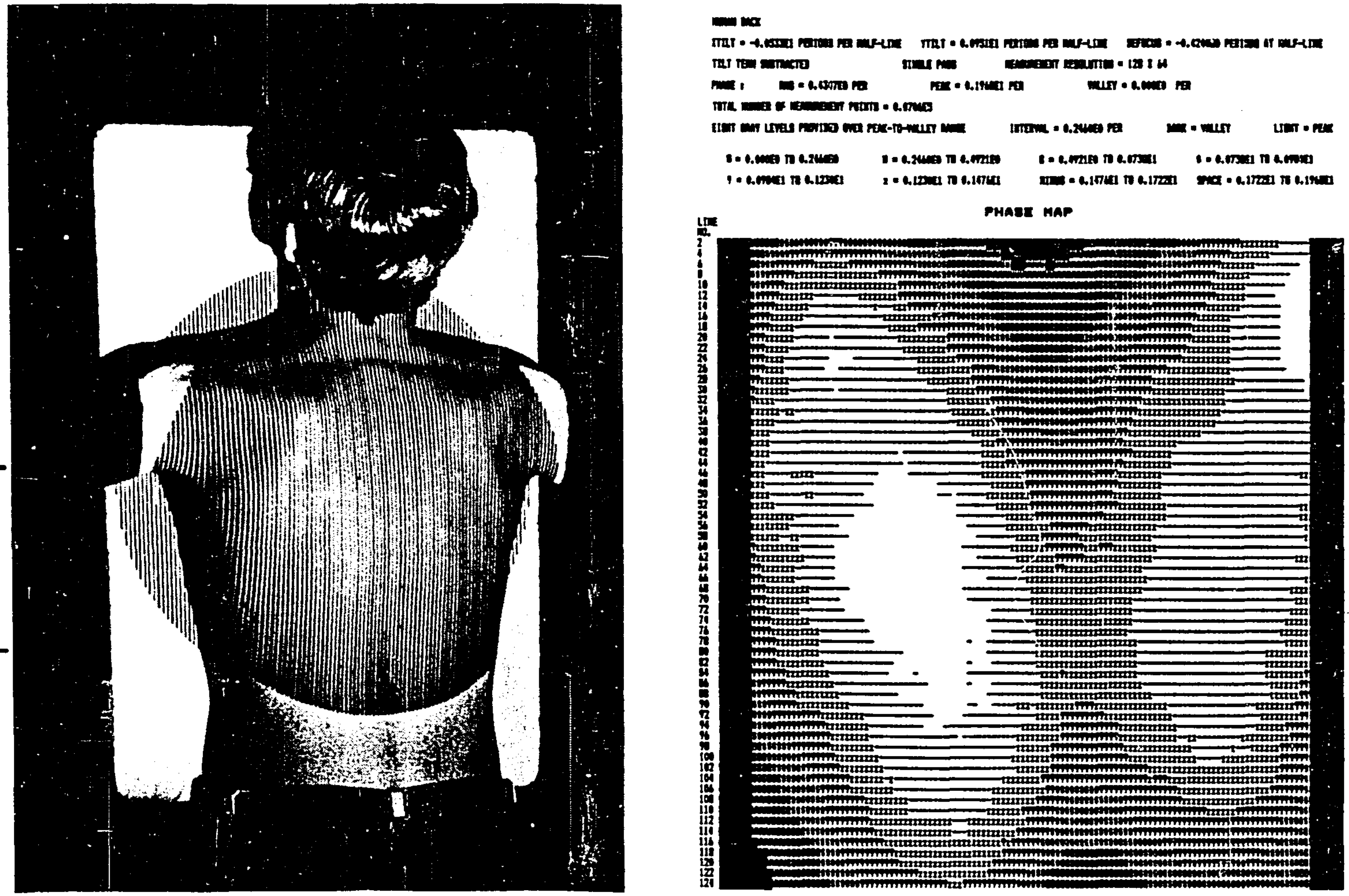


Figure 30. Parallax map of human back.

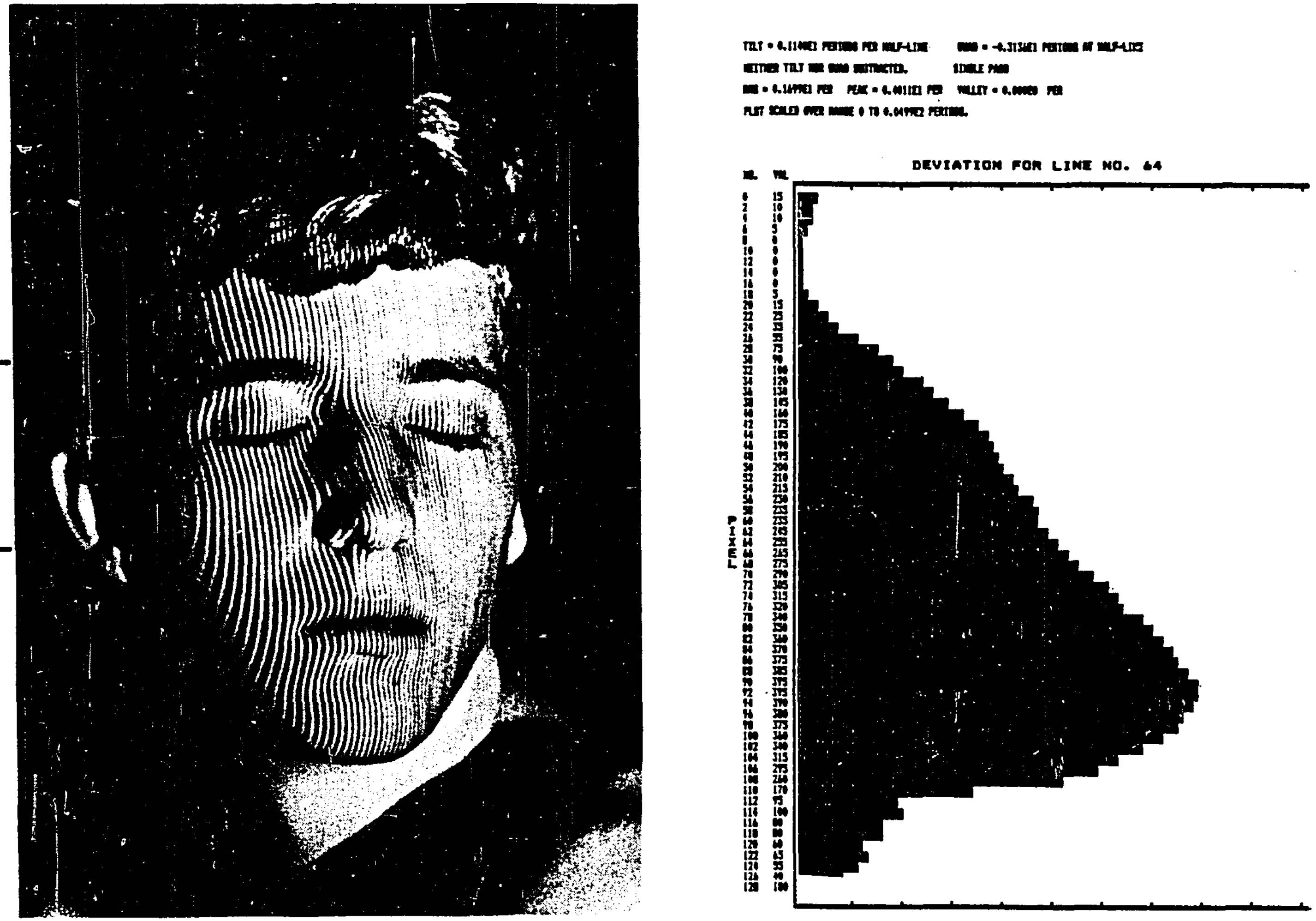


Figure 31. Parallax profile obtained from forward view of face.

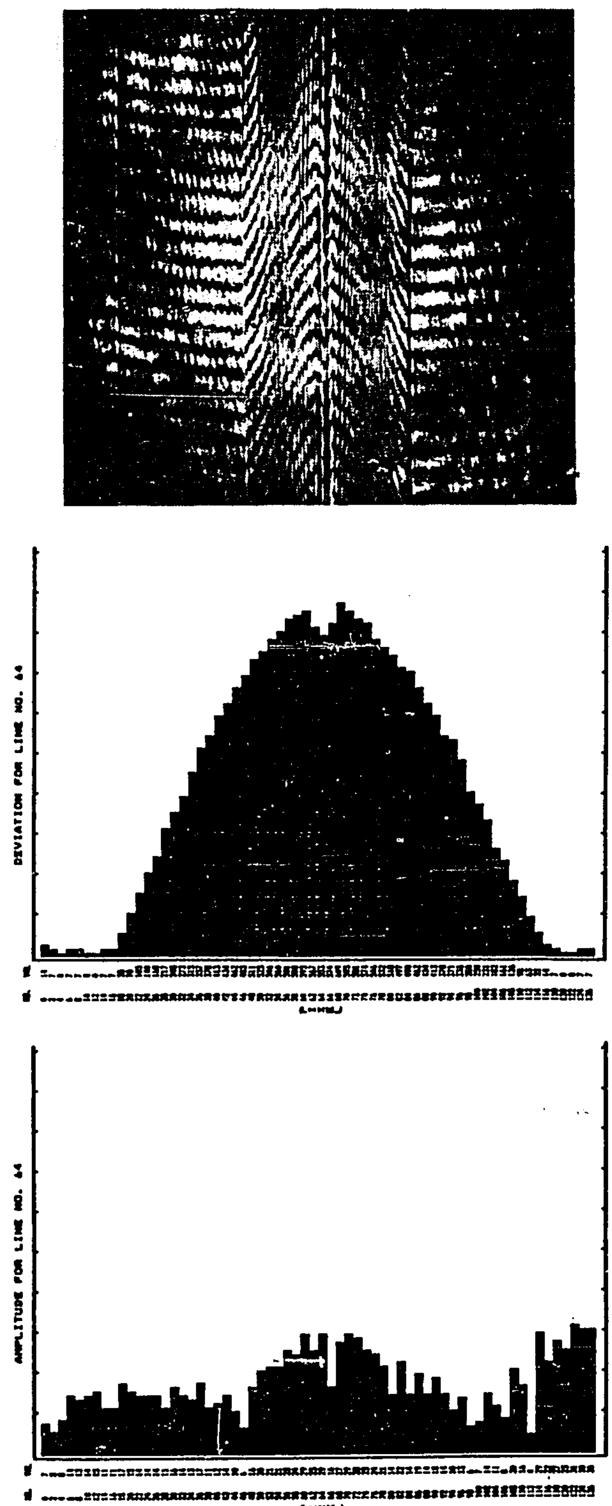


Figure 32. Phase and amplitude profiles obtained in testing an optical preform.

## Special Applications

### Smartt Point Interferometer

For the Smartt point interferometer it is not possible to introduce tilt in order to obtain the high fringe density needed for QMM phase measurement. This is due to the design of the interferometer which consists of a transmissive disk containing a small aperture generally chosen to be a fraction of an Airy disk in diameter. This aperture generates a reference by diffraction which interferes with the test wavefront producing fringes equivalent to those obtained with a Twyman-Green interferometer. To introduce tilt the aperture must be laterally shifted but, unfortunately, a reduction of fringe contrast occurs as the reference aperture moves away from the focal spot of the test beam. It is easy, however, to obtain a high fringe density with good contrast by introducing defocus as this requires longitudinal motion of the aperture along the beam axis. The logical choice of a reference pattern for QMM phase measurement is a sinusoidal zone plate. If no aberration is present on the test beam then the moiré of the reference and fringe pattern consists of straight low-spatial frequency fringes as illustrated in Figure 24. Quadrature references are used to obtain the two moiré needed for phase measurement. As explained earlier some error can be expected in the neighborhood of the central fringe. Otherwise, the accuracy of phase measurements should be as good as would be expected for a biased fringe pattern. An alternative method for obtaining a phase error proportional to the reciprocal of the signal-to-noise is to shift actively the frequency or phase of the reference or test beams. Due to the design of the Smartt point interferometer, this is difficult to accomplish making QMM phase measurement particularly attractive for this application.

Photogrammetry

The height of a diffuse surface can be measured by projecting a fringe pattern onto the surface while viewing it at an angle with respect to the optical axis of the projector. The geometry of the set-up must be known and the parallax of the curved fringes in the surface image must be measured. Parallax is defined to be the displacement of the image of a fringe from its position for a normal range of infinity. Parallax increases with decreasing distance to the surface.

Perrin and Thomas (1977) have noted that the connection between parallax and surface height is particularly simple for the geometry shown in Figure 33. Pirodda (1977) has considered a more general arrangement of the projector, camera, and diffuse surface. From similar triangles in Figure 33 (Castleman, 1979) the image of a reference line occurs in the film plane at

$$x_I = \frac{Sx}{z} , \tag{3.19}$$

while the position of the line in the projector's reference plane is given by

$$x_R = \frac{S(x-d)}{z} . \tag{3.20}$$

Eliminating x from these two equations the normal range is given by

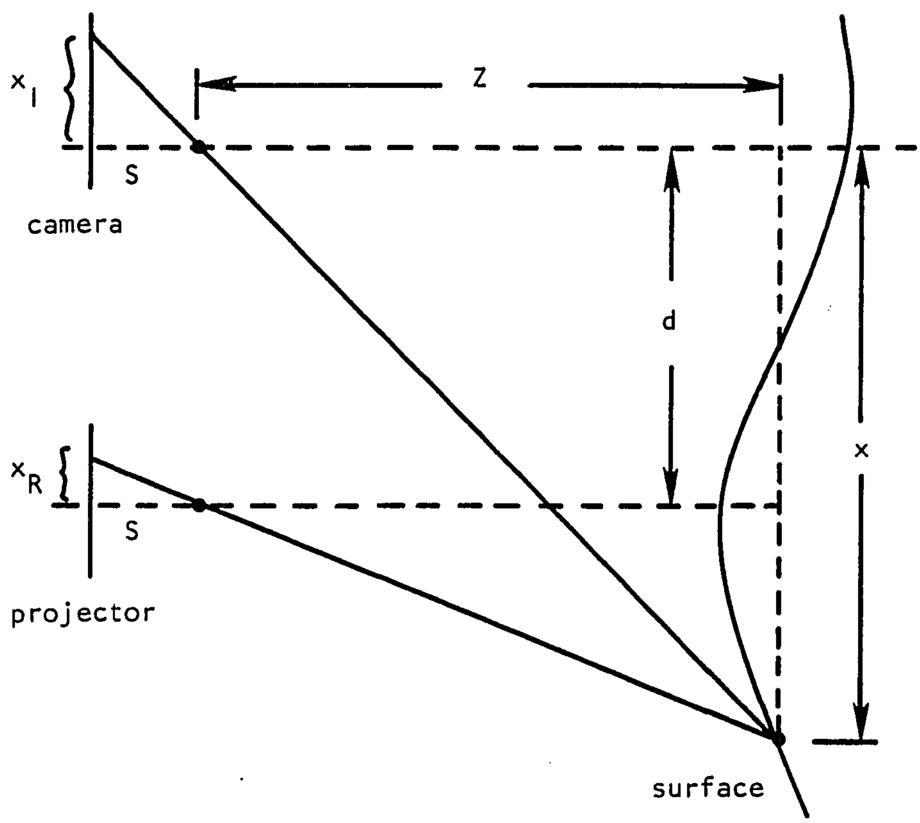


Figure 33. Simple geometry for parallax measurement.

$$Z = \frac{sd}{x_I - x_R} = \frac{sd}{KP} \quad , \tag{3.21}$$

where $x_I - x_R$ is the parallax and KP is the parallax expressed in reference periods. It is concluded that planes of constant parallax lie perpendicular to the optical axes and that the distance between the K=N and K=N+1 planes increases hyperbolically with increasing range. The image of the fringe pattern at the film plane can be written

$$\begin{aligned} I(x,y) &= A + B \cdot \cos 2\pi F_x \left[x + \frac{sd}{Z}\right] \\ &= A + B \cdot \cos 2\pi F_x [x + KP] \quad . \end{aligned} \tag{3.22}$$

Assuming that a one-dimensional reference is used for QMM phase measurement, the low spatial frequency moiré fringes derived from this image can be regarded as contours of equal parallax.

If the change in surface height is small compared with the normal range then from a Taylor series expansion of Eq. (3.21) the parallax and range are linearly related by the expression

$$x_I - x_R \simeq \frac{sd}{Z_o} - \left(\frac{sd}{Z_o}\right) \cdot \left(\frac{Z - Z_o}{Z_o}\right) \quad . \tag{3.23}$$

Expressing the parallax in units of the reference period, the measurement sensitivity is obtained as follows,

$$\frac{\Delta(x_I - x_R)}{P} \approx \left(\frac{sd}{Z_o}\right)\left(\frac{1}{P}\right)\left(\frac{\Delta Z}{Z_o}\right) \tag{3.24}$$

or

$$\Delta Z \approx \left(\frac{Z_o}{s}\right)\left(\frac{Z_o}{d}\right)\left(\frac{\Delta(x_I - x_R)}{P}\right) P \tag{3.25}$$

$\Delta Z \approx$ (Magnification)$\cdot$(Perspective)$\cdot$(Change in Parallax)

$\cdot$ P in Periods.

If the smallest change in parallax that can be measured is 1/100 of a reference period, and assuming a magnification of 25 and perspective of 10, the limiting sensitivity of surface height measurement is just

$$\Delta Z \approx (25)(10)\left(\frac{1}{100}\right) P = 2.5\ P \quad . \tag{3.26}$$

Two examples of parallax measurement using projected fringes are presented in Figures 30 and 31.

## Alternative Synchronous Convolution Techniques

Sinusoidal Window

If a biased fringe pattern is high-passed filtered the resulting high spatial frequency function can be written

$$F_1(x_o,y_o) = \int_{-\infty}^{\infty} I(x,y)h(x_o-x,y_o-y)dxdy$$

$$= \int_{-\infty}^{\infty} I(x,y)\cos 2\pi f_R(x_o-x)h'(x_o-x,y_o-y)dxdy \ . \tag{3.27}$$

Comparing this equation with the quadrature moiré integral, it is noted that for high-pass filtering the cosine reference is shifted with the window rather than maintaining a fixed phase with respect to I(x,y). A second convolution can be evaluated using a filter in quadrature with the first as follows,

$$F_2(x_o,y_o) = \int_{-\infty}^{\infty} I(x,y)\sin 2\pi f_R(x_o-x)h'(x_o-x,y_o-y)dxdy \ . \qquad (3.28)$$

Phase is computed from the expression

$$W(x_o,y_o) = \frac{1}{2\pi} \arctan\left[\frac{F_2(x_o,y_o)}{F_1(x_o,y_o)}\right] \ . \qquad (3.29)$$

Complex Exponential Window

A biased fringe pattern containing a dc term and ±1 order sidelobes can be written

$$\begin{aligned} I(x,y) &= A + B\cdot\cos 2\pi W(x,y) \\ &= A + (B/2)\cdot\exp[i2\pi W(x,y)] + (B/2)\cdot\exp[-i2\pi W(x,y)] \ . \end{aligned} \qquad (3.30)$$

The quadrature moiré and sinusoidal window techniques utilize both sidelobes for phase measurements. Nevertheless the desired phase information is present in a single sidelobe. A convolution window which passes a single sidelobe can be defined as follows,

$$\begin{aligned} h'(x,y) &= h(x,y)\cdot\exp\ i2\pi F_R x \\ &= h(x,y)\cdot[\cos 2\pi F_R x + i\cdot\sin 2\pi F_R x] \ . \end{aligned} \qquad (3.31)$$

The real and imaginary parts of the function resulting from this convolution are identical to $F_1(x,y)$ and $F_2(x,y)$ described for the sinusoidal window method. Since the complex representation of the sidelobe is $\exp[i2\pi W(x,y)]$, phase is given by the arctangent of the real and imaginary parts.

In conclusion, if the convolutions are performed directly in the spatial domain, the computations performed for both the sinusoidal window and complex exponential method are identical for each phase measurement. The frequency domain pictures for the two methods are, however, distinctly different. One passes a double sidelobe and the other a single sidelobe. If the convolution is computed via the DFT convolution theorem, the difference between the two techniques is profound. By this theorem the convolution of two spatial domain discrete functions is equal to the inverse transform of the product of their DFT's. With this understanding the complex exponential window method can be implemented as follows:

(1) Take the DFT of a single line across the biased fringe pattern.

(2) Locate the peak of the first sidelobe and multiply the DFT by a rect or other transfer function centered at the sidelobe.

(3) Compute the inverse DFT of the product.

(4) Obtain phase by taking the arctangent of the ratio of real and imaginary parts at each spatial point.

Stockham (1966) has pointed out the time savings that can result when convolutions are evaluated by using the fast Fourier transform algorithm with the DFT convolution theorem. If the convolution of two real functions of lengths N and L is performed directly, the total time required is given approximately by the expression

$$T_D \approx K_A N(L-1)+K_m NL \quad , \tag{3.32}$$

where $K_A$ and $K_m$ are the times associated with multiplication and addition, respectively. The region where the window of length L overlaps the edge of the array of length N is neglected here. Computation of the FFT of a function of length N requires $N\log_2 N$ complex multiplications and $N\log_2 N$ complex additions. In terms of real arithmetic operations, the total time to evaluate a convolution using FFT's is given approximately by the expression

$$T_F \approx (10 \cdot K_A + 8 \cdot K_m)\ N\log_2 N + K_m L \quad , \tag{3.33}$$

where it is assumed that the transfer function of the convolution window is known and is nonzero over L points in the frequency domain. Table 3 presents the ratios of execution times based on Eqs. (3.32) and (3.33). Note that if the window is sufficiently short compared to the length of the array with which it is being convolved then the direct convolution is faster than evaluation using FFT's. As the window length increases a point is reached where both methods require the same amount of time and for larger window lengths the FFT method is faster than direct computation.

Comparison

The phase obtained for all three techniques contains modulo-pi transitions which must be removed before performing a fit or computing

Table 3. Relative performance for evaluating the convolution directly and by using FFT's.

| | | | Ratio of Times* (FFT/Direct) | | |
|---|---|---|---|---|---|
| N | $N^2$ | $N\log_2 N$ | $L = \frac{N}{20}$ | $L = \frac{N}{10}$ | $L = \frac{N}{5}$ |
| 128 | 16384 | 896 | 10.94 | 5.47 | 2.74 |
| 256 | 65536 | 2048 | 6.24 | 3.12 | 1.56 |
| 512 | 262144 | 4608 | 3.52 | 1.76 | 0.88 |
| 1024 | 1048576 | 10240 | 1.96 | 0.98 | 0.49 |
| 2048 | 4194304 | 22528 | 1.08 | 0.54 | 0.27 |
| 4096 | 16777216 | 49152 | 0.58 | 0.29 | 0.15 |

$$* \; T_F/T_D \cong \left[\frac{(10K_A + 8\,K_m)}{(K_A + K_m)}\right] \cdot \frac{N\log_2 N}{NL} \approx 10 \cdot \frac{N\log_2 N}{NL}$$

surface parameters of interest. The primary advantage of the quadrature moiré method compared with the other techniques is that modulo-pi transitions are generally widely spaced so that the measurements can be several fringe periods apart with no difficulty encountered in later correctly removing the transitions. Convolving the fringe pattern with quadrature sinusoidal windows or a complex exponential window requires that the measurement spacing be less than or equal to half a fringe period if phase transitions are to be correctly removed. The latter two methods are superior to QMM for the following reasons:

(1) Sum and reference spectral components due to the product $I(x,y) \cdot R(x,y)$ are not generated.

(2) Since the reference is built into the window, the number of multiplications that must be performed in evaluating the direct convolution is cut in half.

CHAPTER 4

# SUMMARY AND RECOMMENDATIONS

## An Overview

Data sets for the traditional and synchronous convolution methods are given by

$$D(x,y) = W(x,y) \cdot S(x,y) \qquad \text{Traditional} \qquad (4.1)$$

$$D(x,y) = [A + B \cdot \cos 2\pi W(x,y)] \cdot S(x,y) \qquad \text{Synchronous Convolution} \qquad (4.2)$$

In the traditional method the wavefront is sampled directly by locating fringe centers and assigning order numbers. A replica of $\overline{W}(F_x,F_y)$ aliased by sampling sidelobes occurs in the zero order peak of the data spectrum. A global least squares fit or an interpolation are applied to recover $W(x,y)$. For synchronous convolution the data set is a uniformly sampled version of the fringe pattern itself and not the wavefront. The desired phase information is contained in the first order sidelobes of a spectrum which is repeated at an interval in the frequency domain equal to the reciprocal of the sample spacing. $W(x,y)$ is recovered by application of specially-designed transfer functions to the data spectrum.

The relationship between the data spectrum and three traditional methods for recovering the wavefront from a biased fringe pattern is illustrated in Figure 34. From consideration of Parseval's theorem a

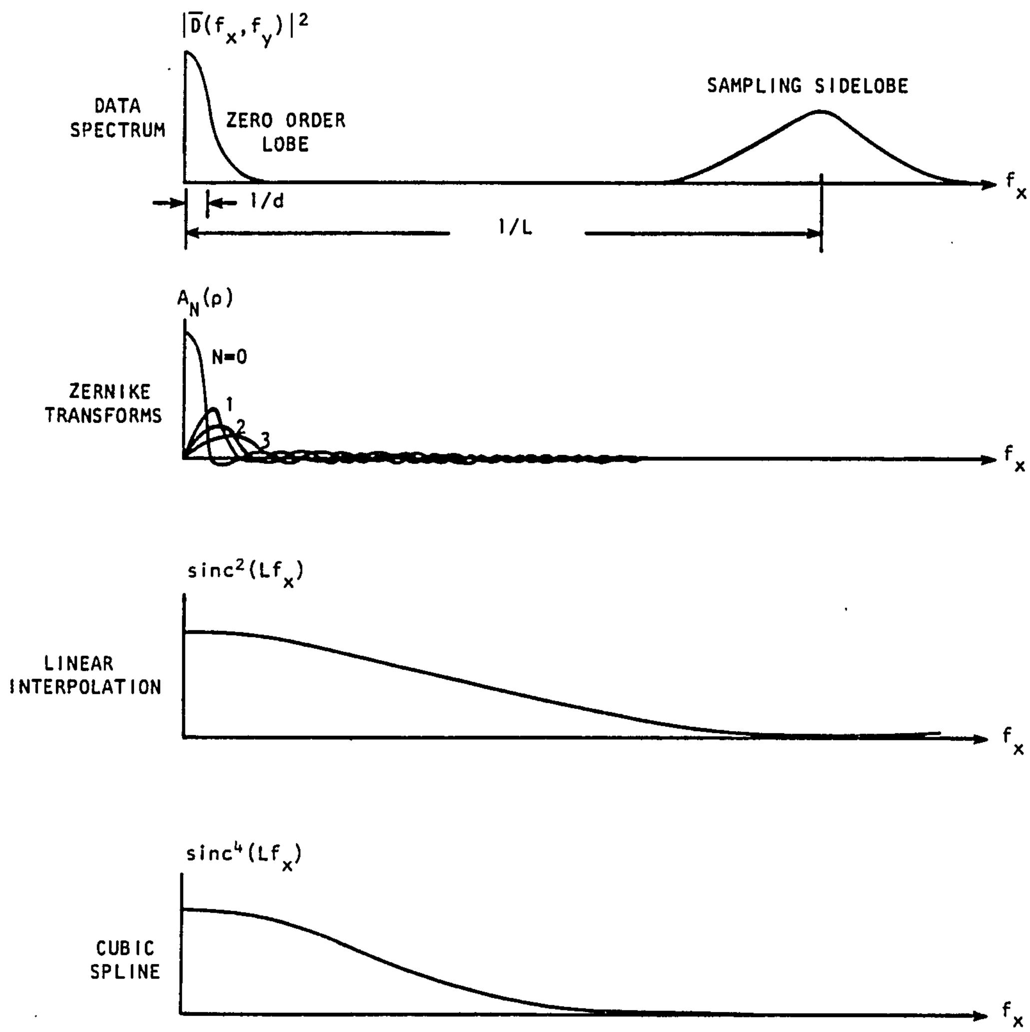


Figure 34. Data spectrum and transfer functions associated with three traditional approaches.

L = Sample Spacing
d = Pupil Diameter

global least squares fit of Zernike polynomials corresponds to building up an approximation to the zero order peak from a linear combination of Zernike transforms. The data spectrum is filtered by each Zernike transform in evaluating the integrals of the normal equations. Since these integrals extend over the entire frequency plane and since the Zernike transforms decay at a relatively slow rate with increasing distance from the origin, an alias error is contributed to each integral due to all the sampling sidelobes. For dense sampling the spectral sidelobes are widely spaced and the integrals give essentially the same result as would be obtained from evaluating the continuous integrals in the spatial domain. For comparison, linear interpolation and cubic spline interpolation to a raster-scanned data set are associated with transfer functions $\mathrm{sinc}^2(Lf_x)$ and $\mathrm{sinc}^4(Lf_x)$, respectively, where L is the nominal sample spacing. These have their first zeroes at the location of the first order sidelobes of the data spectrum. The half-power width of the transfer function for a cubic spline fit occurs at approximately 0.3/L where L is the fringe spacing of the biased fringe pattern. Thus features whose widths are three fringe spacings or wider are recovered in the fit. For a Zernike fit a large number of terms are required to recover a high spatial frequency feature of the wavefront and, in addition, there is the problem that alias error is greater for higher order terms than for lower ones.

A family of three synchronous convolution techniques for recovering the wavefront from the first order sidelobes of the fringe pattern were described in Chapter 3. Figure 35 summarizes their

| | $F(x,y) = G(x,y) * h'(x,y)$ | | |
|---|---|---|---|
| | Double Sideband | | Single Sideband |
| | Low-Pass | High-Pass | High-Pass |
| G(x,y) | $[A + B\cos 2\pi W(x,y)] \cdot \begin{matrix}\cos 2\pi f_R x \\ \sin 2\pi f_R x\end{matrix}$ | $A + B\cos 2\pi W(x,y)$ | $A + B\cos 2\pi W(x,y)$ |
| WINDOW FUNCTION | $h(x,y)$ 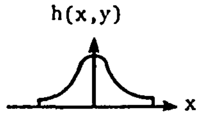 | $h'(x,y) = \begin{matrix}\cos 2\pi f_R x \cdot h(x,y) \\ \sin 2\pi f_R x \cdot h(x,y)\end{matrix}$ 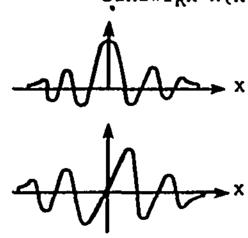 | $h'(x,y) = e^{i2\pi f_R x} \cdot h(x,y)$ 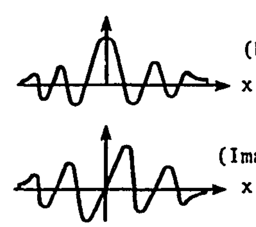 (Real) (Imaginary) |
| TRANSFER FUNCTION | 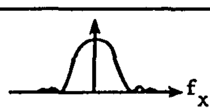 | 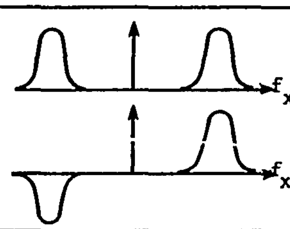 | 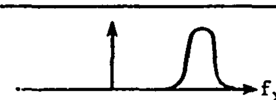 |
| PHASE | $f_R x + \frac{1}{2\pi}\tan^{-1}\left[\frac{F_1(x,y)}{F_2(x,y)}\right]$ | $\frac{1}{2\pi}\tan^{-1}\left[\frac{F_1(x,y)}{F_2(x,y)}\right]$ | $\frac{1}{2\pi}\tan^{-1}\left[\frac{\text{Imaginary Part}}{\text{Real Part}}\right]$ |
| TYPE | Quadrature moiré | Sinusoidal window | Complex exponential window |

Figure 35. Synchronous convolution methods.

characteristics and inter-relationships. The logical connections are particularly clear for the case of a biased fringe pattern.

(1) QMM involves multiplying the fringe pattern by a sinusoidal reference thereby shifting the spectral sidelobes to near-dc. A low-pass filter isolates them and attenuates high spatial frequency terms associated with the product of reference and unknown fringe patterns. Phase is computed from the filter outputs for quadrature references.

(2) The sinusoidal window technique eliminates the direct product with a reference pattern and instead the reference is made a part of the window envelope. The resulting quadrature high-pass filters pass the sidelobes and phase is computed directly from the two filter outputs.

(3) The two first order sidelobes are conjugates of one another and so either contains all the desired phase information. The complex exponential window technique filters out only a single sidelobe. The filter output is complex and phase is computed as the arctangent of the ratio of real and imaginary parts of the filter output.

The three synchronous convolution methods can be classified according to their transfer functions as double sideband low-pass, double sideband high-pass, and single sideband high-pass, respectively.

Phase measurement for all three methods involves summing over products of the form

(Fringe Pattern) x (Reference Term) x (Filter Envelope)

with the major difference occurring in the argument of the reference term. The effect of Gaussian noise upon phase error for each method is the same as for temporal synchronous detection (Bruning et al., 1974; Bruning, 1978) with the qualification that since the complex exponential window technique passes only a single sidelobe, the contribution of Gaussian noise is reduced for that case by a factor of two.

Advantages of the synchronous convolution methods over the traditional methods include the following:

(1) Measurements are obtained over a uniform grid with no need to locate fringe extrema.

(2) Accuracy in direct phase measurement is associated with signal-to-noise rather than the number of resolution elements from one extrema to the next.

(3) Little or no operator interaction is required.

These must be weighed against the following disadvantages:

(1) Phase information is lost near the edges of a fringe pattern due to the convolution.

(2) A high fringe density is required in order that local phase measurements are obtained in summing over a window width of several fringe periods.

## Recommendations

### Traditional Approach

A computer experiment can be performed to estimate what sample density is needed to achieve a desired accuracy in Zernike coefficients. In software data sets can be created corresponding to the expected amount of aberration plus varying amounts of tilt. It is expected that as the sample spacing decreases the Zernike coefficients obtained from least squares fits will converge to their ideal values.

If high accuracy is needed for Zernike coefficients, consider using spline interpolation followed by a Zernike fit to a dense uniform grid of interpolated values. The sidelobe attenuation associated with a cubic spline fit is much better than that of Zernike transforms. Also since error due to sampling sidelobes tends to occur in higher order Zernike coefficients and since error is coupled into the lower order coefficients due to the cross-correlation integrals of the normal equations, it is recommended that Zernike fits be truncated to as few terms as are actually needed. It is not a good idea to perform a 36-term fit when your primary objective is to obtain coefficients for subtracting tilt and defocus from the direct order assignment. General recommendations are to avoid random sampling, avoid closed fringe patterns, use a high resolution scanner, and sample densely.

Graphics tablet data entry is attractive due to its low cost and ease of implementation. The chief disadvantages are the dependence upon operator judgment and the time required to take data. At a speed of 1 point every two seconds over 30 minutes is required to reach 1000 points.

The random aspect of sampling with a graphics tablet can be easily improved upon by using a ruled transparent mylar sheet to guide the operator in choosing points. A video system for locating fringe centers and assigning order numbers is potentially faster than a tablet. This advantage is only true when interferograms are of sufficiently high quality that little or no video editing is needed to clean up errors. In the limit in which video data entry is totally manual using a cursor superimposed upon the fringe pattern image, the video and tablet approaches become nearly equal in speed and convenience provided the video cursor is under fast and accurate control of a joystick or trackball. Manual video data entry via the keyboard is slow and less convenient. The disadvantages of a video system relative to a tablet-based system are high cost and, if the video system is custom-designed, the complexity of hardware and software needed to handle a wide variety of fringe pattern conditions. In terms of resolution the graphics tablet has an advantage provided the interferogram covers a region greater than 2 to 3 inches across on the tablet surface. Tablets usually have resolutions of 200 points per inch or better. However, if the human link in the system is considered, the effective resolution of a tablet may be significantly less. Inexpensive CCTV cameras typically provide 50% MTF at 125 fringes across a horizontal line.

In conclusion, it is recommended that if a low volume of interferogram analyses are to be processed, a graphics tablet system may be the best choice. The potential automatic operation of a video system becomes attractive as the volume to be analyzed increases.

Synchronous Convolution Approach

Some firms have microdensitometers which are not routinely applied to traditional analyses due to the need for interactive software --the same problem encountered in developing an automated video system. Microdensitometers are, however, well-suited for phase measurement by the convolution methods and provide for those who have the facilities a simple way to process fringe pattern photographs. A low-cost microdensitometer can be constructed using a graphics tablet by modifying the cursor pen to include an optical sensor. A transparent plastic overlay with rows of slits can be positioned over a fringe pattern photograph to guide the pen through a raster scan. In this way a tablet can be adapted to the convolution as well as the traditional approach. Other attractive scanners include a CCD video camera with a commerical frame grabber or a long linear CCD array with a mechanical scan perpendicular to the array.

For high speed operation FFT's can be performed using an S2814 FFT processor (American Microsystems, Inc., 1981), which is designed as a peripheral for 8 bit microprocessors. With the single chip S2814, phase can be computed at a rate of ten 512 point lines per second if DMA is used for data transfers.

The synchronous convolution techniques can be regarded as image processing equivalents of temporal heterodyne interferometry and are recommended as attractive alternatives to the traditional approach for processing fringe pattern images.

## REFERENCES


Aime, C. and F. Martin, "Use of Diffraction Patterns as a Regular Diagnostic for Jittered Arrays of Periodic Structures," Proc. SPIE, 240 (1980).

American Microsystems, Inc., "S2814A Fast Fourier Transformer," Advanced Product Description, Santa Clara, California (1981).

Arcelli, C., L. P. Cordella, and S. Levialdi, "More About a Thinning Algorithm," Elec. Lett. 16 (1979).

Augustyn, W. H., A. H. Rosenfeld, and C. A. Zanoni, "An Automatic Interference Pattern Processor with Interactive Capability," Proc. SPIE, 153 (1978).

Balasubramanian, N. and G. W. DeBell, "A New Approach to High Precision Phase Measurement Interferometry," Proc. SPIE, 230 (1980).

Bernal, E. and J. Loomis, "Interactive Video Image Digitizer--Application to Interferogram Analysis," Proc. SPIE, 126 (1977).

Bezdidko, S. N., "The Use of Zernike Polynomials in Optics," Soviet J. of Optical Technology, 41 (1974).

Braile, L. W., "Comparison of Four Random to Grid Methods," Computers and Geosciences, 5 (1978).

Bruning, J. H., "Fringe-Scanning Interferometers," in Optical Shop Testing, John Wiley & Sons, New York (1978).

Bruning, J. H., D. R. Herriott, J. E. Gallagher, D. P. Rosenfeld, A. D. White, and D. J. Brangaccio, "Digital Wavefront Measuring Interferometer for Testing Optical Surfaces and Lenses," Appl. Opt., 13 (1974).

Cardwell, S. M., "Capacitive Stylus Design," Hewlett-Packard Journal, 32 (1981).

Castleman, K. R., Digital Image Processing, Prentice-Hall, Englewood Cliffs, N.J. (1979).

Crain, I. K. and B. K. Bhattacharyya, "Treatment of Non-Equispaced Two-Dimensional Data with a Digital Computer," Geoexploration, 5 (1967).

Dandliker, R., "Heterodyne Holographic Interferometry: A Review," Proc. SPIE, 136 (1977).

Eikonix Corporation, "7800 Series Universal Image Digitizers," Product Description, Bedford, Massachusetts (1981).

Fairchild, Inc., "CCD Imaging and Signal Processing," Product Catalog, Santa Clara, California (1981).

Freniere, E. R. and O. E. Toler, "Interferogram Evaluation Program," Opt. Eng., 20 (1981).

Funnell, W. R. J., "Image Processing Applied to the Interactive Analysis of Interferometric Fringes," Appl. Opt., 20 (1981).

Gaskill, J. D., Linear Systems, Fourier Transforms, and Optics, Wiley & Sons, New York (1978).

Glassman, A. T. and C. E. Orr, "Automated Interferogram Reduction," Proc. SPIE, 181 (1979).

Gordon, W. J. and B. K. Bhattacharyya, "B-Spline Curves and Surfaces," in Computer-Aided Geometric Design, Academic Press, New York (1974).

Hayslett, C. R. and W. H. Swantner, "Mathematical Methods for Deriving Wavefronts from Interferograms," American Society for Testing and Materials, Philadelphia, Pennsylvania, 666 (1978).

Hecht, E. and A. Zajac, Optics, Addison-Wesley, Reading, MA (1974).

Hildebrand, F. B., Advanced Calculus for Applications, Prentice-Hall, Englewood Cliffs, N.J. (1962).

Huang, T. S., "Two Dimensional Fourier Transform," in Digital Image Processing and Analysis, Noordhoff, Leyden (1977).

Huck, F. O., N. Halyo, and S. K. Park, "Aliasing and Blurring in 2-D Sampled Imagery," Appl. Opt., 19 (1980).

Ichioka, Y. and M. Inuiya, "Direct Phase Detecting System," Appl. Opt., 11 (1972).

Jain, V. K., "FFT Based Algorithms for High Accuracy Analog Measurements," Computer and Elec. Eng., 5 (1978).

Jones, H. D., "Computer Reduction of Holographic Interferograms," Sandia Laboratories, SAND77-8236 (1977).

Kintner, E. C. and R. M. Sillitto, "A New Analytic Method for Computing the Optical Transfer Function," Optica Acta, 23 (1976).

Koliopoulos, C., "Interferometric Phase Measurement," Ph.D. Dissertation, Optical Sciences Center, University of Arizona, Tucson (1981).

Lawson, J. L. and G. E. Uhlenbeck, Threshold Signals, McGraw-Hill, New York (1950).

Leith, E. N. and J. Upatnieks, "Reconstructed Wavefronts and Communication Theory," JOSA 52 (1962).

Loomis, J. S., FRINGE User's Manual, Version 2, Optical Sciences Center, University of Arizona, Tucson (1976).

Loomis, J. S., "Applications of Computer-Generated Holograms in Optical Testing," Ph.D. Dissertation, Optical Sciences Center, University of Arizona, Tucson (1980).

Massie, N. A., R. D. Nelson, and S. Holly, "High Performance Real-Time Heterodyne Interferometry," Appl. Opt., 18 (1979).

Monro, D. M., "Interpolation Methods in Surface Mapping," Computer Programs in Biomedicine, 11 (1980).

Nuttall, A. H., "Some Windows with Very Good Sidelobe Behavior," IEEE Trans. on Acoustics, Speech, and Signal Processing, 29 (1981).

Papoulis, A., The Fourier Integral and Its Applications, McGraw-Hill, New York (1962).

Perrin, J. C. and A. Thomas, "Electronic Processing of Moiré Fringes. Application to Moiré Topography and Elements of Comparison with Photogrammetry," Proc. SPIE, 136 (1977).

Pirodda, L., "Dimensional Metrology of Large Objects by Projection Moiré Techniques," Proc. SPIE, 136 (1977).

Pole, R. V., A. J. Spiekerman, and T. W. Hansch, "Interferometric Wavelength Measurements Through Post-Detection Signal Processing," IBM Journal of Research and Development, 24 (1980).

Race, R., "Orthogonal Polynomial Fitting of Interferograms," Bachelor's Thesis, MIT, Cambridge (1981).

Renes, J. and D. Beintema, "The Use of B-Spline Approximation and an Array Processor in the IRAS Ground Operations and Preliminary Analysis Facility," J. of the British Interplanetary Society, 34 (1981).

Reticon Corporation, "Linear Diode Arrays," Product Description, Sunnyvale, California (1981).

Rimmer, M. P., "Polynomial Fitting of Interferograms," Itek Technical Report, Lexington, Massachusetts (1972).

Shagam, R. N., "Heterodyne Interferometric and Moiré Test Methods for Surface Measurements," Ph.D. Dissertation, Optical Sciences Center, University of Arizona, Tucson (1980).

Slomba, A. F. and J. W. Figoski, "A Coaxial Interferometer with Low Mapping Distortion," Proc. SPIE, 153 (1978).

Snyder, J. J., "Algorithm for Fast Digital Analysis of Interference Fringes," Appl. Opt., 19 (1980).

Stanley, W. D., Digital Signal Processing, Reston Publishing Co., Reston, VA (1975).

Stavely, D. J., "A High Quality, Low-Cost Graphics Tablet," Hewlett-Packard Journal, 32 (1981).

Stefanelli, R. and A. Rosenfeld, "Some Parallel Thinning Algorithms for Digital Pictures, " J. of the Association for Computing Machinery, 18 (1971).

Stockham, T. G., "High Speed Convolution and Correlation," Proc. of the Spring Joint Computer Conference (1966).

Talmi, Y., "TV-Type Multichannel Detectors," Analytical Chemistry, 47 (1975).

Walkup, J. F. and J. W. Goodman, "Limitations of Fringe-Parameter Estimation at Low Light Levels," JOSA 63 (1973).

Wang, J. Y. and D. E. Silva, "Wavefront Interpretation with Zernike Polynomials," Appl. Opt., 19 (1980).

Whetstone, A. L., "A New Data Tablet/Digitizer Using Magnetostriction," Summagraphics Corporation, Fairfield, Connecticut (1980).

Womack, K. H., Video Interferogram Analysis System Manual, Optical Sciences Center, University of Arizona, Tucson (1980).

Womack, K. H., J. A. Jonas, C. Koliopoulos, K. L. Underwood, J. C. Wyant, J. S. Loomis, and C. R. Hayslett, "A Microprocessor-Based Instrument for Analyzing Video Interferograms," Proc. SPIE, 192 (1979).

Womack, K. H., K. L. Underwood, and D. Forbes, "Microprocessor-Based Video Interferogram Analysis System," Proc. SPIE, 230 (1980).

Yokozeki, S., Y. Kusaka, and K. Patorski, "Geometric Parameters of Moiré Fringes," Appl. Opt., 15 (1976).

Zanoni, C. A., "Method and Apparatus for Interference Fringe Center Sensing," Zygo Corporation, U.S. Patent No. 4,169,980 (1979).